

Spring 2011

An integrated circuit/microsystem/nano-enhanced four species radiation sensor for inexpensive fissionable material detection

Randy Paul Waguespack

Follow this and additional works at: <https://digitalcommons.latech.edu/dissertations>

 Part of the [Electrical and Computer Engineering Commons](#), and the [Nuclear Engineering Commons](#)

**AN INTEGRATED CIRCUIT/MICROSYSTEM/NANO-ENHANCED
FOUR SPECIES RADIATION SENSOR FOR INEXPENSIVE
FISSIONABLE MATERIAL DETECTION**

by

Randy Paul Waguespack, B.S., M.S.

A Dissertation Presented in Partial Fulfillment
of the Requirements for the Degree
Doctor of Philosophy

COLLEGE OF ENGINEERING AND SCIENCE
LOUISIANA TECH UNIVERSITY

May 2011

UMI Number: 3459546

All rights reserved

INFORMATION TO ALL USERS

The quality of this reproduction is dependent upon the quality of the copy submitted.

In the unlikely event that the author did not send a complete manuscript and there are missing pages, these will be noted. Also, if material had to be removed, a note will indicate the deletion.



UMI 3459546

Copyright 2011 by ProQuest LLC.

All rights reserved. This edition of the work is protected against unauthorized copying under Title 17, United States Code.



ProQuest LLC
789 East Eisenhower Parkway
P.O. Box 1346
Ann Arbor, MI 48106-1346

LOUISIANA TECH UNIVERSITY

THE GRADUATE SCHOOL

March 16th, 2011

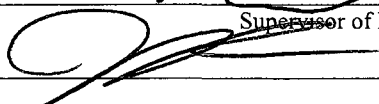
Date

We hereby recommend that the dissertation prepared under our supervision
by Randy Paul Waguespack

entitled AN INTEGRATED CIRCUIT/MICROSYSTEM/NANO-ENHANCED FOUR
SPECIES RADIATION SENSOR FOR INEXPENSIVE FISSIONABLE
MATERIAL DETECTION

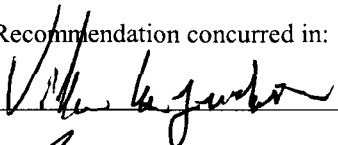
be accepted in partial fulfillment of the requirements for the Degree of
Doctor of Philosophy in Engineering

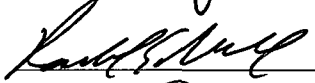


Supervisor of Dissertation Research


Head of Department
College of Engineering and Science

Department

Recommendation concurred in:








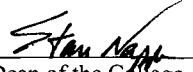
Advisory Committee

Approved:


Director of Graduate Studies

Approved:


Dean of the Graduate School



Dean of the College

ABSTRACT

Small scale radiation detectors sensitive to alpha, beta, electromagnetic, neutron radiation are needed to combat the threat of nuclear terrorism and maintain national security. There are many types of radiation detectors on the market, and the type of detector chosen is usually determined by the type of particle to be detected. In the case of fissionable material, an ideal detector needs to detect all four types of radiation, which is not the focus of many detectors. For fissionable materials, the two main types of radiation that must be detected are gamma rays and neutrons. Our detector uses a glass or quartz scintillator doped with ^{10}B nanoparticles to detect all four types of radiation particles. Boron-10 has a thermal neutron cross section of 3,840 barns. The interaction between the neutron and boron results in a secondary charge particle in the form of an alpha particle to be emitted, which is detectable by the scintillator.

Radiation impinging on the scintillator matrix produces varying optical pulses dependent on the energy of the particles. The optical pulses are then detected by a photomultiplier (PM) tube, creating a current proportional to the energy of the particle. Current pulses from the PM tube are differentiated by on-chip pulse height spectroscopy, allowing for source discrimination. The pulse height circuitry has been fabricated with discrete circuits and designed into an integrated circuit package. The ability to replace traditional PM tubes with a smaller, less expensive photomultiplier will further reduce the size of the device and enhance the cost effectiveness and portability of the detector.

APPROVAL FOR SCHOLARLY DISSEMINATION

The author grants to the Prescott Memorial Library of Louisiana Tech University the right to reproduce, by appropriate methods, upon request, any or all portions of this Dissertation. It is understood that "proper request" consists of the agreement, on the part of the requesting party, that said reproduction is for his personal use and that subsequent reproduction will not occur without written approval of the author of this Dissertation. Further, any portions of the Dissertation used in books, papers, and other works must be appropriately referenced to this Dissertation.

Finally, the author of this Dissertation reserves the right to publish freely, in the literature, at any time, any or all portions of this Dissertation.

Author Randy Waguerpuk
Date 4/27/2011

TABLE OF CONTENTS

ABSTRACT.....	iii
LIST OF TABLES	ix
LIST OF FIGURES	x
ACKNOWLEDGEMENTS	xv
CHAPTER ONE: INTRODUCTION.....	1
1.1 Types of Radiation Detectors.....	3
1.1.1 Gas Based Detectors	3
1.1.2 Semiconductor Detectors	4
1.1.3 Scintillator Detectors	5
1.2 Dissertation Objectives	6
1.3 Literature Review.....	7
CHAPTER TWO: RADIATION PRINCIPLES	23
2.1 Radiation Sources	23
2.1.1 Alpha Particle Sources	25
2.1.2 Beta Particle Sources	26
2.1.3 Electromagnetic Radiation Sources	28
2.1.4 Neutron Sources.....	32
2.2 Radiation Interactions with Matter	34
2.2.1 Alpha Particle Interactions.....	35

2.2.2 Beta Particle Interactions	36
2.2.3 Electromagnetic Interactions	38
2.2.4 Neutron Particle Interactions	41
CHAPTER THREE: RADIATION DETECTORS	43
3.1 Gas Based Radiation Detectors.....	43
3.1.1 Ionization Chamber.....	45
3.1.2 Proportional Counter.....	45
3.1.3 Geiger-Müller Counter.....	47
3.2 Solid State Detectors.....	48
3.3 Scintillator Detectors	51
3.3.1 Organic Scintillators	52
3.3.2 Inorganic Scintillators.....	54
CHAPTER FOUR: BORON LOADED SCINTILLATORS FOR DETECTION OF ALL FOUR TYPES OF RADIATION SPECIES	55
4.1 Device Design.....	57
4.2 Fabrication	58
4.2.1 Device	58
4.2.2 Scintillators	60
4.3 Testing.....	61
4.3.1 Testing Setup	63
4.4 Results and Discussion	65
4.4.1 Beta Particles	65
4.4.2 Gamma Rays.....	68
4.4.3 Alpha Particles and Neutrons.....	71

4.4.4 More Quartz Testing	74
4.4.5 Radiation Source Differentiation	75
CHAPTER FIVE: CREATING A DETECTING PACKAGE: ADDING CIRCUITRY	78
5.1 Circuit Design	79
5.1.1 Charge Sensitive Preamplifier	80
5.1.2 Filtering and Shaping.....	84
5.1.3 Peak Detection and Comparator Trigger	90
5.1.4 Complete Radiation Spectroscopy Circuit.....	92
5.2 Integrated Circuit Design.....	95
5.2.1 Amplifier Design	96
5.2.2 Operational Amplifier Design.....	103
5.2.3 Biasing Circuit Design.....	106
5.2.4 Comparator Circuit Design	111
5.2.5 Operational Amplifier Simulation Results.....	115
5.2.6 Comparator Simulation Results	120
5.3 Integrated Circuit Layout Design.....	121
5.3.1 Operational Amplifier Layout.....	122
5.3.2 Comparator Layout	123
5.3.3 Passive Component Layout.....	123
5.3.4 Pads and Pad Frame	125
5.3.5 Chip Core	126
5.4 Results and Improvements.....	127
5.4.1 Operational Amplifier Testing	128

5.4.2 Operational Amplifier Improvements.....	132
5.4.3 Comparator Testing and Improvements.....	136
5.4.4 New Test Layout.....	138
CHAPTER SIX: COMPLETING THE DETECTING PACKAGE: STACKED LAYER PHOTOMULTIPLIER TUBE.....	140
6.1 Photomultiplier Tube Components.....	142
6.1.1 Photocathode.....	143
6.1.2 Dynode Stages	145
6.2 Design	147
6.2.1 Dynodes and Anode.....	147
6.2.2 Voltage Divider.....	149
6.3 Fabrication	150
6.3.1 Dynode Layers	151
6.3.2 Voltage Divider.....	154
6.4 Testing.....	154
6.4.1 Testing Equipment.....	155
6.4.2 Testing Setup	155
6.5 Results and Discussion	156
REFERENCE.....	161

LIST OF TABLES

Table 5.1 Transistor sizes for the operational amplifier	106
Table 5.2 Transistor sizes for the current reference circuit	109
Table 5.3 Transistor sizes for the current mirror bias circuit.....	111
Table 5.4 Transistor sizes of the comparator	114
Table 5.5 New transistor sizes for the operational amplifier	134
Table 5.6 New transistor sizes for the comparator circuit	137

LIST OF FIGURES

Figure 2.1	^{36}Cl energy spectrum.....	28
Figure 2.2	Decay scheme of ^{60}Co	29
Figure 2.3	Possible electron orbital transitions	31
Figure 2.4	Range of alpha particles.....	36
Figure 2.5	Range of beta particles.....	38
Figure 2.6	Compton scattering	40
Figure 3.1	The different operating regions of gas-filled detectors.....	44
Figure 3.2	Configuration of organic scintillator electronic energy levels.....	53
Figure 4.1	Glass and quartz substrates doped with boron nanoparticles converts radiation particles into optical pulses with varying heights which exit the scintillator (a). Optical pulses exiting the scintillator are directed away from the scintillating window by gold coated waveguides (b). The micro-device is patterned on-chip for a complete integrated radiation detection package (c)	58
Figure 4.2	2-D process flow	59
Figure 4.3	Photo of scintillating micro device with patterned scintillating quartz material inside of the etched cavity and gold coated waveguides (Cap not shown).....	59
Figure 4.4	Micro-device drawing	60
Figure 4.5	Beta counts verse distance for the glass scintillator.....	66
Figure 4.6	Quartz scintillator compared to the glass scintillator for beta detection...	67
Figure 4.7	Glass and quartz absorption of beta particles as substrate thickness is increased	68

Figure 4.8	Testing the scintillator detectors with a gamma ray source for a function of counts per minute over varying distances	69
Figure 4.9	Glass and quartz have similar energy spectra allowing for glass or quartz to be used as the detecting medium	70
Figure 4.10	Glass and quartz absorption of gamma rays as substrate thickness is increased	71
Figure 4.11	Boron doped scintillator has the ability to detect all four radiation species. Scaling for the alpha, beta, and gamma pulse are 50 mV y-axis divisions and scaling for the neutron pulse is 25 mV y-axis divisions	73
Figure 4.12	Quartz scintillator was doped with various doping percentage based on weight.....	74
Figure 4.13	Energy spectrum of the quartz scintillator doped with 2%, 5% and 10% boron by weight	75
Figure 4.14	Decay scheme for cesium-137 and cobalt-60 radiation sources	76
Figure 4.15	Source differentiation between ^{137}Cs and ^{60}Co	76
Figure 5.1	Block diagram of circuit components	80
Figure 5.2	Schematic diagram of the simulated charge-sensitive preamplifier	81
Figure 5.3	Varied input test currents with uniform pulse width	82
Figure 5.4	Uniform input test current with varied pulse width	82
Figure 5.5	Peak output voltage with feedback capacitor of 5pF	83
Figure 5.6	Peak output voltage with varying pulse widths	83
Figure 5.7	Preamplifier output with 5pF capacitor and 100k resistor.....	84
Figure 5.8	Preamplifier output with varying feedback capacitors and 100k resistor	84
Figure 5.9	Preamplifier input and desired filter output	86
Figure 5.10	Canonical representation of the transfer function $H(s)$	86
Figure 5.11	Schematic of a Sallen-Key low pass filter	87

Figure 5.12	Schematic of 5 th order filter	89
Figure 5.13	LT Spice simulation versus the desired output $y(t)$	89
Figure 5.14	Schematic of a peak detector with op-amp buffers.....	90
Figure 5.15	Peak detector output waveform	91
Figure 5.16	Comparator circuit used to trigger a microcontroller	92
Figure 5.17	Discrete circuit charge sensitive pre-amplifier and Sallen-Key filters	93
Figure 5.18	Radiation spectroscopy circuit for the integrated circuit layout	94
Figure 5.19	Output waveform of the radiation spectroscopy circuit.....	95
Figure 5.20	Four common-source amplifier configurations	97
Figure 5.21	Common-source amplifier with a current source load.....	98
Figure 5.22	Cascode amplifier configuration.....	99
Figure 5.23	Folded cascode topology with diode connected pair	100
Figure 5.24	Push-pull output topology.....	101
Figure 5.25	NMOS source-coupled differential pair.....	102
Figure 5.26	Differential amplifier with a current mirror load.....	103
Figure 5.27	Two-stage operational amplifier block diagram	104
Figure 5.28	Two-stage operational amplifier design.....	105
Figure 5.29	Basic current mirror with resistor loads.....	107
Figure 5.30	Current reference circuit with start-up circuit.....	108
Figure 5.31	Current mirrors for bias voltages 2, 3, and 4	109
Figure 5.32	Current mirrors for bias voltages 1, N, and P	110
Figure 5.33	Block diagram of a comparator.....	111
Figure 5.34	Comparator pre-amplification stage	112

Figure 5.35	Comparator decision circuit.....	113
Figure 5.36	Comparator schematic	114
Figure 5.37	Open loop gain and phase response, 500 fF capacitor.....	116
Figure 5.38	Open loop gain and phase response, 250 fF capacitor.....	117
Figure 5.39	Step response, 500 fF capacitor	118
Figure 5.40	Step response, 250 fF capacitor	119
Figure 5.41	Comparator switching test at 200 mV	120
Figure 5.42	Transient response of the comparator	121
Figure 5.43	Operational amplifier layout.....	122
Figure 5.44	Comparator layout	123
Figure 5.45	Capacitor layout for 500 fF(a) and 250 fF(b) capacitors	124
Figure 5.46	50 kilo-ohm resistor layout.....	125
Figure 5.47	Layout of complete radiation detection circuitry.....	127
Figure 5.48	Inverted step response of one particular 250 fF amplifier	129
Figure 5.49	Non-inverted amplification of the 500 fF amplifier with a gain of two	130
Figure 5.50	Inverting amplification of the 500 fF amplifier	130
Figure 5.51	Step response of the 500 fF amplifier	131
Figure 5.52	Testing the output limitations of the amplifier	132
Figure 5.53	Common centroid layout of a transistor pair	133
Figure 5.54	New op-amp layout with better transistor matching.....	134
Figure 5.55	Under-sized power and ground traces become resistors in the circuit....	135
Figure 5.56	New comparator schematic.....	137
Figure 5.57	New comparator layout with transistor matching.....	138

Figure 5.58	Test layout for second MOSIS fabrication run	139
Figure 6.1	AutoCAD drawing of a stacked layer PM tube	142
Figure 6.2	Spectral response of common types of photocathode materials [68]	144
Figure 6.3	Dynode electron amplification.....	145
Figure 6.4	Photomultiplier tube dynode configurations [67].....	147
Figure 6.5	First stack layer design; layers are alternated as they are stacked	148
Figure 6.6	Second stack layer design; only a single layer is needed, requiring each layer to be rotated 180° as they are stacked.....	149
Figure 6.7	Schematic diagram of the voltage divider circuit	150
Figure 6.8	Master mold milled from Teflon stock	151
Figure 6.9	Reverse silicon mold of dynode master mold.....	152
Figure 6.10	Dynode layers from cast stainless steel powder mixture	153
Figure 6.11	Eight layer dynode stack for testing.....	153
Figure 6.12	Voltage divider circuit	154
Figure 6.13	Voltage change versus dynode voltage for each filament voltage of the eight layer dynode stack.....	157
Figure 6.14	Voltage change versus filament voltage of the eight and six layer dynode stacks	158
Figure 6.15	Voltage change versus filament voltage of the non-coated and Al-coated dynode stacks.....	159

ACKNOWLEDGEMENTS

I would like to express my sincere gratitude to my wife, Stacy; my parents, Effie and Jason; and my family for their love, support, and encouragement throughout the years, allowing me to accomplish my goals.

I would also like to express my gratitude to my advisor, Dr. Chester Wilson; “the group;” and my graduate committee – Dr. Ville Kaajakari, Dr. Rastko Selmic, Dr. Randy Null, and Dr. Long Que. Thank you for the support, guidance, ideas, and conversations over the years at Louisiana Tech.

CHAPTER ONE

INTRODUCTION

The ability to detect all forms of radiation species, alpha, beta, gamma/X-ray, and neutrons, is important in industries such as oil and coal exploration, biological imaging and treatment, nuclear reactor facilities, and it is also of importance to the Department of Homeland Security. Since the beginning of the nuclear age, the materials needed to construct a nuclear weapon have been gathered by many different nations around the world and some weapons that have been created may not be adequately secured from theft or sale in some parts of the world [1]. There are also many nuclear reactors that are spread around the world that are capable of producing the raw material that is needed to construct a nuclear device by using documents that have been published on building these devices. Because of this, The National Academy of Engineering listed the ability to detect nuclear materials, at a distance, as one of the five major challenges in preventing nuclear terror [1]. To accomplish this task, there is a need to create detectors that are small and concealable, as well as reliable enough to discriminate between various types of radiological sources. These detectors would be implemented into portable devices and sensor networks that can be deployed in areas vulnerable to weapon smuggling across borders, as well as areas of interest where weapons grade fissionable material can potentially be produced.

One of the major challenges to radiation detectors is the size of the device. Current field detectors are bulky and not easily concealed if necessary. Geiger counters are one of the more popular types of detectors used in the field. Traditional Geiger counters are the size of a small shoe box, which limits the types of applications for which it can be used. Another concern with current detectors is the cost of the detector. If an array of detectors is needed for an application, the cost per detector becomes a major factor in the number of devices that can be purchased and deployed. Reducing the size of the detector not only increases the applications for which it can be used, but also reduces the price of the detector depending on the types of technologies that can be utilized in its construction.

One major area that needs a deployment of a large number of detectors is cargo ports. Currently in the United States, only a small number of shipping containers are checked for fissionable material. There is no system in place that could check all containers entering the ports for a nuclear weapon. There is no such system because it is not feasible to implement traditional detectors because of both the size of the devices and the cost of a mass deployment. There is a need to create a device that is small, relatively cheap, and has the ability to be mass produced, to create the type of large scale detector network needed to adequately address the problem.

Creating detectors that are easy to deploy in the field and that can be controlled off-site give the ability to easily cover and monitor large areas for radiation. These types of networks can be covertly deployed in and around nuclear reactor sites and other areas in foreign countries that are suspected of producing weapons grade material to be used in

the construction of a nuclear weapon. These types of capabilities become possible once the size and cost of radiation detectors are reduced.

1.1 Types of Radiation Detectors

There are three main types of radiation detectors that are commonly used, each having its own method to detect the radiation particles. They are divided into gas based detectors, semiconductor detectors, and scintillator detectors. Gas based detectors use a gas that is electrically biased to collect ionized particles, which are a result of the interaction between the radiation particle and the fill gas. Semiconductor detectors rely on a reverse biased diode junction to create electron hole pairs when the depletion region is excited by incoming radiation particles. Scintillator detectors interact with incoming radiation particles and, as a result, release light photons that are then detected using an optical transducer.

1.1.1 Gas Based Detectors

Gas based detectors are classified by the amount of applied voltage and the region in which the chamber is operated. They are divided into ion chambers, proportional counters, and Geiger counters. They each have their own design and method of operation, but all rely on the creation of ion pairs within the fill gas of the device.

Gas based detectors can be operated in current mode or pulse mode. Ion chambers are typically operated in current mode, using an applied voltage between two electrodes to set up an electric field within the chamber. Incoming radiation particles create ion pairs within the fill gas. The created positive ions and electrons are swept to the opposite electrodes, creating a constant current that is proportional to the intensity of the incoming radiation flux.

Proportional counters are used when higher sensitivities are needed for radiation detection. Proportional counters typically operate in pulse mode and on the principle of gas multiplication. Gas multiplication occurs when the initial ion pairs have enough energy to create secondary ion pairs. When operating in pulse mode, each radiation interaction results in a single pulse inside of the chamber. This pulse is typically proportional to the energy of the incoming radiation particle.

The third type of gas based detector used is the Geiger counter. The Geiger counter also relies on gas multiplication but is operated at higher energy potentials than proportional counters, which results in a larger electric field within the detector. The use of higher electric fields does not result in the pulse being created from the incoming radiation to be proportional to the energy of the particle. Due to the Geiger counter's higher electric field, the kinetic energy of the created electrons is much higher. This increase in energy results in an increase in the number of secondary ion pairs produced in the gas. The creation of secondary pairs continues until a saturation point is reached, resulting in all detected particles to produce the same output pulse, making the output independent of the incoming radiation energy. This limits the application of the Geiger counter because it is only useful in detecting the presence of radiation, but it is still a very popular device due to its simple design and operation.

1.1.2 Semiconductor Detectors

Semiconductor detectors rely on the creation of electron hole pairs within the crystal structure of the semiconductor. Like the ion pairs created in the fill gas of the previous detectors, the interaction between the incoming radiation particle and the semiconductor crystal create electron hole pairs by exciting an electron from the valence

band into the conduction band of the crystal. Semiconductor detectors can have an energy resolution that is ten times greater than that of gas based detectors because of the lower energy required to create an electron hole pair. The average energy needed to create an ion pair within the fill gas of a gas detector is about 30 eV, while the energy needed to create an electron hole pair inside of a silicon semiconductor is about 3 eV [2]. This lower energy allows for more pairs to be created for the same radiation particle energy, giving more information about the incoming particle. The disadvantage of using semiconductors is the dependence on operating temperature, since the band gap of the crystal can be affected with a change in operating temperature, giving the device thermal background noise.

1.1.3 Scintillator Detectors

Scintillator detectors, unlike gas based and semiconductor detectors, do not rely on the production of ion or electron hole pairs; they instead rely on the process of fluorescence to detect the presence of incoming radiation particles. Scintillators are based off the production of photons when the radiation particles interact with the scintillating medium. The incoming radiation will interact with atoms inside of the scintillating medium, exciting electrons from their ground state into higher energy orbitals. When the electrons drop back down into the ground state, the extra energy is released as a light photon. If the scintillator material is transparent to the wavelength of the created photon, the photon will be able to exit the material and be detected by either a photomultiplier (PM) tube or a photodiode.

Scintillators can be divided into two types of material, inorganic and organic. Inorganic materials usually have a higher light output and linearity compared to organics,

but they tend to have a slower response time. Inorganic materials must also be configured into a crystal lattice like a semiconductor material. When electrons that are excited into the conduction band by radiation energy recombine back with the hole in the valence band, an optical pulse is released. This optical pulse is usually outside of the visible light range, so the crystal of the scintillator is doped with activator impurities that allow for additional energy levels within the band gap of the material. This allows for the electron to de-excite to a new energy level before recombining in the valence band and will result in an optical pulse in the visible range. Organic scintillators have a lower light output than inorganic scintillators, but they have better response times. The fluorescence process in organic scintillators occurs within one molecule of the material and is not dependent on the crystal structure of the scintillator. Because of this, organic scintillators can be found in pure organic crystals, liquid, plastic, or a gas state.

1.2 Dissertation Objectives

The objectives of this research are to design, construct and test small scale radiation detectors that have the ability to detect all four types of radiation species: alpha, beta, gamma/X-ray, and neutrons. The detection of all four types of radiation is important when trying to determine what type of radiological species is being detected. The ability to determine the exact species is important because nuclear weapons are not the only material that emits radiation. Medical isotopes also emit various types of radiation, but this type of radiation is different from bomb material in species and energies. A device that has the ability to differentiate between the types of radiation species would be helpful in determining the type of threat a source that is emitting radiation poses.

Another important factor in the device design is the overall cost of the complete detector. Current detectors are expensive, limiting the number of detectors that can be deployed on a large scale because it is not economical to create a network at such a high expense. The device in this research uses a single scintillator to detect all types of radiation species reducing the cost, since most types of detectors focus on detection of only one type of species, requiring multiple detectors for multi-species detection. This is one factor that helps to reduce the overall cost of the radiation detector.

The device developed as part of this research uses two types of substrates doped with boron nanoparticles used for charge conversion as a detecting medium for all types of radiation species. The nanoparticles convert the high energy incident radiation particles into lower energy electrons which then scintillate in the substrate, producing light particles that can then be detected. A photomultiplier (PM) tube is used to detect the optical pulses and circuitry was constructed to amplify, shape and record the pulse heights of the incoming radiation particles. Pulse height spectroscopy can then be used to determine the types of particles impinging on the scintillator, which can be used to determine the type of source being detected. To further reduce the overall size of the detector, research was conducted to replace the traditional PM tubes with smaller, less expensive photomultipliers. A photomultiplier design that is small and easy to fabricate will improve the cost effectiveness, as well as reduce the overall detector size, increasing portability.

1.3 Literature Review

As discussed previously, many nations around the world either currently have nuclear weapons, or are in the process of acquiring the materials and means necessary to

construct a nuclear weapon. The threat of nuclear weapons used in conventional warfare is small due to mutual deterrence. Deterrence is the stopping of an enemy from using weapons of mass destruction, such as nuclear warheads, by making them aware that the response to such an act would result in retaliation that is far worse than the initial attack. This method of defense is effective between large nations, but a new threat has arisen with the possibility of small rogue groups possessing and smuggling single nuclear devices into a country and detonating it. So the threat has moved from large nations using nuclear weapons in conventional warfare to small groups of terrorist having the capabilities to destroy a large population.

The United States does not currently have the infrastructure and technology to search every cargo container that enters U.S. ports. Because of this, less than ten percent of all the containers that enter the ports are searched [3]. Because of the number of containers in a port at one time, one solution to this is to create a large network of wireless sensors that can be implemented into the containers. The sensors can use mesh networking algorithms that can automatically reconfigure the wireless network connections as the containers are moved around the port [4]. This would allow continuous real-time monitoring of the port with the constant movement of containers being uninterrupted, by the scanning of each container for fissionable materials. For a network of sensors to be feasible the detector, such as the one covered in this work, needs to be small, relatively cheap and easy to produce on a large scale.

Another area that these sensors are of interest to is nuclear power plants. Entergy Nuclear has addressed the problem that they lack real-time field monitors that are low cost. One goal of the facility is to have real-time monitors for each person working on

site and for specific locations within the plant. All of the monitors would be networked together, so the person wearing the sensor is aware of what it is detecting, and this information could be relayed back to a central location where a few individuals could monitor everyone on site.

We are not the only group conducting research in the area of small portable radiation detectors to meet the needs of the world. One group has been working on a hand-held neutron detector using boron-carbide diodes. K. Osberg, et al. has produced a system that uses the boron-carbide diode to detect incoming neutrons and circuitry along with a microcontroller to process the charge outputted from the diode. They have been successful at detecting and classifying the energy of the neutrons from their plutonium-beryllium neutron source [5]. The system has been able to detect neutrons, but the noise in the system limits the detection of lower energy neutrons and is limited to detecting only neutrons.

Another group has been experimenting with making a boron-loaded plastic scintillator that is lower cost than off the shelf scintillators that can be purchased from Bicron. S. Normand, et al. has created a scintillator that uses a distilled styrene base along with p-terphenyl (PPP) and POPOP (1,4-bis(5-phenyloxazol-2-yl)benzene), with a boron content of 5% by weight. They have created a scintillator that is a factor of four lower in cost when compared to Bicron's BC454 5% boron loaded scintillator [6]. The scintillator shows similar detection efficiencies as the Bicron scintillator when exposed to an ^{241}Am alpha source and AmBe neutron source. This group has shown that there are lower cost scintillator materials, with similar detection efficiencies compared to commercial products that can be used for neutron and alpha detection, but the detection

efficiency does become reduced as the scintillator size is reduced. The application of this device was designed for nuclear waste management in areas of high neutron flux.

J.S. Neal, et al. has constructed a new type of single crystal scintillator made from $\text{CeCl}_3(\text{CH}_3\text{OH})_4$ for fast neutron detection. The $\text{CeCl}_3(\text{CH}_3\text{OH})_4$ scintillator is a rare-earth metal-organic scintillator that has the ability to detect fast neutrons, gamma-rays and x-rays [7]. The scintillator is successful in detecting fast neutrons because of the high hydrogen content of the material; fast neutrons can be moderated and then detected [7]. They have successfully been able to detect neutrons with an energy of 14.1 MeV. They state the benefits of this material compared to rare-earth halides scintillators that are currently used in labs is the fact this new scintillator can be grown at room temperature and is less prone to thermal cracking [7]. The drawback to this material is that it is sensitive to air, and while it can detect neutrons and gamma-rays in high flux environments, it cannot distinguish between the types of radiation being detected.

Another group has created special ceramic scintillators that can detect alpha, beta, and low energy x-rays. Y. T. Viday, et al. developed different types of ceramic scintillators such as BaF_2 , $\text{CaF}_2:\text{Eu}^{2+}$, ZnS , and ZnO and compared them to the CsI crystal scintillator. The ZnS and $\text{CaF}_2:\text{Eu}^{2+}$ scintillators showed a light output of 35% and 28%, respectively, when compared to the CsI crystal [8]. The ceramic scintillators are easier to produce and more robust than the inorganic scintillators, which make them good for mass production applications, but they lack the ability of neutron and gamma-ray detection.

M. E. Kellior and L. W. Burggraf have developed an interesting type of porous scintillator for alpha detection in aqueous solutions. The pair used two types of

scintillators, one gel-silica scintillator doped with polonium and another using mesh silica glass beads [9]. The group was able to achieve detection efficiencies of 99% with the gel-silica samples and 97% efficiency when testing the glass beads [9]. Although their scintillator is limited to alpha detection, further development into the detection of other radiation types would be beneficial to both the nuclear energy and waste industries.

One group has been investigating the use of ZnS scintillators doped with various impurities to adjust the detection efficiency, count rate, and the decay times of the scintillators. The two conversion mediums used were ^{10}B and ^6Li because of their good neutron cross-sections. The ZnS scintillator doped with ^6Li had a neutron detection efficiency of 40% [10]. These results were compared to ZnS doped with ^{10}B since the neutron cross sections of ^{10}B is four times higher than ^6Li , but the light yield from the boron interaction is about two times lower than the lithium [11]. It was found that both scintillators provided around the same detection efficiencies. The use of ZnS scintillators showed good detection efficiency and discrimination between gamma-rays and neutrons, but the decay times of the scintillators were relatively slow, limiting their count rate. The group has also investigated various types of glass scintillators. The glass scintillators have a combination of both lithium and boron doped into the same scintillator. While the scintillator did have good detection of both gammas and neutrons, they were not able to discriminate between the two sources [12].

L. Swiderski, et al. has been investigating the use of a commercial liquid scintillator, BC523A, doped with ^{10}B particles for neutron and gamma-ray detection. The group's scintillator has been used to detect neutrons with energies ranging from tens of MeV down to thermal neutron energies without the use of additional moderators [13].

The groups scintillator compared to a standard commercial liquid scintillator, BC501A, shows that the addition of the boron is what provides the ability to detect the thermal neutrons [13]. They have been successful with detecting and discriminating between fast and thermal neutron events but have trouble differentiating between low energy gamma-rays and neutron events.

E. Kamaya, et al. has experimented with loading organic scintillators with ^{10}B for neutron detection with short decay times. Glass scintillators that are sensitive to neutrons have a decay time of about 100 to 200 ns, while the organic scintillators have a decay time of about 3.7 ns for the organic polymer with boron and 7.4 ns for the organic polymer with boron blended with polymethylmethacrylate [14]. The author does say that the detection efficiencies of the scintillators are very low and need to be improved. One improvement for future testing is to use ^{10}B to replace naturally occurring boron, which was used in the first experiments [14]. The use of ^{10}B should increase the detection efficiency since the ^{10}B has a higher neutron cross section than naturally occurring boron.

Creating a detecting platform that is small and covert is important for applications where the area in question is not open to outsiders. R. Aryaeinejad, et al. has created a detector that is small and can detect neutrons in a high gamma flux environment. The overall size of the complete sensor is 3 x 4 x 6 inches. The detector uses a glass scintillator doped with ^6Li , using a thickness of only a few millimeters to achieve high detection efficiency. To detect the neutrons in a high gamma flux environment, the scintillator doped with ^6Li is paired with another scintillator that is doped with ^7Li . Using the ^6Li scintillator alone makes it difficult to distinguish between the neutron source and gamma field; subtracting the spectrum of the ^7Li scintillator from the ^6Li results in a pure

neutron spectrum [15]. The device is limited to the detection of only thermal neutrons and cannot perform energy spectroscopy on the gamma rays.

One of the limiting factors to the overall size of a scintillator detector is the PM tube and the circuitry needed to operate the PM tube at high voltages. The high voltage supply usually does not need to provide large currents but does need to supply multiple output voltages to supply the dynodes of the PM tube [16]. Another concern with creating a portable detector is the total power consumption of the device and battery lifetime. Typical portable power supplies for PM tubes utilize DC to DC converters to achieve high voltages and then use a voltage divider network to supply individual voltage levels to each dynode. Spencer, et al. explored the use of a Cockroft-Walton voltage multiplier to power their PM tubes. The benefit to using this type of circuit is that the dynodes can be supplied from the stages within the Cockroft-Walton circuit; this precludes the need for the voltage divider circuit and allows for a smaller footprint of high voltage circuitry [16].

Idaho National Engineering and Environmental Laboratory developed a detector with ^6Li and ^7Li scintillators that uses small PM tubes to reduce the overall size of the detector [17]. They have improved on this design by creating a smaller packaging and using smaller PM tubes. R. Aryaeinejad and D.F. Spencer reduced the size of the detector by using smaller planar socket PM tubes and used a Cockroft-Walton voltage multiplier circuit. The device was tested with two ^{252}Cf sources and was able to detect neutrons and gamma rays from a 1.4 μCi source at a distance of 60 cm; with a stronger 55.6 μCi source, the detection distance for neutrons and gamma rays was 500 cm [17]. The device operates on a single lithium ion battery and has a display to show real-time

counts per second to the operator [17]. The device operates in the same manner as the previous detector designed by R. Aryaeinejad, et al. using the difference between the ${}^6\text{Li}$ and ${}^7\text{Li}$ spectrums to discriminate neutrons.

As previously stated, the use of PM tubes can limit the overall size of the detector package; other groups have been investigating the use of other types of detectors that can potentially replace the PM tube for small portable systems. A relatively new type of device called the silicon photomultiplier (SiPM) is being explored for radiation detection. The SiPM is an avalanche photodiode operating in Geiger mode, which is divided into individual microcells, each with its own quenching resistor [18]. When a single photon is detected, a single pulse is produced by one microcell; when the array of microcells is hit by a larger light source, the amplitude of produced signal is proportional to the number of trigger microcells [18]. This type of device works as an analog photodetector for weak photon fluxes, since the amount of charge collected at the SiPM output gives the analog superposition of the binary signals produced by all triggered pixels [19]. The sensor offers many benefits such as very fast timing, good photon counting capabilities, high gain with low bias voltages, and high detection efficiency. [19]. These types of detectors, while smaller than traditional PM tubes, are not perfect replacements; the performance of the device is affected by dark current and the dark rate. The dark rate is defined as the number of avalanche current pulses produced by thermally generated electrons, which are indistinguishable from the detection of a single photon [18,20]. The SiPM also can suffer from after pulses and cross-talk between cells, especially when measuring very low light intensities [21].

D. J. Herbert, et al. has experimented with the use of SiPM detectors in conjunction with scintillators. The group used lutetium oxyorthosilicate ($\text{Lu}_2\text{SiO}_5:\text{Ce}^{3+}$ or LSO) crystals for the test scintillating medium, which is one of the most popular types of medium used in PET scan imaging [20]. The group found that the SiPM used did not detect any of the Compton scattering events that occurred within the scintillator due to the threshold limit of the detector. This resulted in the detection of gamma-ray energies that were significantly lower than what was expected for the scintillator being used and had a light collection efficiency that was as low as 7% [20]. They believe some better results can be obtained from adjusting the detection threshold and better detector/scintillator coupling.

R. Bencardino and J. E. Eberhardt are developing a fast neutron detector using SiPM for monitoring neutron flux in fast neutron/gamma radiography. The goal for the detector is the ability to handle high count rates and have a high damage threshold for longevity in high radiation flux environments. They used a neutron source with a fast neutron flux of up to 6×10^7 neutrons per second. Wavelength shifting fibers were used to couple the scintillator to the SiPM, allowing for the detector electronics to be separate and shielded from the neutron flux that the scintillator was exposed to. The SiPM detector was able to produce 4×10^4 useful counts per minute compared to a standard photodiode detector which produced only 160 counts per minute [22]. The SiPM detector was also compared to a traditional PM tube detector and showed comparable count rates [22]. They have stated that the device does have a temperature dependence, resulting large gain variation. They believe the solution to the problem is a system to adjust the bias voltage based on temperature variance. Another issue with this type of

device is the need for the detector to be separate from the scintillator because the radiation flux can damage the detector over time.

C. Stapels, et al. has been working on a gamma ray detector using SiPM detectors to replace PM tubes, allowing for a completely integrated CMOS device that is low-cost to optimize the functionality of scintillating materials. The group used LSO scintillators for gamma-ray detection paired with a SiPM detector. The group fabricated various SiPM detectors with different pixel spacings to compare cross-talk between pixels. The fabricated SiPM detector had a detection efficiency of about 20% after correcting for after pulsing [23]. Using a 150 micron spacing between pixels, the group was able to reduce crosstalk between cells to about 2% over the range of all bias voltages [23]. The group states that this type of device has the potential to be a CMOS compatible detector, but the size of the device affects the detection efficiency. Larger SiPM devices with more pixels will improve the detection efficiency, but it will also increase the background noise due to the cross-talk effect [24].

SiPM detectors are not the only type of semiconductor detector that is used for radiation detectors. PIN diodes with the addition of a conversion layer are also capable of neutron detection. C. H. Mesquita, et al. used a conversion layer of polyethylene (CH_2) as a conversion layer, which produces charge particles when the layer interacts with incoming neutrons. The charged particles from the interaction can then be detected by the PIN diode [25]. The effectiveness of the detector is dependent on the thickness of the conversion layer; the thicker the layer, the more neutrons that can be stopped by the material. But as the thickness of the layer is increased, the ability of the charged particles to escape the conversion layer and be detected by the diode is reduced. The recoil energy

of the charged particles is also affected by the incident angle of the incoming neutron [25].

Other types of conversion layers using ^{10}B and ^6Li have the ability to actually capture thermal neutrons within the layer. The captured thermal neutron interaction results in the emission of an alpha particle that can then be detected. D. McGregor, et al. experimented with thin film conversion layers but could only achieve low detection efficiencies of about 4.5% [26]. The low detection efficiencies of the thin films was attributed to the energy products (alpha particles) being re-absorbed by the conversion layer [27]. McGregor, et al. also experimented with using reactive ion etching to create 20 to 30 μm holes within the silicon detector and filling them with ^{10}B or ^6LiF . This device, though, also has a low detection efficiency of 3.8% [27]. The group does state detection efficiencies as high as 30% could be possible if the holes could be placed closer together and etched deeper into the silicon [27].

Other kinds of materials have also been experimented with to replace traditional silicon and germanium photodiodes. F. H. Ruddy, et al. has been investigating the use of silicon carbide (SiC) PIN diodes for fast neutron detection. The benefit to using the SiC diode over traditional diodes is that the SiC diode has a larger band gap (3.25 eV), allowing it to be used in high dose rates and high ionization environments [28]. Ruddy, et al. stated for low energy fission-neutron applications that it is possible to calculate the energy spectrum for the recoil ion based on the observed pulse height spectrum and range-energy calculations [28]. The problem with performing energy spectroscopy from the recoil ion is that the energy is dependent on the angle of incidents, which is unknown. The advantages of the SiC diode is that it can be used for applications in environments

that plastic scintillators and Si and Ge diodes cannot be used. S. Metzger, et al. conducted experiments using SiC detectors in harsh environments and compared it to the limits of Si and Ge detectors. Because of the large band gap, the SiC diode can operate at temperatures up to 200 °C with a good signal to noise ratio [29].

Gas based detector platforms are another type of device that is being reduced in size to create field portable detectors. One group has developed a glass and silicon microGeiger [30]. Wilson, et al. reports on a micromachined Geiger counter fabricated from stacks of glass and silicon wafers to create a double cavity device that is capable of energy spectroscopy of beta particles. The stacked geometry allows for energy discrimination of beta particles, which is not typical for ordinary Geiger counters [30]. As a beta particle enters the top cavity of the device, the fill gas is ionized by the particle and creates an electron cascade producing a signal. Higher energy beta particles are able to penetrate into the lower cavity of the device; this allows for the energy of the particle to be extrapolated by looking at the difference between the count rates of the upper and lower cavities [30]. The device only detects beta particles and has the potential to detect gamma rays by liberation of electrons from the cathode, but would not be able to discriminate between beta particles and gamma rays. C. Eun, et al. attempted to expand on the capabilities of the microGeiger by characterizing the RF emissions created when the electrons collect at the anode of the device. When the ionized electrons within the fill gas accelerate towards the anode, an RF signal is produced. The use of an RF receiver with the device would create a wireless microGeiger. The problem with the device was the RF emission was weak and the signal would fade as the distance between the detector and receiver was increased, limiting the range of device [31].

Another type of gas based detector is the micro-strip gas chamber (MSGC) invented by A. Oed in 1988. A. Oed published a paper on his device titled “Position Sensitive Detector with Microstrip Anode for Electron Multiplication with Gases” [32]. MSGC are designed by patterning alternating strips of anode and cathode materials. There is an insulated drift plane separate from the cathode and anode strips that sets up the electric field inside of the device. The size of the cathode strips range from 200 to 400 microns, while the anode strips are sized between 5 and 10 microns [33]. A bias voltage is applied to the anode, and by varying the distance between the strips, the gas multiplication of the device can be changed. The closer the strips are together, the higher the gas multiplication, resulting in higher pulse heights when detecting incident radiation. The distance between the strips cannot be so small that breakdown will occur between the anode and cathode because of the high electric field [33]. Spatial resolution can be done by individually reading each cathode within the device, which allows MSGC to be used for particle tracking in nuclear physics experiments.

To use a MSGC as a neutron detector, there must be an additional conversion medium added to the device. One popular conversion medium that is also used in proportional counters to detect neutrons is helium-3. T. Nakamura, et al. used a capillary plate filled with ^3He , placing it between the drift plane and the cathode and anode strips of the MSGC. The capillary plate consisted of tubes that were 100 μm in diameter with a spacing of 20 μm , and filled with ^3He at a partial pressure of 0.13 atm with the remainder filled with ^4He gas to a pressure of 3 atm [34]. The bias voltage that is applied to the capillary plate will affect the gas multiplication factor of the detector, so various bias voltages were tested. The drift plane was kept at a constant voltage of 3000 V with anode

biased at 200 V and the cathode at -150 V. The capillary bias voltage varied from 1500 to 2300 V, with the gas gain of the device increasing with an increase in capillary bias voltage. The device shows a 17% detection efficiency and a stable gas gain of about 600 [34]. The device can detect neutrons and is capable of spatial resolution, but the need for multiple negative and positive high voltage biases does not show much promise for a portable version. The main application of the device is focused on neutron scattering lab experiments.

Another type of electron amplification with gas based detectors was invented in 1996 called the GEM (Gas Electron Multiplier). F. Sauli developed the new electron amplification method using a planar anode and conductive mesh layers within the device to amplify and direct the electrons [35]. R. Bouclier, et al. later determined that the GEM could be used for radiation detection and can be fabricated using the same techniques as printed circuit boards. The device is made in three layers; the top and bottom are constructed of 18 μm layers of copper with a dielectric that is 25 μm thick separating the layers. Holes were etched that are 75 μm with a spacing of 100 μm . At a test voltage of -220 V, the device showed a gain of about 6 when exposed to a ^{55}Fe X-ray source [36]. The disadvantage to this device is the precision needed with layer alignment and lithography techniques, and the device showed little energy resolution.

J. Benlloch, et al. studied various GEM detectors that varied in size from 700 cm^2 to several centimeters squared with varying metal layer thicknesses. The metal layer thickness was varied from 5 to 15 μm with a dielectric layer of 50 μm between the metal layers. The group was able to show that the GEM detector was capable of gains around a 100 but also noted that other studies have provided gains of up to 1000. For applications

requiring the position of x-rays fields, a double sided circuit board could be used as the signal electrode, giving two dimensional spatial resolution [37].

G. Bencivenni, et al. experimented with using a multi-GEM detector for high rate charged particle detection. The group constructed a three stage GEM detector to achieve high gains while minimizing the probability of discharging within the device [38]. The group experimented with having a fast time response within the GEM to allow for high efficiency muon triggering. To achieve a fast time response, a special gas mixture of 60% Ar, 20% CO₂ and 20% CF₄ was used, and the group reported on an RMS signal distribution of about 5 ns [38]. The parameters of the GEM were also studied when exposed to a constant x-ray flux [39].

Another group has been studying neutron detection using GEM devices. For neutron detection, a conversion medium of ¹⁰B was used by S. Park, et al. to convert incoming neutrons into alpha particles. The GEM was a two stage device and used a 2.5 μm thick conversion layer. The ¹⁰B was thermally evaporated onto the bottom of the drift plane of the GEM [40]. The alpha particles emitted from the neutron boron interaction, ionize within the fill gas of the detector and are amplified by the two GEM stages. The group also put a boron coating on the GEM foils of the device and determined that the thickness of the foils has an effect on the detector efficiency [40]. The thicker the foil layers, the higher the potential for the created charged particle to be reabsorbed before exiting the material and ionizing within the fill gas.

In 2000, J. F. C. A. Veloso, et al. proposed a new type of detector that combined the design of the MSGC with its alternating cathode and anode strips with the GEM technology. The group called this new type of detector a microhole and strip plate

detector (MHSP) [41]. In a later publication Veloso, et al. discussed how this detector can be used for neutron detection. The group used a unique fill gas mixture in the device of 3-bar argon/50-mbar xenon/6-bar helium, stating that the mixture can achieve gains around 2×10^3 [42]. The group also reported that the mixture allowed for a 70% neutron detection efficiency for a 2.5 cm thick absorption region and intrinsic position resolution of about 1.7 mm [42]. The detector is also capable of gamma ray detection, but the ability to discriminate between the detected radiation species is missing.

There are various types of detectors available on the market today and at different stages of research development. The application of the detector usually dictates the type of detector needed. Field detectors offer additional challenges to detector designs because of the need for portability and remain robust and accurate enough to determine the isotope being detected outside of a lab setting. One method to provide this is to design a detector than can detect and discriminate between the four types of radiation particles in the field. Current detectors mainly focus on the detection of one specific type of radiation and leave the detection of other species to other detectors. By creating a single detector to detect all types of radiation, the need for multiple detectors is reduced, which reduces the cost and the amount of equipment in the field.

CHAPTER TWO

RADIATION PRINCIPLES

Nuclear materials emit several types of radiation species. To effectively design a sensor that is able to detect nuclear material, there is a need to understand the principles behind radiation sources and interactions. This chapter presents the basis behind the theories of atomic and nuclear radiation.

2.1 Radiation Sources

There are four main types of radiation sources that are divided into two categories: charged particles and uncharged particles. Charged particles consist of fast electrons and heavy charged particles. Examples of fast electrons are beta particles that are emitted from nuclear decay and other energetic electrons that are produced from radiation interactions. Heavy charged particles are energetic ions that have an atomic mass of one or higher; alpha particles fall into this radiation type. The category of uncharged particles includes electromagnetic radiation and neutrons. Electromagnetic radiation consists of X-rays, which are emitted from the electron shell of atoms, and gamma rays, which are emitted from the nucleus of the atom. Neutrons can be created from a variety of nuclear interactions and can be subdivided into slow and fast neutrons.

These four types of radiation are then further divided down into ionizing and non-ionizing. Radiation is called ionizing when it has enough energy to release an electron

from the atom. When the particle enters an absorbing medium, the charged particle interacts with many different electrons. Depending on how close the particle interacts with an electron, the force of the interaction may be enough to remove the electron from that atom, this is ionization, or it may just excite the electron to a higher energy shell, called excitation. If the radiation particle does not contain enough energy to release an electron from the atom, it is considered non-ionizing.

Radiological sources are defined by the rate of radioactive decay, the types of radiation emitted, and by the amount of energy they release. Radioactive decay is defined in Equation 2.1.

$$\frac{dN}{dt} = -\lambda N, \quad (2.1)$$

where N is the number of nuclei that are radioactive and λ defines the decay constant. The activity of a source can also be described by the length of the isotope's half life. The half life is the period of time it takes for the isotope that is decaying to lose half of its initial value. The exponential decay of a radioactive isotope is described in Equation 2.2.

$$N_t = N_0 \left(\frac{1}{2}\right)^{\frac{t}{t_{1/2}}}, \quad (2.2)$$

where N_t is the number of radioactive nuclei that remain, N_0 is the initial number of radioactive nuclei, t is the time that has passed, and $t_{1/2}$ is the half life of the decaying isotope. As an isotope decays, there is a possibility that daughter products are created whose activity will contribute to the overall radiation emitted from the source. Daughter products do not always emit the same type of radiation as the parent nucleus; this leads to sources that emit more than one form of radiation species. Depending on the type of decay that a source is undergoing, it will emit only a single species of radiation or it will emit a variety of species depending on the daughter products that are created in the decay.

The unit used for measuring radiation energy is the electron volt (eV). An electron volt is the amount of energy needed to move a single electron through a potential difference of one volt.

2.1.1 Alpha Particle Sources

Alpha particles fall under the category of heavy charged particles and are typically emitted from heavy nuclei. An alpha particle consists of two protons and two neutrons that are bonded together forming a helium nucleus, ${}^4\text{He}$. Heavy nuclei are unstable because of the high ratio of protons to neutrons within the nuclei. The heavy nuclei undergo alpha decay, releasing alpha particles and reducing the number of protons within the nucleus of the parent atom which brings the atom to a more stable state. Equation 2.3 describes the process for alpha decay.



where X is the initial nuclear species (parent) before decay and Y is the final species (daughter product) once decay has occurred. Looking at the equation, we can see that when the initial species undergoes decay it loses two protons in the process, reducing its atomic number by two, meaning the decaying atom becomes a new element. An example of this is Radium (${}_{88}\text{Ra}$) which undergoes alpha decay becoming Radon (${}_{86}\text{Rn}$).

The energy released from the decay is divided between the two products with an inverse proportion to their masses. Both the daughter product and the alpha particle have the same momentum after the decay occurs and are traveling in opposite directions. Since the mass of the alpha particles is much less than the daughter product, the particle travels much faster. Alpha decay within a source occurs at discrete energies that are particular to the type of atom undergoing the change. Because of the way that the energy

is shared between the alpha particle and the daughter nucleus, all the alpha particles appear at the same energy level. In some cases, depending on the atom undergoing decay, the particles will appear at more than one energy level, but these energies will not be over a range of values but at specific discrete values.

Alpha sources have a large range of possible half-lives. Some sources have a half-life of thousands of years while others have a half-life of days. The energy of a source has a large correlation to the length of its half life. Sources that have large energies (above 6.5MeV) typically will only have a half-life of days because of the high rate at which they emit alpha particles, which limits their usefulness. Sources that have a longer half-life emit particles at lower energies (below 4 MeV), but these also have limited usefulness because of their intensity level. A common alpha source that is used for calibrations is ^{241}Am ; which has a half-life of 433 years and emits alpha particles at 5.48 MeV and 5.44 MeV.

2.1.2 Beta Particle Sources

Beta particle radiation is the most common type of fast electron emission; this type of radiation is emitted from the nucleus of the atom. Beta decay occurs when the number of neutrons and protons inside of the nucleus of atom is unbalanced. There are two forms of beta decay, beta minus (β^-) and beta plus (β^+). Beta minus is the most common type of emission; it occurs when a neutron inside of the nucleus is converted into a proton. Beta plus works in the opposite way. If there are more neutrons inside of the nucleus, some become transformed into protons to bring the atom's nucleus to a more stable state. The process for beta minus decay is given in Equation 2.4.



where X is the parent species, Y is the daughter product, and $\bar{\nu}$ is an antineutrino. The production of an antineutrino along with the fast electron occurs because of the need for the conservation of mass, energy, and charge in the decay process. In the process of beta plus decay, a proton is converted into a neutron along with a positron and neutrino, shown in Equation 2.5:



The process of beta plus decay absorbs energy in the conversion of a proton to a neutron, while in beta minus decay energy is released when the uncharged neutron is converted into a smaller charged proton. Since the energy of the system has to be conserved, the released energy is divided between the daughter nuclei, the fast electron, and the antineutrino. The daughter nucleus typically only has a small amount of recoil energy which is below the threshold of ionization. The mass of an antineutrino is less than one two-thousandth of an electron and can essentially be said to have zero mass [43]. The energy of the antineutrino is practically undetectable because the antineutrino is so small it has a very low probability of interacting with matter. This leaves the rest of the kinetic energy from the interaction being deposited into the beta particle being emitted, giving the particle a high velocity.

It is possible for some beta sources to emit more than just pure beta radiation. When the source undergoes beta decay, it is possible for the parent or daughter nuclei to raise to an excited state; as result of the nuclei transitioning back to the ground state, gamma rays are released along with the beta particle. If the parent and daughter nuclei stay at the ground state when undergoing beta decay, the source is a pure beta emitter. Each type of beta decay is characterized by a fixed decay energy that can range anywhere

on the spectrum from zero up to an end-point energy or Q-value specific to the source. The beta particle's energy is dependent on the amount of energy that is shared between the beta particle and the undetected antineutrino. The beta energy spectrum of ^{36}Cl is shown in Figure 2.1.

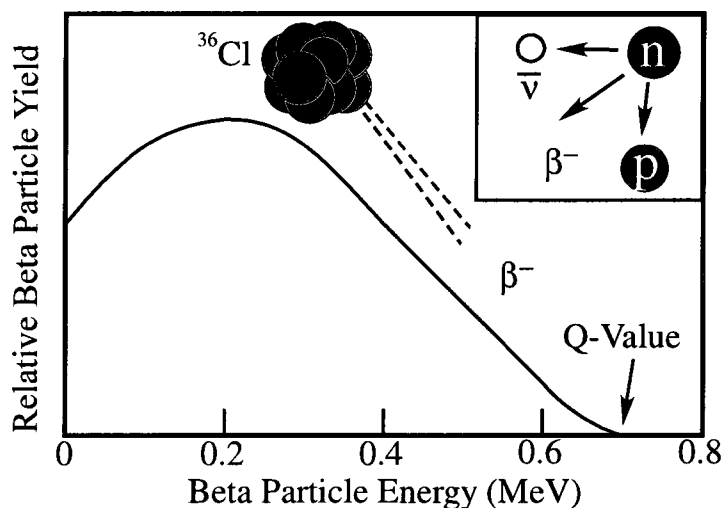


Figure 2.1 ^{36}Cl energy spectrum.

The Q-value for specific types of decay is normally given assuming that the decay takes place between the ground states of the parent and daughter nuclei. If the decay involves the excited state of the parent or daughter nuclei, then the multiple end-point energies can occur from the source.

2.1.3 Electromagnetic Radiation Sources

Gamma rays and X-rays are two major types of electromagnetic radiation we are concerned with detecting. Each is produced in a different way; gamma rays are produced in a nuclear reaction, and x-rays are caused by the removal or excitation of the orbital electrons. Electromagnetic radiation consists of photons with an energy described in Equation 2.6.

$$E_p = h\nu = \frac{hc}{\lambda}, \quad (2.6)$$

where E_p is the energy of the photon, h is Planck's constant (4.135×10^{-15} [eV•s]), ν is the frequency, λ is the wavelength, and c is the speed of light. Electromagnetic radiation includes a wide spectrum from radio waves to visible light, to x-rays and gamma rays, but from Equation 2.6 only electromagnetic radiations with short wavelengths will produce high energy photons. With the production of high energy photons comes the possibility that the radiation will ionize.

As previously mentioned, gamma rays can be emitted in the process of beta decay. Gamma radiation is emitted by the excited parent or daughter nuclei transitioning to lower nuclear levels. This type of gamma radiation is commonly used for sources in testing radiation detectors. An example of a common source used for this is ^{60}Co . The beta decay of ^{60}Co leads to daughter nuclei at excited states which emit two gamma rays as the nuclei release energy to fall back down to its ground state (Figure 2.2).

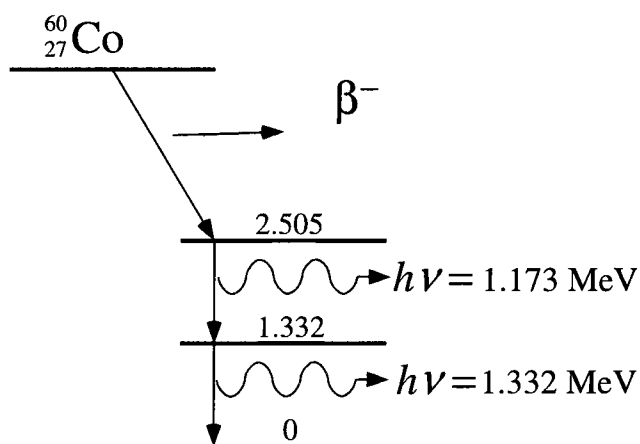


Figure 2.2 Decay scheme of ^{60}Co .

The de-excitation of the daughter nuclei emits a gamma ray photon whose energy is almost equal to the energy difference between the initial excited nuclear state and the final nuclear state.

Gamma rays can also be emitted from what is known as annihilation radiation. Annihilation radiation occurs when the parent nucleus undergoes beta plus decay and a positron is emitted from the decay process. The positron only can travel a few millimeters before losing its energy. The emitted positron combines with a normal electron in an absorbing material in the process call annihilation. The positron and electron combination disappears and is replaced by two gamma rays who are directed away from each other whose energy is 0.511 MeV. This type of gamma radiation produces an energy peak of 0.511 MeV superimposed over gamma radiation produced by the daughter product of subsequent beta decay.

Gamma rays can also occur following a nuclear reaction; the types of gamma rays emitted from these reactions are much higher energy than those that occur from beta decay. This type of emission occurs with an alpha particle interacting with a target material. When the alpha strikes the target a new element is produced along with a neutron. The daughter nuclei that result from the interaction are at an excited state and fall back to the ground state producing a high energy gamma ray. High energy gamma rays can also occur after a nucleus absorbs a thermal neutron. A “neutron-capture gamma ray” typically has energy ranging as high as 9 MeV [2].

When atoms become excited or energetic, electrons respond by moving to higher orbital shells to compensate for the increased energy. After the electrons move to higher shells, they rearrange themselves and fall back to their previous state releasing the extra

energy. The extra energy that is released comes in the form of characteristic x-rays. The energy of the released x-ray depends on which two shells the electron transitions between. The highest energy x-rays occur when an electron transitions from an upper shell down to the K-shell, which is the shell closest to the nucleus. Figure 2.3 shows the different types of x-ray energies that can be emitted from an electron transitioning down between shells.

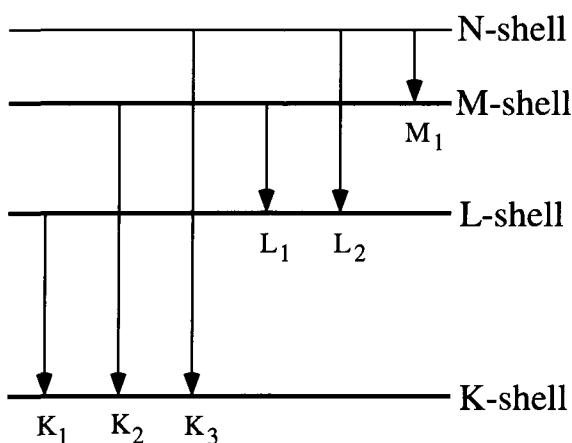


Figure 2.3 Possible electron orbital transitions.

Higher Z elements have more shells at which an electron can be energized to resulting in stronger x-rays being emitted when the electrons rearrange and fall back to their lower energy shells.

There are several ways that an atom can become excited leading to the release of x-rays. One method is from radioactive decay by internal conversion or electron capture. Internal conversion consists of the daughter nuclei de-exciting with release of a gamma ray or K-shell electron of an atom creating a vacancy in the shell. In electron capture, an electron in the K-shell is absorbed by the nucleus of an atom, again leaving a vacancy in the K-shell. As a result of this vacancy, an electron from a higher orbital fills in the

vacancy in the K-shell releasing x-rays in the process. Another method of x-ray production is excitation by external radiation. An external source of radiation is used to excite a target material, and when the source is removed, the target material will release this energy in the form of x-rays. As stated previously, if the target is a high Z element, then it will have more shells for the excited electrons to move into and produce higher energy or “harder” x-rays, as compared to a low Z element, which has limited shells available to excite electrons into producing lower energy or “soft” x-rays.

2.1.4 Neutron Sources

Neutrons are the uncharged particles that are found within the nucleus of atoms. Due to a strong binding energy, neutrons are not typically released from atoms through conventional radioactive decay. Neutrons can be emitted from the nucleus of an atom either through spontaneous fission or by nuclear reactions.

In the process of spontaneous fission, a heavy nucleus splits into two smaller nuclei and several by-products, which include beta particles, gamma rays, and one or more neutrons. For a source to be used as a neutron source, it must be enclosed in a container that will block the charged particles from escaping. The emitted neutrons can take on a variety of energies because the total energy of the reaction is shared between all of the products. The most commonly used neutron source that uses spontaneous fission is ^{252}Cf .

Nuclear fission of heavy elements, such as ^{239}Pu , is an exothermic reaction which releases large amounts of energy in the form of electromagnetic radiation and kinetic energy. This type of reaction gives the ability to create nuclear power as well as nuclear weapons. A nuclear reaction can be self sustaining when neutrons emitted from fission

are absorbed by other heavy nuclei which then undergo fission, emitting more neutrons in a chain reaction. This chain reaction can be at a controlled rate, which is used in nuclear power or at an uncontrolled rate in nuclear weapons.

Nuclear radiation can also be produced through several different nuclear reactions using a radiation source to excite the nucleus of a target material. Alpha particles and gamma rays are used to excite target a material such as ${}^9\text{Be}$. Alpha emitting isotopes bombarding a ${}^9\text{Be}$ target is one of the most commonly used sources because of the high neutron yield of the reaction. The reaction is shown in Equation 2.7:



The number of neutrons produced in the interaction is determined by the energy of the alpha particles and the thickness of the beryllium target. When the target is thick relative to the range of the alpha particles, most of the particles are just stopped by the target; only about 1 in 10,000 alpha particles will interact with the nucleus of a target atom producing a neutron. Because of the low probability of a neutron being produced, a highly active alpha source, such as ${}^{241}\text{Am}$, is used to increase the number of neutrons being emitted from the target.

Photoneutron sources use gamma rays to release a neutron from the target material. The gamma rays are used to excite the target atom by absorbing the gamma ray photon allowing for the emission of a free neutron. Two of the most commonly used reactions are given in Equations 2.8 and 2.9:



The energy of the neutron released in these reactions has an energy that is directly related to the energy of the gamma ray used to release the neutron. If the gamma rays used are mono-energetic, the neutrons that are emitted will also be nearly mono-energetic, since there is only a small variation in energy transfer due to the angle of the gamma ray interaction.

There is a third type of nuclear reaction that is based off of accelerating charged particles. For this type of reaction, ionized deuterium is accelerated by a potential of 100 to 300 kV to a deuterium or tritium target. The reactions are given in Equations 2.10 and 2.11:



The reactions result in neutrons being produced at about the same energy for each interaction. The deuterium/deuterium reaction produces 3.26 MeV neutrons while the deuterium/tritium reaction produces 17.6 MeV neutrons.

2.2 Radiation Interactions with Matter

Each type of radiation species interacts differently when they enter the detector medium. The interactions of each species depend on the type of radiation, the energy of the particle, and the material of the absorber. The absorbing range of a medium depends on the overall thickness of the absorber and the type of elements that make up the material; these factors determine how much energy the particle will transfer to the medium, ranging from all of its energy to none at all.

2.2.1 Alpha Particle Interactions

Alpha particles primarily interact with matter through Coulomb forces between the positive charge of the alpha particle and the negative charge of the orbital electrons within an absorbing medium. As the alpha particle enters the medium, it interacts with many electrons simultaneously. Two types of interactions occur depending on the distance between the particle and electrons it is interacting with; it may excite the electron to a higher energy state within the atom, or it can remove it completely from the atom (ionization). The alphas are heavy particles and have a linear path through the medium because the pull from the orbital electrons is from all directions. The particle will continue to travel through the medium until it dissipates all of its energy. The stopping power of an alpha particle in an absorbing medium can be described by Equations 2.12 and 2.13.

$$S = -\frac{dE}{dx} = \frac{4\pi e^4 z^2}{m_0 v^2} NB, \quad (2.12)$$

$$B \equiv Z \left[\ln \frac{2m_0 v^2}{I} - \ln \left(1 - \frac{v^2}{c^2} \right) - \frac{v^2}{c^2} \right], \quad (2.13)$$

where S is the stopping power, v is the velocity of the primary particle, ze are the charge of the particle, N is the number density, Z is the atomic number of the absorber atoms, m_0 is the electron rest mass, I is the ionization potential of the absorber, and c is the speed of light. As the particle penetrates deeper into the absorbing medium the stopping power increases, due to the energy transfer from the charged particle to the electrons of the absorber. As the particle slows down, more energy is transferred to the surrounding electrons because the particle and the nearby electrons have more time to interact. Higher energy particles have larger velocities and are able to penetrate deeper into an absorber.

The distance that alphas can penetrate into an absorber is called the range. Because alphas have a linear path through a medium, the amount of particles reaching a detector on the other side of a medium is constant. The particles are able to travel through the medium until it reaches a critical thickness where the number of alpha particles passing to the other side rapidly drops shown in Figure 2.4.

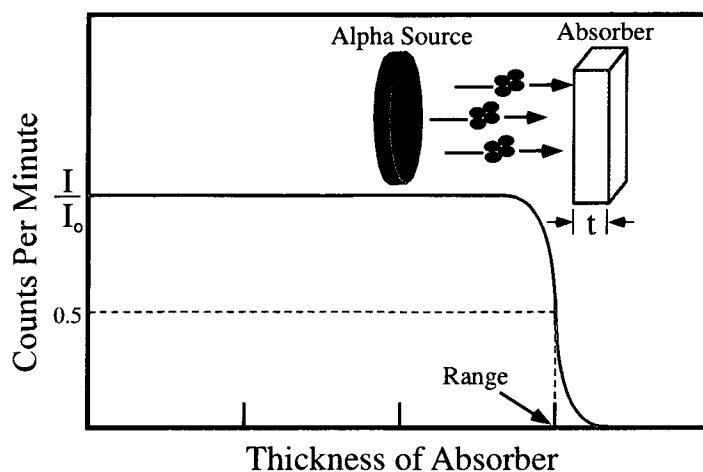


Figure 2.4 Range of alpha particles.

The range of an absorbing medium is determined by the thickness needed to reduce the number of alpha particles passing through by half of their initial value; at this point, transmission of the particles is rapidly attenuated. Absorbing mediums that are made of higher Z elements have a higher stopping power and decrease the thickness needed to stop alpha particles.

2.2.2 Beta Particle Interactions

The beta particles passing through an absorbing medium react with the orbital electrons of the absorber's atoms through columbic forces. When you compare the beta particle interaction to the interaction of the larger alpha particles within the medium, the beta particles lose their energy at a much lower rate because of their smaller size. Unlike

alpha particles, beta particles do not travel a linear path through the medium. Since the size of beta particles is similar to the size of the orbital electrons, they can lose more energy per encounter and have path deviations within the material.

The specific energy of beta particles contains two parts, the Coulomb force interactions, $\left(\frac{dE}{dx}\right)_c$, and Bremsstrahlung or electromagnetic radiation interaction, $\left(\frac{dE}{dx}\right)_r$. The electromagnetic radiation occurs from the acceleration of the beta particle in the absorbing medium as it interacts with the orbital electrons. The summation of these two parts gives the overall stopping power of an absorber which is defined in Equations 2.14, 2.15, and 2.16.

$$S = \frac{dE}{dx} = \left(\frac{dE}{dx}\right)_c + \left(\frac{dE}{dx}\right)_r, \quad (2.14)$$

$$-\left(\frac{dE}{dx}\right)_c = \frac{2\pi e^4 NZ}{m_0 v^2} \left(\ln \frac{m_0 v^2 E}{2I^2(1-\beta^2)} - (\ln 2)(2\sqrt{1-\beta^2} - 1 + \beta^2) \right. \\ \left. + (1-\beta^2) + \frac{1}{8}(1-\sqrt{1-\beta^2})^2 \right), \quad (2.15)$$

$$-\left(\frac{dE}{dx}\right)_r = \frac{NEZ(Z+1)e^4}{137m_0^2c^4} \left(4 \ln \frac{2E}{m_0c^2} - \frac{4}{3} \right), \quad (2.16)$$

where S is the stopping power, N is the number density, Z is the atomic number of the absorber atoms, m_0 is the rest mass of an electron, I is the ionization energy, e is the charge of the primary particle, c is the speed of light, and $\beta \equiv \frac{v}{c}$.

The transmission of beta particles through an absorbing medium differs significantly when compared to alpha particles due to the non-linear path beta particles travel. Beta particles that have a lower energy are quickly absorbed by materials that have small thicknesses; this leads to a much greater initial drop off of the number of betas that can pass through the absorber and reach a detector on the other side (Figure 2.5).

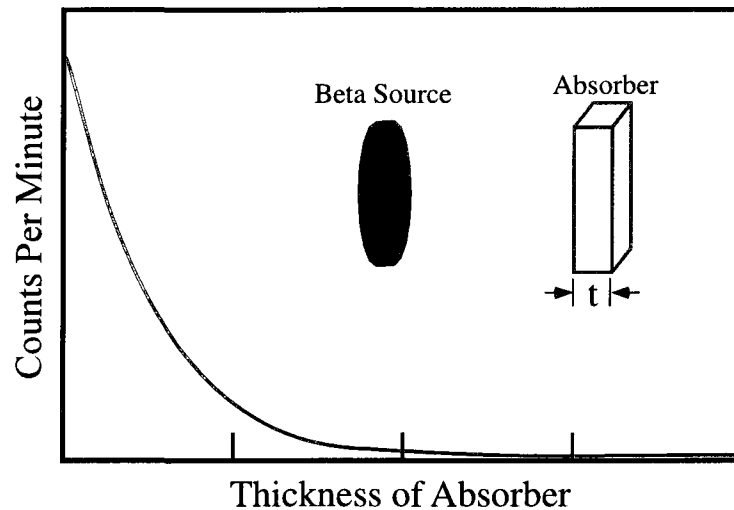


Figure 2.5 Range of beta particles.

As the thickness of the absorber increases, more beta particles are scattered by interactions with the absorber atom's orbital electrons, causing the particles to not reach the detector. For most beta particles sources, the range of the beta particles follows a curve approximated in Equation 2.17.

$$\frac{I}{I_0} = e^{-nt}, \quad (2.17)$$

where I is the counting rate with the absorber, I_0 is the counting rate without the absorber, t is the thickness of the absorber in g/cm^2 , and n is the absorbing coefficient. The curve models an exponential decay because of the lower energy betas being more rapidly absorbed by the medium leaving only higher energy betas passing through to the detector.

2.2.3 Electromagnetic Interactions

Gamma rays and X-rays interact with matter in many different ways, but for the purpose of measuring and detecting this type of radiation, only three ways are of importance: the photoelectric effect, Compton scattering, and pair production. Each of these processes leads to the photon energy being partially or completely transferred to

electron energy, which is important when trying to detect electromagnetic radiation. After the energy transfer occurs, the photon either will disappear or will be scattered, changing its path completely. This type of interaction differs greatly from the previously discussed particles where the particle slowly loses energy as it passes through the absorbing medium.

In the photoelectric effect, the photon energy of a gamma ray will interact with an absorber atom as a whole, and the photon will completely disappear. The photon, given that it has enough energy, will usually interact with the innermost shell of the atom, ejecting an electron from the shell. The electron is ejected with a kinetic energy given in Equation 2.18.

$$E_{kin} = h\nu - E_b , \quad (2.18)$$

where E_{kin} is the kinetic energy of the liberated electron, $h\nu$ is the energy of the gamma ray and E_b is the binding energy of the orbital electron. This interaction also leaves a vacancy in the shell of the absorber atom, which is then filled by outer electrons or the capture of free electrons in the medium. The process of filling the shell will emit one or more characteristic x-rays.

In Compton scattering, the gamma ray photon can interact with any of the orbital electrons in the absorbing atom. This type of interaction is the most common type for gamma ray sources. The incoming photon collides with an orbital electron of the absorbing atom and can transfer from zero to all of its energy to the electron. The collision results in a large path change for the photon, and the electron is ejected from the atom with energy proportional to the angle of photon deflection (Figure 2.6).

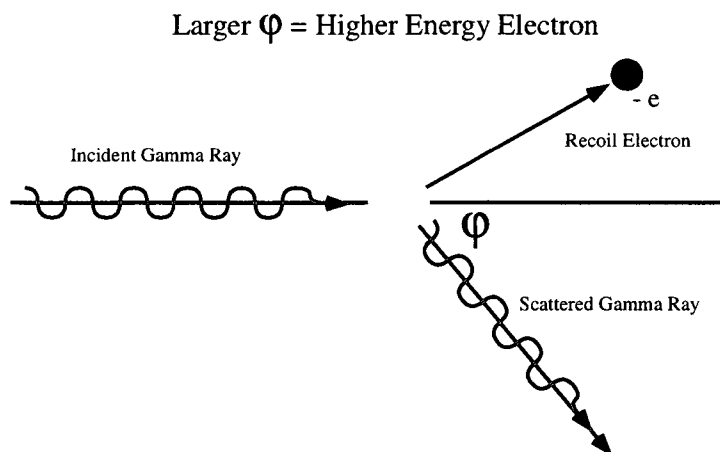


Figure 2.6 Compton scattering.

For small angles of ϕ , little energy is transferred to the orbital electron. After the interaction, the redirected photon can either interact again with another electron transferring more of its energy or be deflected completely out of the absorbing medium. The probability of Compton scattering increases with high Z elements because the number of orbital electrons to interact with increases.

Pair production only occurs with high energy gamma rays; the gamma ray must be at least twice the energy of the rest mass energy of an electron (1.02 MeV). Once this amount of energy is reached, the probability of pair production is still very low until the gamma rays reach energies of several MeV. In this type of interaction, the gamma ray photon disappears, and its energy goes into an electron-positron pair. Once the pair is created, the positron is quickly absorbed through annihilation, producing two annihilation photons, which result in two more gamma rays. The fast electron from the pair is able to escape the medium and be detected, resulting in pulse heights of various energies.

The attenuation of gamma rays and x-rays through a medium can be described by an exponential function given in Equation 2.19.

$$\frac{I}{I_0} = e^{-\mu t}, \quad (2.19)$$

where I_0 is the original number of gamma rays from the source, I is the number of gamma rays being detected, μ is the attenuation coefficient, and t is the absorber thickness. The attenuation coefficient is a summation of the probability of the three previously discussed interactions occurring. High Z absorbing elements will have a higher attenuation coefficient, resulting in a higher stopping power for gamma rays and x-rays.

2.2.4 Neutron Particle Interactions

Like gamma rays, neutrons carry no charge and do not interact with matter through Coulomb force, which is the dominate factor for charged particles and electrons in losing their energy from an absorbing medium. When neutrons do interact with an absorbing atom, it is with the atoms nucleus, where either the neutron will be absorbed and secondary radiation species will be emitted or the direction and the energy of the neutron will be changed dramatically. Neutrons are divided into two types depending on the amount of energy they carry. Slow neutrons have an energy that is below 0.5 eV, while they are considered fast neutrons if their energy is above 0.5 eV.

When neutrons enter an absorbing medium, they do not always interact with the atoms of the absorber; some pass completely through with no interaction at all. The neutron cross section of a material is a term used to describe the probability of neutrons interacting with the absorber. This cross section is dependent on the energy and amount of neutrons entering the absorber, as well as the quantity and type of nuclei in the

absorber. The better the neutron cross section of an absorber, the higher the probability of interactions with neutrons passing into the medium.

Slow neutrons interact with the absorber through elastic and inelastic scattering. The probability of elastic collisions of the neutron and the absorber nuclei is very high, and this collision acts to bring the slow neutron into equilibrium with the absorber. The thermal neutron with energy of about 0.025 eV can then undergo capture, which will result in the release of gamma rays or heavy charged particles. Since the gamma rays that result from neutron interactions are still hard to detect, it is more desirable to have an absorber material that results in a neutron/alpha, neutron/proton, or neutron/fission reaction.

Fast neutron interactions are dominated by elastic scattering with the production of recoil nuclei being produced in the collisions. The recoil nuclei pick up detectable amounts of energy from the neutron collision. With each collision, the neutron loses energy and starts to slow down, eventually becoming a slow neutron and undergoing a nuclear reaction. The most effective moderator for neutrons is hydrogen because it is possible for the neutron to lose all of its energy from a single collision with a hydrogen nucleus.

Transmission of neutrons through a medium has a similar attenuation as gamma rays and x-rays. Neutron attenuation is given in Equation 2.20.

$$\frac{I}{I_0} = e^{-\Sigma t} , \quad (2.20)$$

where I_0 is the original number of neutrons from the source, I is the number of neutrons being detected, Σ total number of all possible cross sections in an absorber, and t is the absorber thickness.

CHAPTER THREE

RADIATION DETECTORS

There are three main types of detectors that are used for radiation detection: gas based, solid state semiconductors, and scintillator detectors. For radiation detection to occur in any of these detectors, the radiation must undergo an interaction through one of the methods previously discussed in Chapter 2. This chapter presents details on all three detection methods currently in use.

3.1 Gas Based Radiation Detectors

There are several different types of gas based radiation detectors that are classified by the region they operate within and the amount of applied voltage. The three main types of gas based detectors are ionization chambers, proportional counters, and Geiger-Müller counters. Radiation absorption in a gas based detector is dependent on an electrostatic field created between the chamber wall (cathode) and a positive electrode (anode) placed near the center axis of the chamber. The chamber can be filled with many different types of gases including air, helium, argon, xenon, and neon; the fill gas can either be at atmospheric pressure or can be pressurized to increase radiation interactions. The primary mode of interaction involves the ionization and excitation of the gas molecules along the path of the radiation particle [2]. Ionization of the gas by radiation consists of the removal of one or more electrons from one or more gas molecules

allowing formation of positive ions and free electrons [44]. The behavior of the charged particles after the initial formation is dependent on the gas and the electric field inside of the chamber. Figure 3.1 shows the different operating regions of gas based detectors with radiation particles of two different energies.

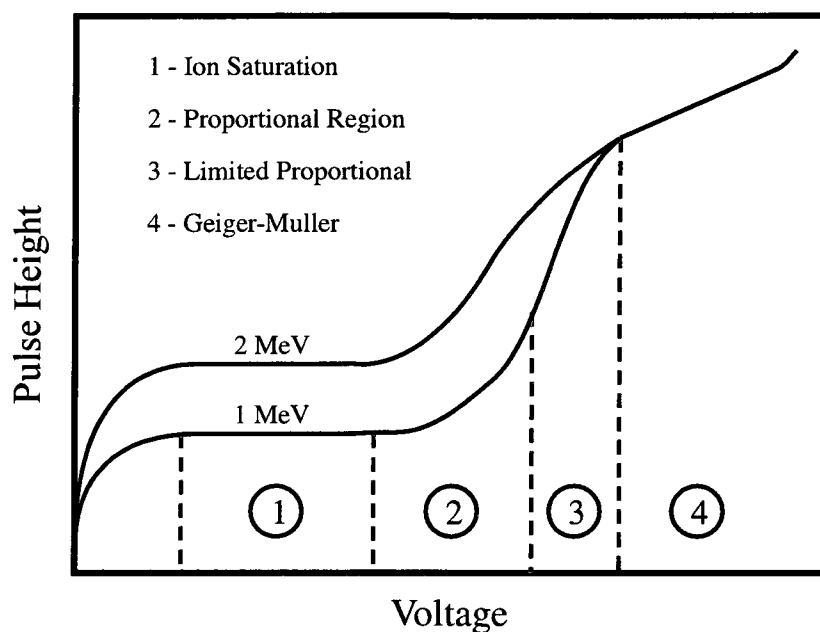


Figure 3.1 The different operating regions of gas-filled detectors.

The ion saturation region shows constant pulse heights for radiation sources that have a constant energy; this is the operating region of ion chambers. In the proportional region, the electrons have enough energy to ionize atoms of the fill-gas. They begin to multiply by creating additional ion pairs and have a pulse amplitude that is proportional to the original particle energy. In the Geiger-Müller region, pulse heights are not distinguishable from each other because of liberated electrons forming a cascade of more electrons, and pulse heights are not dependent on the original energy.

3.1.1 Ionization Chamber

The principles of the ionization chamber are simplest of the gas based detectors. The operation of an ionization chamber is based on the collection of all the charges that are created by direct ionization within the gas when an electric field is applied. Ion chambers can be operated in both current and pulse mode. The most common mode of operation is current mode as a DC device, where proportional and Geiger counters typically always operate in pulse mode.

When fast charged particles pass through gas, the interactions that were previously discussed create ionized molecules along its path. The resulting ionization creates a positive ion and free electron called an ion pair. The ions can be formed either from a direct interaction with a gas particle or through a secondary interaction process where some particle energy is deposited into an energetic electron. When a particle passes through a gas, not all of the energy transferred results in ion pairs. There are other types of interactions that can occur. The amount of ion pairs formed for specific particle energy is dependent on the type of gas being used inside of the chamber. Tests have shown the amount of ion pairs that form for a specific energy is a constant parameter for many gases, allowing for the particle energy to be determined from the number of pairs formed [2].

3.1.2 Proportional Counter

Proportional counters are typically operated in pulse mode and use gas multiplication to amplify the charge created by the formation of the ion pairs inside the gas. The pulses that are created are much larger than what is created inside of a simple ion chamber, but the multiplication that occurs in the chamber stays in proportion to the

particle energy that is being detected. Proportional counters are useful for ion pairs generated by radiation that are very small and are not easily detected by pulse mode ion chambers.

Gas multiplication inside of a proportional counter occurs because of the increased electric field inside of the chamber. When a chamber has a low electric field, the ion pairs that are created from incident radiation will drift through the gas to the collecting electrodes. As these pairs are drifting through the gas, they go through many collisions, but little energy is transferred. When a larger potential field is present, the free electrons created by the ion pairs can be accelerated and begin to have a more kinetic energy. If the accelerated electron has more energy than is needed to ionize the gas molecules, then additional ion pairs are created in these collisions. As additional ion pairs are created, these new free electrons are also accelerated by the electric field, creating even more ion pairs. One parameter that affects the number of ion pairs created is the multiplication coefficient of the fill gas in the detector. In a proportional counter the number of ion pairs produced per radiation interaction is a function of the primary radiation interaction energy.

As the electric field is increased inside of the chamber, a non-linear proportional counting region can start to occur. This happens because as the ion pairs are formed, the time it takes for the positive ions to be collected compared to the time it takes for free electrons to be collected starts to increase. This can cause a buildup of positive ions inside the chamber, which will affect the electric field inside of the chamber. Since the gas multiplication is dependent on the electric field, a non-linear amplification is created and is called the limited proportional region.

3.1.3 Geiger-Müller Counter

Geiger counters are another type of gas based detector that relies on gas multiplication. Geiger counters are the most popular type of gas based detector because they offer a high sensitivity, are able to detect different types of radiation, come in a large variety of sizes and configurations, and provide a large output signal.

Geiger counters differ from proportional counters in the way the gas multiplication and electric field is used. Proportional counters rely on gas multiplication that creates ion pairs that are a function of the original energy of the incident radiation particles. Geiger counters use a significantly higher electric field to increase the kinetic energy in the free electrons. This increase in kinetic energy increases the number of the secondary ion pairs (an avalanche of electrons) that are produced in the gas. The large increase in energy and ion pairs produced allows additional separate avalanches to start to occur independent of the first avalanche. At a critical value of the electric field, each avalanche that is created will create at least one more avalanche, creating a self propagating reaction in the chamber [2]. Once this discharge reaches a specific size, the effect of all the discharges builds up and eventually stops all of the reactions. Since the limiting point is always reached around the same number avalanches, the pulse energy is independent of the initial radiation energy. The Geiger counter gives no information of the initial particle energy. Because of this effect, the Geiger counter can only be used to count radiation events and cannot be used to determine the specific radiation particle energies.

3.2 Solid State Detectors

Solid state or semiconductor detectors are another type of detector that is commonly used to detect multiple kinds of radiation particles. When compared to gas based detectors, the detector dimensions of semiconductor detectors can be much smaller and provide the same detection ability of high energy electrons. This is due to the densities of the solid state detectors, which are about 1,000 times greater than that of gas [2]. Other features of semiconductor detectors, other than their smaller size, are they have relatively quick timing characteristics and the thickness of the material can be changed to match the application requirements. Disadvantages to using semiconductors are that they are limited to small sizes and their performance can become degraded over time due to radiation damaging the crystal structure of the substrate. There are various materials that can be used for solid state detectors; the most commonly used materials are silicon and germanium.

Solid state detectors are crystalline structures that consist of many different energy bands and gaps of forbidden energy ranges inside of the material. The electron energy inside of a semiconductor must be within one of these bands. The bands are separated into two types: the valence bands and the conduction bands. The valence band is the area inside of the semiconductor where outer shell electrons are bound to specific areas inside of the crystal lattice. The conduction band is a higher energy band that allows the electrons within it to move around the crystal lattice and do not confine the electron to specific areas. Electrons in the conduction band contribute to the electrical conductivity of the material. The valence and conduction bands are separated by a band gap. The band gap is the amount of energy required to excite an electron from the

valence band into the conduction band. Different materials have different band gaps; the size of a band gap determines whether a material is a semiconductor or insulator. The band gap for silicon is 1.1 eV, germanium is 0.67 eV, and the band gaps for insulators are typically greater than 10 eV.

Intrinsic semiconductors are not typically used in practice; instead these semiconductors are doped with different concentrations of impurities. The two most common impurities used for silicon is boron (n-doped) and phosphors (p-doped). Adding boron to the silicon adds more electrons in the material to be available for the conduction of an electric current (n-type semiconductor). The addition of phosphors introduces more holes in the semiconductor that are available for conduction (p-type semiconductor). Both the flow of negatively charged electrons and positively charged holes contributes the conductivity of an intrinsic semiconductor.

Semiconductor detectors rely on the creation of electron hole pairs in the material when radiation particles interact with the substrate. The energy lost by a charged particle inside of a semiconductor is divided between the excitation of lattice vibrations and the production of electrons and holes in the material [45]. When radiation interacts with a semiconductor material, the energy transfer results in an equal number of electrons and holes created in the material. Practical applications of semiconductors for radiation detection use more than one type of semiconductor material. A P-N junction is a commonly used topology. A P-N junction has a p-type semiconductor connected to an n-type semiconductor. Because of the difference in charges of the two materials, the electron in the n-doped side of the junction will want to migrate into the p-type semiconductor, while the holes from the p-doped material will migrate into the n-type

semiconductor. The region at the interface is known as the depletion region and is used as the radiation absorbing region in the junction. The depletion region is increased by applying a reverse biasing voltage to the junction. As radiation enters the depletion region, the electron hole pairs are swept to their respective electrodes by the electric field present in the junction. Collection time within the detector is on the order of nanoseconds which make for very fast detection rates. Semiconductor detectors can be used for energy spectroscopy because energy of the radiation particle induces a proportional number of electron pairs in the semiconductor.

Solid state detectors are limited to small sizes due to the size of the depletion width that can be created with the use of high voltages. Their small size works well for low penetration radiation, like alpha particles, where they can completely absorb the particle. They do not work as well for high penetrating radiation, such as gamma rays. The depletion region depth is what affects the ability of the detector to stop the gamma ray. One method to increase the depletion region is to lower the concentration of doping impurities. For this application high purity germanium is used because it has a very low impurity level and has a high level of mobility for hole and electrons when it is compared with silicon.

As stated before, one major disadvantage that comes with using solid state detectors is the problem of radiation damage. For solid state detectors to have a proper operation, the crystal structure of the material must be an almost perfect lattice. Over time there will be radiation damage to the lattice structure due to the lattice vibration introduced by the radiation energy. Eventually the device starts to exhibit more leakage current and starts to have less energy resolution.

3.3 Scintillator Detectors

Scintillator detectors do not use the production of ion pairs, electrons, or holes like gas based and solid state detectors use for the detection of radiation particles. Scintillators are based off of the process of photon production when the radiation particles interact with the detecting medium. Scintillators, discovered in 1903, are one of the oldest techniques used for the detection of radiation [46]. Initially scintillators were used with microscopes and the user would sit at the microscope and count the number of fluorescence that occurred over a period of time. This method was not very efficient until the introduction of the photomultiplier tube in 1944, which replaced the microscope and the user's eyes for counting the radiation interactions.

Scintillators have many properties that are desired for efficient operations. They need to have high scintillation efficiency for converting the energy of a radiation particle into a measurable light signal. The conversion of the radiation energy into a light pulse needs to be a linear function. The scintillation medium needs to be transparent to the wavelength of the produced light pulse so that the photons can exit the material. The time it takes for the luminescence to decay should be short so that fast radiation pulses can be detected. The medium should also have an index of refraction that is near that of glass so that the scintillator can be coupled to the detector head with little light reflected at the barrier between the medium and detector head. Scintillating materials do not simultaneously meet all of these requirements; a compromise between these properties must be established for each material and radiation being detected.

Scintillators are divided into two different categories, organic and inorganic. Inorganic scintillators usually have a higher light output and linearity, but depending on

the material, they tend to have a slow response time. Organic scintillators will usually output less light, but they have a faster response time compared to inorganic scintillators. The material being detected also influences what type of scintillator is good for a particular application. Inorganic scintillators have a higher density and are better for gamma-rays, while organic scintillators are better for betas and neutrons because of their hydrogen content.

Light can be emitted from a material by three different mechanisms: prompt fluorescence, phosphorescence, and delayed fluorescence. Prompt fluorescence is the desired type of emission. Prompt fluorescence is the emission of visible light when the material is excited by radiation energy. Undesired emissions in scintillators are phosphorescence and delayed fluorescence. Phosphorescence is the emission of a longer wavelength of light compared to fluorescence and takes longer to be emitted. Delayed fluorescence is an emission of light at the same wavelength as prompt fluorescence but takes longer to be emitted from the material. When scintillators are operated in pulse mode, the phosphorescence and delayed fluorescence are not a major factor because the signals they produce are usually low level and not detected. When using scintillators in a steady-state current mode, the phosphorescence and delayed fluorescence will start to contribute to the overall signal.

3.3.1 Organic Scintillators

The prompt fluorescence in organic scintillators occurs within the energy levels of a single molecule and is independent of the physical state of the molecule. This differs from inorganic scintillators which require a regular crystalline structure. Organic scintillators rely on organic molecules that have symmetrical properties, giving what is

called a π -electron structure. The π -electronic energy levels for a molecule are shown in Figure 3.2.

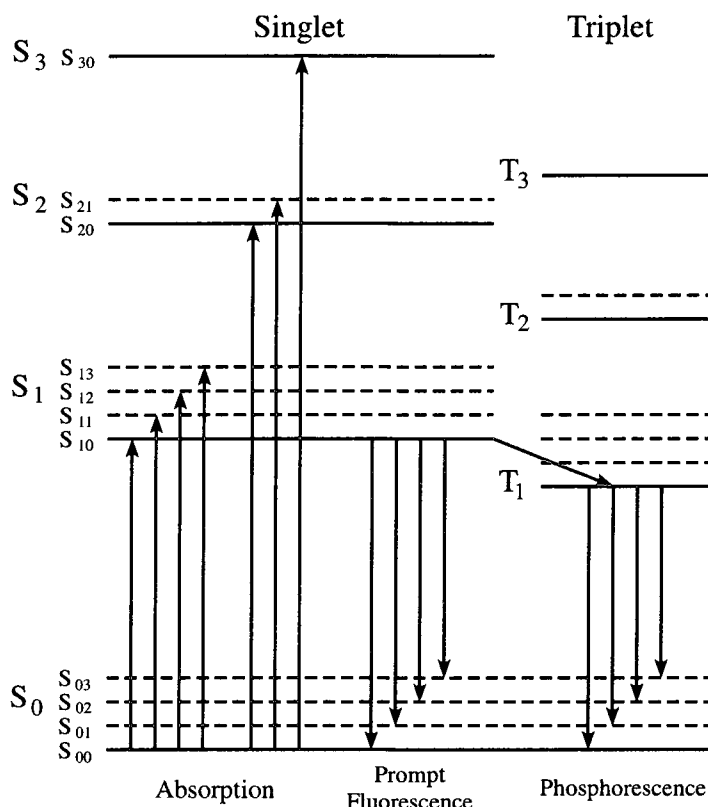


Figure 3.2 Configuration of organic scintillator electronic energy levels.

The energy of the radiation can be absorbed to excite an electron to any of the excited states shown in the figure. The energy states are divided into two types: singlet and triplet states. Electrons that de-excite from level S_1 to S_0 give off fluorescence and delayed fluorescence. Electrons excited to states higher than S_1 are de-excited to the S_1 electron state through internal conversion. The lifetime of triplet states are a lot longer than singlet state and result in phosphorescence. The intensity level of prompt fluorescence produced by radiation excitation is given in Equation 3.1.

$$I = I_0 e^{-t/\tau}, \quad (3.1)$$

where τ is the fluorescence decay time for the S_{10} level and t is the time following the excitation interaction. In organic scintillators the constant τ is typically in the nanosecond range, meaning that the scintillated light pulse is relatively fast.

When radiation interacts with the scintillating medium, only a small part of the energy is converted into fluorescence light; the remainder of the energy is lost through lattice vibrations or heat. The fraction of particle energy that is converted into light depends on the type of particle and the amount of energy present in the particle. This fraction that is converted is known as the scintillation efficiency of the material.

3.3.2 Inorganic Scintillators

Inorganic scintillators have a different way of creating scintillated light from radiation particles. For inorganic scintillators, scintillation is dependent on the energy states within the crystal lattice of the material. Crystals only have discrete bands of energy available for an electron to be found in. The absorption of radiation energy excites the electrons in the crystal from the valence band into the conduction band. When the electron then de-excites, the energy that is released is in the form of a photon. Usually the energy of the photon is too high to be within the visible range. To make the scintillator more efficient at releasing a photon in the visible range, impurities are added to the crystal. The impurities are called activators, and they create areas within the lattice that have a modified band structure. The modification in the band structure allows electrons to be found between the valence and conduction bands. The energy that is released from these areas in the crystal is less than the normal energy emission from photons falling from the conduction band and falls within the visible range of light.

CHAPTER FOUR

BORON LOADED SCINTILLATORS FOR DETECTION OF ALL FOUR TYPES OF RADIATION SPECIES

The prevention of nuclear terror was listed as one of the fourteen grand challenges for engineering in the 21st century by the National Academy of Engineering. One of the five major challenges listed for nuclear detection was the ability to detect nuclear material at a distance. While there are many types of radiation detectors that have been developed, these detectors are not practical for implementation into compact field detectors for one or more reasons: they are too expensive to mass produce, they lack the ability to be miniaturized into a portable detector, they have complicated designs that cannot be batch produced, or they cannot detect and discriminate all four types of radiation species.

My project attempts to design a turn-key micro-system that can be mass produced at a low cost. These sensors can then be implemented in large numbers into sea ports, airports, nation borders, and various commercial areas to provide real time radiation monitoring. Since the sensors will be cheap and easy to produce, they can be deployed in large numbers into a smart network configuration that can provide radiation detection and tracking of a radiation source [4].

The detector platform uses scintillators doped with boron nanoparticles to detect the presence of incoming radiation particles. The nanoparticles are a conversion mechanism to create fast electrons from the interaction between the radiation and nanoparticles. The created fast electrons scintillate, creating a characteristic light pulse which is able to exit the detecting medium since the diameters of the nanoparticles are smaller than the wavelength of light. The optical light that is produced in the radiation/scintillator reaction can be detected by both photodiodes and photomultiplier tubes, which convert the optical pulse into a measurable electrical signal [44].

The advantage of using a scintillating material for the detection of radiation is the ability to record the amount of energy the particle releases upon the interaction with the material. The use of boron doped scintillators allows for the detector to detect the presence of neutrons being released. If an external off-the-shelf PM tube is to be used, the overall package size and cost per detector would increase [47]. A PM tube would also require the use of a high voltage chip to scale up the voltage from a battery supply to the voltages needed to operate the PM tube; this would then reduce the battery lifetime of the sensor. There are some advantages to using a PM tube, such as good response time, lower background noise, and the production of its own internal gain compared to photodiodes [48]. Using an integrated photodiode allows for both the detector to be processed together with the CMOS circuitry and to be operated off of a lower voltage, increasing the battery lifetime of the sensor. Photodiodes also offer the advantage of a higher quantum efficiency, which can produce a better energy resolution. They are also not as fragile as a PM tubes. Photodiodes have the advantage of being good for use with timing applications [2]. Both types of detectors have their own advantages.

For fissionable materials, the two main types of radiation that must be detected are the gamma rays and neutrons. Gamma and neutron radiation have longer mean free paths than charged particle radiation, allowing for some standoff detection [49]. Both particles are more difficult to shield and to detect compared to charged particles. Since neutrons have a low probability to react with traditional semiconductor materials, a conversion medium with high neutron cross sections is needed [50]. Two common materials used as a conversion medium to detect neutrons are ^{10}B and ^6Li . The detector platform allows for the detection of all four types of radiation: alpha, beta, gamma/X-ray, and neutrons from a single chip. Since a fissionable weapon emits all four types of radiation species, it is essential for a field portable systems to be able detect and discriminate between each type [51,52]. Since biological radioactive isotopes also emit different types of radiation, it is essential that a detector be able to distinguish between a medical isotope and a nuclear weapon.

4.1 Device Design

The radiation detectors discussed in the chapter are created by doping glass and quartz substrates with boron nanoparticles to detect all four types of radiation species: alpha, beta, gamma/x-ray, and neutrons. The glass-based scintillator uses sintered glass frit doped with nanoparticles to create solid scintillator medium, while the quartz scintillator uses quartz wafers as a substrate with boron nanoparticles diffused into the wafer using a diffusion furnace. Both types of scintillators can be shaped to fit various detector windows.

The radiation impinging on the nanoparticles releases lower energy electrons which scintillate within the substrate creating a light pulse (Figure 4.1a). The light pulse

is then able to exit the detector interface, since the diameter of the nanoparticles is smaller than the scattering threshold of light. The exiting pulse is then guided to the PM tube detector head by waveguides embedded in the device (Figure 4.1b). The initial device design was created in a borosilicate glass substrate that was micro-sandblasted, but for a mass production device, it can be constructed from silicon wafers allowing for the device to be patterned on chip for a complete integrated package (Figure 4.1c).

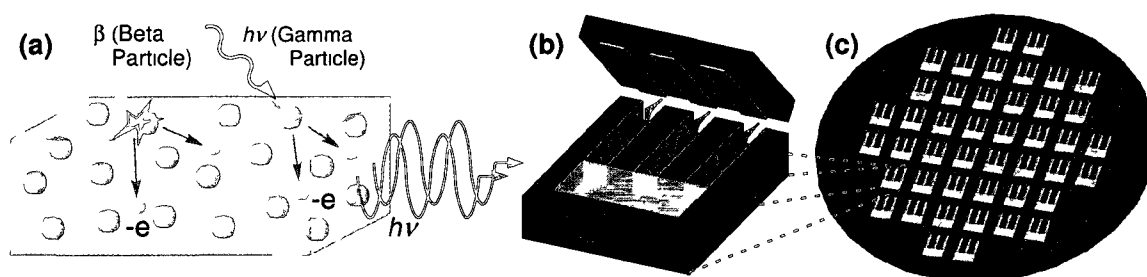


Figure 4.1 Glass and quartz substrates doped with boron nanoparticles converts radiation particles into optical pulses with varying heights which exit the scintillator (a). Optical pulses exiting the scintillator are directed away from the scintillating window by gold coated waveguides (b). The micro-device is patterned on-chip for a complete integrated radiation detection package (c).

4.2 Fabrication

The detector fabrication can be tailored to the application it is being applied to. The doped scintillators can be shaped into any form needed to cover the detecting window. They can be shaped by cutting from a larger piece or can be fabricated in a mold of the desired shaped. This section discusses the fabrication process for the initial prototype device that can be adapted to create other device shapes and sizes.

4.2.1 Device

The micro-device was made from a sandblasted glass substrate. A glass substrate was chosen because of the ease of processing and the ability to make many single devices

with various dimensions. To pattern the glass, a photo-sensitive polymer layer was deposited onto the substrate. Photolithography was used to define the areas of the substrate for the scintillator window and the waveguide channels. The exposed glass substrate was etched using micro sandblasting techniques creating the area for the scintillating window and multiple channels for the wave guides (Figure 4.2a,c). The size of the scintillating window on the device was $5 \times 4 \times 1$ mm with waveguides that were 1 mm wide and 1 mm deep. The micro sandblasting process uses a $<20 \mu\text{m}$ grit medium and has an etch rate of about 1 mm per minute. After etching the window and waveguide, gold was deposited into the channels and the bottom of the scintillating window (Figure 4.2b). The glass and quartz scintillators were then patterned into the device window. (Figure 4.2d). To enclose the waveguides, a glass cap was cut and the bottom side deposited with gold. The glass cap was then bonded to the device to enclose the waveguides, leaving the scintillating window exposed. The completed device was then covered with an opaque coating to cover the exposed glass outside and prevent stray light from reaching the scintillator and PM tube (Figure 4.3).

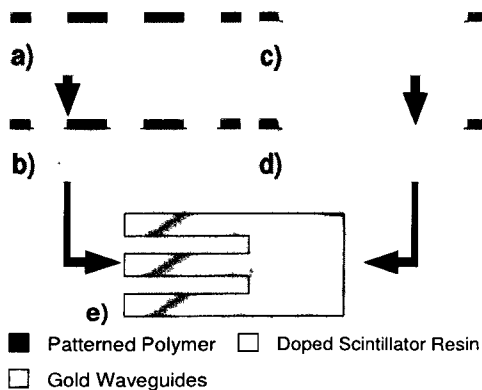


Figure 4.2 2-D process flow.

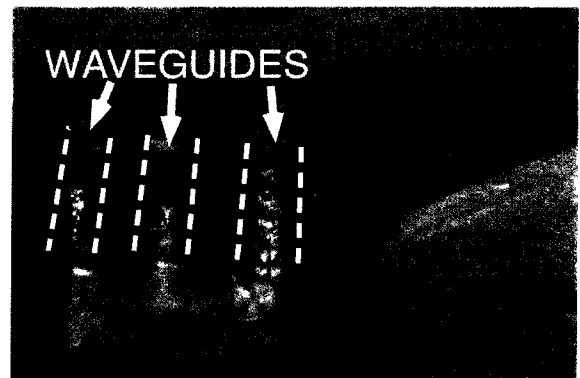


Figure 4.3 Photo of scintillating micro device with patterned scintillating quartz material inside of the etched cavity and gold coated waveguides (Cap not shown).

Only one type of geometry has been tested, but using nanoparticles embedded into glass and quartz substrates can easily be patterned into other geometries, allowing for various window sizes and shapes to be tailored to specific application sizes. Figure 4.4 shows a three dimensional drawing of the complete micro-device.

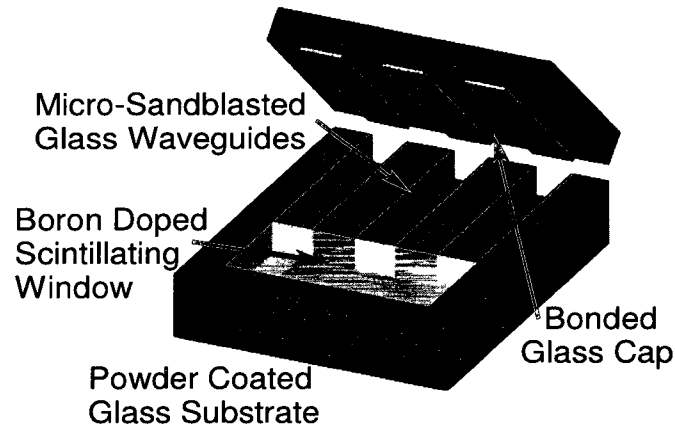


Figure 4.4 Micro-device drawing.

4.2.2. Scintillators

The glass frit for making the glass based scintillator was purchased from Bullseye Glass Company in a fine powder form with a crystal clear coloring. The boron nanoparticles were mixed with glass frit based on the percentage desired by weight. The formula used to determine the amount of nanoparticles is given in Equation 4.1.

$$\text{Loading percentage} = \frac{m_n}{m_n + m_s}, \quad (4.1)$$

where m_n is the mass of the nanoparticles and m_s is the mass of the substrate material. By solving the equation for m_n , the desired mass of the nanoparticles can be calculated. After the frit and the nanoparticles are mixed together, the mixture is placed in a ceramic holder for sintering. The mixture was heated in the furnace to 1500 °F to fuse the glass particles together and held at this temperature for 30 minutes. The temperature was then

dropped slowly to 800 °F over a 3 hour period to anneal the glass. After annealing, the furnace was dropped back down to room temperature.

The quartz scintillator was made using a quartz wafer for the substrate and diffusing the boron nanoparticles into the wafer. The quartz wafers were purchased from Hoffman Materials, Inc. and cut to size using a glass cutting saw. The doping percentage calculations for the amount of boron nanoparticles were determined using Equation 4.1. Since each substrate piece is not cut exactly to the same size, the quartz/boron weight ratios are recalculated for each piece. Once each piece is measured, it is placed in the furnace on a ceramic base. The boron was defused into the quartz by raising the furnace to 1500 °F at a rate of 200 °F/hr and held for 8 hours at the maximum temperature. Then the furnace was cooled to 1000 °F at a rate of 100 °F/hr. Upon reaching 1000 °F the cooling rate was then changed to 300 °F/hr until reaching room temperature. This heating cycle was determined from trial and error until the boron successfully defused into the quartz without the sample splitting or cracking into multiple pieces.

4.3 Testing

The device was tested using two different testing setups. Initial testing was performed using an oscilloscope to view the pulses that were being produced from the PM tube. The second test setup removed the oscilloscope and used a shaping preamplifier and a multichannel analyzer for more detailed analysis of the incoming pulses.

The reaction between the radiation particles and the scintillating medium will produce light particles that are typically in the visible light range. Since the light particles that need to be detected are in the visible range, there needs to be a way to

isolate the created light from background light. Large amounts of background light would also overwork the PM tube, shortening its lifespan. To shield the PM tube from the background light it, a light tight box was used. The box is constructed out of half inch plywood panels. The box also had an aluminum connector panel to allow for power to be delivered to the PM tube and the signals from the PM tube to be sent out to the equipment. The aluminum panel was attached to a cutout on one side of the box. Once complete, all the corners and edges of the box were caulked to prevent any stray light from entering the box. The box was tested using a PM tube with no radiation source or scintillator. Any signal from the PM tube would indicate that the box is not light tight, allowing background noise. After multiple tests and additional caulking and taping, a light tight box produced no background noise in the PM tube.

The next piece of equipment needed was a DC high voltage supply to power the PM tube. The high voltage supply used was from Stanford Research Systems Inc., and the model used was PS325. The high voltage supply is capable of supplying a maximum voltage of 25000 VDC with a maximum power output of 25 watts. The PM tube was operated at a voltage of 1000 VDC. The Hamamatsu PM tube used draws a current of about 0.27 mA when supplied a voltage of 1000 VDC.

The last piece of equipment used to the initial scintillator testing was an oscilloscope. The oscilloscope was used to visually see the number of pulses that were being created by each type of scintillator/radiation species combination. The scope was also used to determine the pulse amplitudes that were being created for each radiation species.

Once the scintillators were confirmed to interact with different radiation species, the oscilloscope was replaced with other test equipment. The oscilloscope was replaced with a pulse shaping amplifier and a multichannel analyzer. The pulse shaping amplifier and multichannel analyzer were purchased from ORTEC. The ORTEC equipment consists of a NIM bin to supplies ± 24 VDC and ± 12 VDC to individual detection components that slide into the NIM bin. The components in the NIM bin were a multichannel analyzer which requires ± 6 VDC supplies, a power reducer to provide the ± 6 VDC to the multichannel analyzer, and a pulse shaping amplifier. The pulse shaping amplifier shapes the incoming pulse into a Gaussian shape and can also amplify the signal with a gain of 1 to 40 using either inverting or non-inverting amplification. The multichannel analyzer is connected to the computer using via usb cable. The software used for analysis was provided by ORTEC with the equipment. The software divides up the energy spectrum into channels each with a range of 5 mV. As radiation particles are detected, the software counts the number of particles that occur within each channel range. This provides both the total number of particles detected over all ranges and well as the number of particles within each energy range.

4.3.1 Testing Setup

The testing setup for recording radiation energies using the multichannel analyzer consisted of the scintillator, PM tube, the light impenetrable box, pulse shaping amplifier and the high voltage supply. The PM tube was powered with the high voltage DC power supply. Five different radiation sources were used with the two scintillators to test how well the scintillator detects each type of radiation species. For alpha detection, the source used was ^{241}Am , which releases alpha particles with an average energy of 5.6 MeV. For

beta detection testing, a ^{90}Sr beta source was used with a dose rate of 3.2 $\mu\text{rem/hr}$ (micro-rem per hour). ^{90}Sr emits beta particles that have an average energy of 546 keV. For gamma testing, a ^{60}Co gamma source was used. ^{60}Co emits both gammas and beta particles; the gamma particles for ^{60}Co are emitted with energies of 1.17 MeV and 1.33 MeV. The beta particles that are emitted from the ^{60}Co source have a maximum energy of 315 keV. The ^{60}Co lab source used for testing has a dose rate of 10 $\mu\text{R/hr}$ (micro-roentgen per hour). For testing the scintillator for the ability to do source differentiation, a ^{137}Cs source with a dose rate of 10 $\mu\text{R/hr}$ was used along with the ^{60}Co source. The ^{137}Cs source emits either a beta particle and gamma ray when it decays or a single higher energy beta particle. When the single beta particle is emitted, it has an energy of 1.17 MeV, with this type of decay occurring about five percent of the time. When both the beta particle and gamma ray are emitted, the energies are 510 keV for the beta particle and 662 keV for the gamma ray. For neutron detection testing, a neutron source was constructed in the lab. The neutron source was fabricated using the ^{241}Am alpha source and beryllium foil. The alpha particle interaction with beryllium foil results in a neutron being released if the beryllium foil thickness is larger than the absorbing range of the alpha particle in beryllium. Only about 1 out of 10,000 alpha particles will interact with the nucleus of a beryllium atom resulting in the release of a neutron. The rest of the alpha particles are stopped by the foil and no nucleus interaction occurs. The alpha particle/Be reaction is given in Equation 4.2.



this interaction produces about 70 neutrons for every 1,000,000 alpha particles that enter the beryllium foil.

The testing configuration consisted of the radiation source, scintillator, and PM tube being contained within the light impenetrable box. The Stanford high voltage supply provided power to the PM tube and the signal for the PM tube was fed into oscilloscope input. For later testing with the multichannel analyzer, the output of the PM tube was fed into the pulse shaping amplifier and then into the analyzer. The initial testing of the glass and quartz scintillators was for particle count rates compared to the distance between the source and the scintillator. Later testing consisted of testing for ability to use the scintillator to differentiate between two types of source with different decay schemes.

4.4 Results and Discussion

4.4.1 Beta Particles

The beta particles passing through the scintillator react with the orbital electrons of the absorber's atoms through columbic forces. When comparing the beta particle interaction to the interaction of the larger alpha particles within the medium, the beta particles lose their energy at a much lower rate because of their smaller size. Unlike alpha particles, beta particles do not travel a linear path through the medium. Since the size of beta particles is similar to the size of the orbital electrons, they can lose more energy per encounter and have path deviations within the material.

Beta radiation test were conducted using a ^{90}Sr source. The ^{90}Sr source was placed at different distances away from the glass scintillator to test the relation of counts per minute versus the distance. The size of the source limits the count rate versus distance that can be tested with the detector. Figure 4.5 shows the count rate versus distance for the glass scintillator doped with boron nanoparticles.

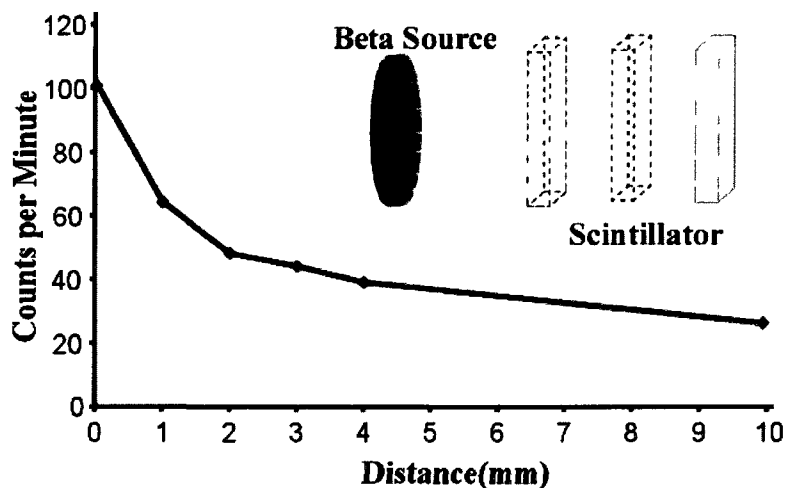


Figure 4.5 Beta counts verse distance for the glass scintillator.

The count rate per minute of the beta particles decreases as the distance is increased between the scintillating window and the source. The count rate of the beta particles rapidly decreases at first because the low energy beta particles are absorbed by the air gap between the detector and the source. As the distance is increased the attenuation becomes more exponential. Since the path of the beta particle is not linear and changes direction with each interaction, eventually the particle will not have enough energy to exit the scintillator and the count rate will drop to zero.

Beta testing was also done using quartz substrates doped with boron nanoparticles. Figure 4.6 shows the count rate versus the distance of the quartz scintillator compared to the glass scintillator.

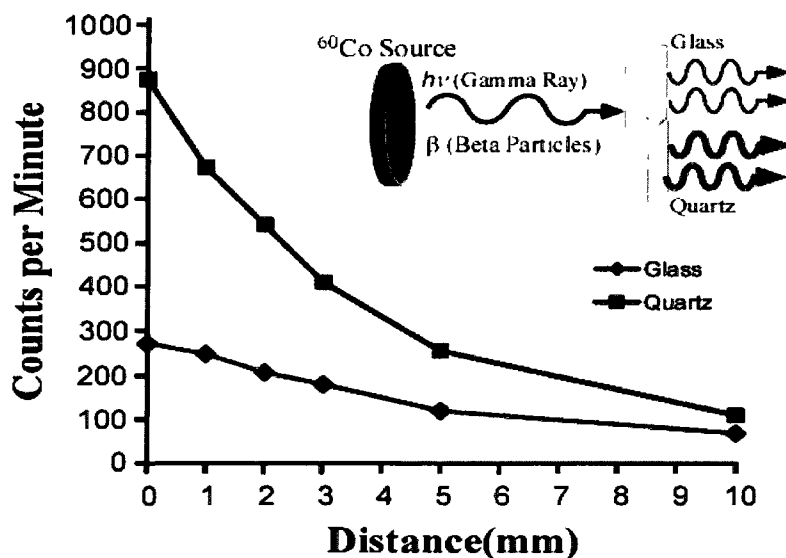


Figure 4.6 Quartz scintillator compared to the glass scintillator for beta detection.

The quartz scintillator shows a better detection rate for beta particles when compared to the glass; this shows the boron doped quartz has better stopping power than glass for beta particles. The stopping power of a material is described by how well a material absorbs incoming radiation; the better the stopping power, the more likely incoming radiation will interact with the atoms in the absorbing material. The quartz also shows a better count rate over a distance showing that quartz can detect additional lower energy particles.

Testing was also done to compare the beta absorption efficiency of the two scintillators. The testing showed, as expected, that increasing the thickness of the material improves particle absorption. Both scintillators were tested with three different substrate thicknesses. A base line test was done with no material between the source and detector to test how many particles reached the detector. The glass and quartz was then placed between the source and detector to determine how many particles are being

absorbed in the material and how many pass completely through. Figure 4.7 shows the beta absorption efficiency of the two scintillators.

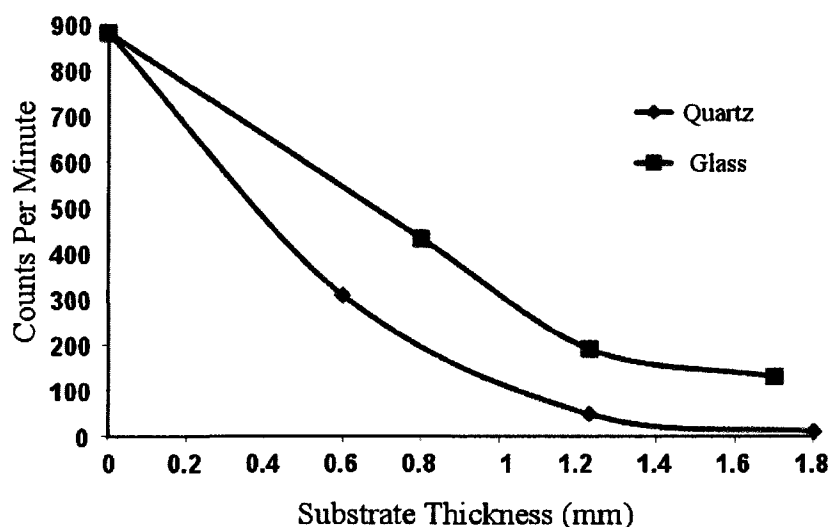


Figure 4.7 Glass and quartz absorption of beta particles as substrate thickness is increased.

Both scintillators show a rapid increase in beta particle absorption as thickness is increased. The quartz shows better absorption efficiency than the glass, which is consistent with the results from the detection of counts per minute of the previous experiment.

4.4.2 Gamma Rays

Gamma ray detection is essential for fissionable material identification because both neutrons and gammas emitted from these materials are hard to shield. Gamma ray detection testing was done using a ^{60}Co source; this source emits both gamma rays and beta particles.

Gamma detection occurs when the radiation particles interact with the ^{10}B nanoparticles within the scintillator. The gamma ray interaction with the nanoparticles leads to the photon energy being partially or completely transferred to electron energy,

which is important when trying to detect gamma rays. After the energy transfer occurs, the photon either will disappear or will be scattered, changing its path completely. The energy transfer from the photon results in a recoil electron that is then scintillated inside of the medium creating an optical pulse [53,54]. These secondary electrons are emitted through pair production, Compton scattering, and photoelectric absorption [2]. Photoelectric absorption has a high probability of occurrence with lower energy gamma rays, while higher energy gamma rays will liberate electrons through Compton scattering. For photon radiation energies that are about twice the rest mass of an electron, the probability of pair production occurring increases [46].

The gamma radiation detection was also tested as a function of distance from the source for both types of scintillators. Figure 4.8 shows the count rates versus distance for both scintillators in the presence of a gamma source.

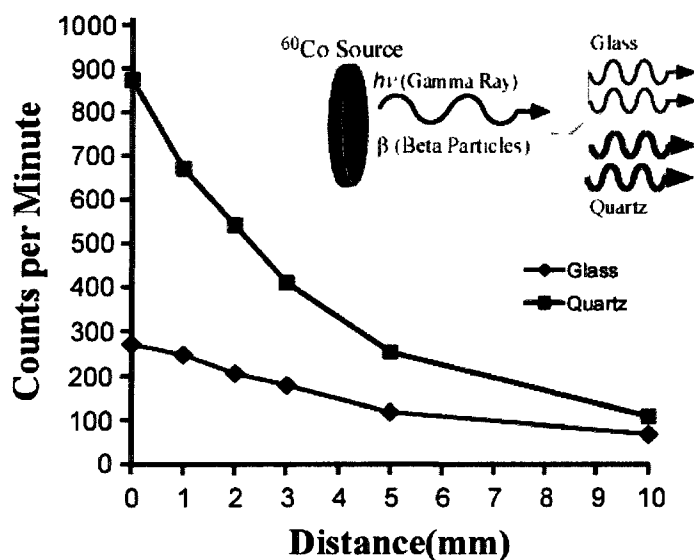


Figure 4.8 Testing the scintillator detectors with a gamma ray source for a function of counts per minute over varying distances.

Gamma rays are not attenuated in air as easily when compared to the beta particles, resulting in a more linear decrease in particle detection over a distance. The quartz scintillator again shows better detection efficiency than the glass scintillator. The energy spectrum for each type of scintillator was also looked at using the ^{60}Co source at a distance of 0 mm. By looking at the energy spectrum the scintillators can be compared by more than just a particle detection rate; the spectrum gives both a count rate over a time period and the ability to see the energies of the particles being detected. Figure 4.9 shows the spectrum of both the glass and quartz scintillator in the presence of the ^{60}Co source. We can see that the quartz is better at detecting both the lower and higher energy particles when compared to the glass.

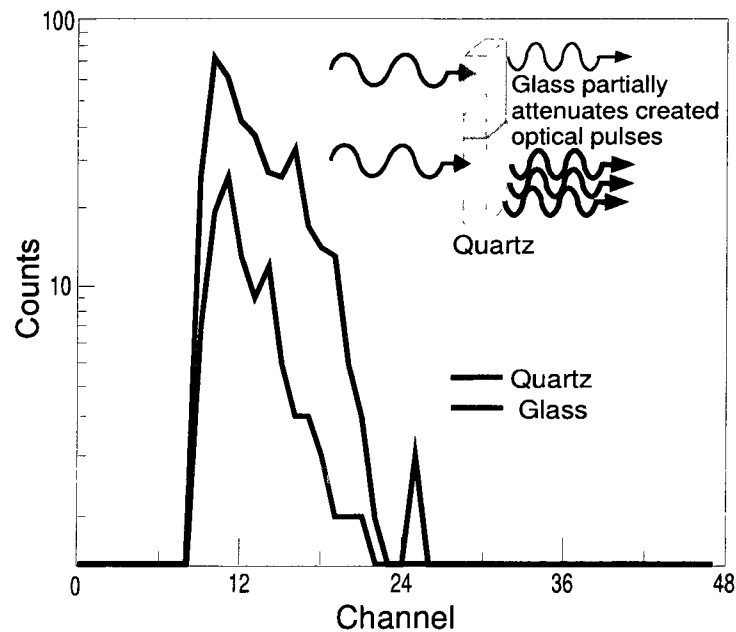


Figure 4.9 Glass and quartz have similar energy spectra allowing for glass or quartz to be used as the detecting medium.

The gamma ray absorption efficiency of both scintillators was also tested. To experiment with the absorption of only gammas, a thin sheet of lead was placed in front

of the ^{60}Co source to block the emitted beta particles. Figure 4.10 shows the absorption efficiency of the glass and quartz scintillators.

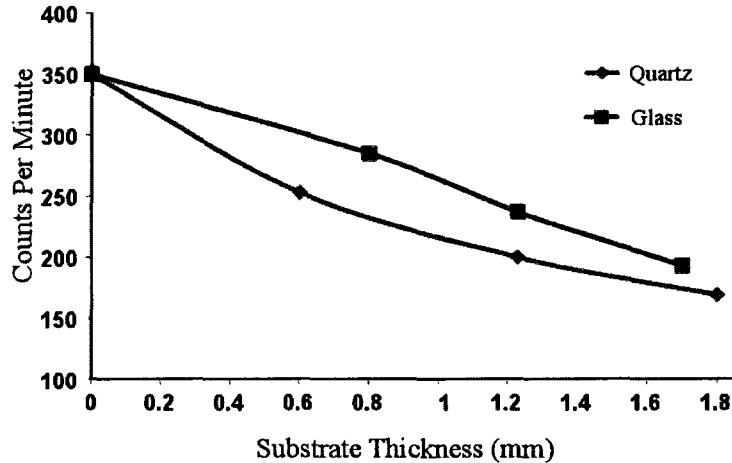


Figure 4.10 Glass and quartz absorption of gamma rays as substrate thickness is increased.

The absorption of gamma rays for both materials is more linear when compared to the beta absorption in Figure 4.7. This is due to the fact that gamma rays have a larger mean free path than the betas, resulting in fewer interactions between the gamma rays and the quartz and glass substrates. Again the quartz shows to have better radiation particle absorption when compared to the glass.

4.4.3 Alpha Particles and Neutrons

Alpha particles primarily interact with matter through coulomb forces between the positive charge of the alpha particle and the negative charge of the orbital electrons within an absorbing medium. As the alpha particle enters the scintillator, it interacts with many electrons simultaneously. If the amount of energy transferred from the alpha particle to the electron is enough to strip the electron from the particle, the electron scintillates in the medium. The alphas are heavy particles which are much larger than

orbital electrons. Since alphas are much larger than the nearby orbital electrons, they have a linear path through the scintillator because the pull from the orbital electrons is from all directions. The particle will continue to travel through the scintillator until it dissipates all of its energy.

Neutron radiation is difficult to detect due to the limited reactions neutrons have with other particles. To detect neutrons, the uncharged particle is converted into a charged particle. Using a scintillator doped with ^{10}B nanoparticles allows for the conversion of these neutral charges into a detectable charged particle. When neutrons do interact with an absorbing atom, it is with the atoms nucleus, where either the neutron will be absorbed and secondary radiation species will be emitted or the direction and the energy of the neutron will be changed dramatically. Neutrons entering the detector medium interact with the boron nanoparticles releasing an alpha particle. A secondary reaction then occurs between the released alpha particle and the substrate.

When neutrons enter an absorbing medium, they do not always interact with the atoms of the absorber; some pass completely through with no interaction at all. The neutron cross section of a material is a term used to describe the probability of neutrons interacting with the absorber. This cross section is dependent on the energy and amount of neutrons entering the absorber, as well as the quantity and type of nuclei in the absorber. The better the neutron cross section of an absorber, the higher the probability of interactions with neutrons passing into the medium. The benefit of using ^{10}B is it has a high thermal neutron cross section (3,840 barns) allowing for the maximum number of impinging neutrons to be absorbed, converted, and detected.

Figure 4.11 shows the detection of all four types of radiation species using the boron doped scintillator. The pulse heights for the detected particles in the figure are: alpha 35 mV, beta 60 mV, gamma 90 mV, and neutron 38 mV.

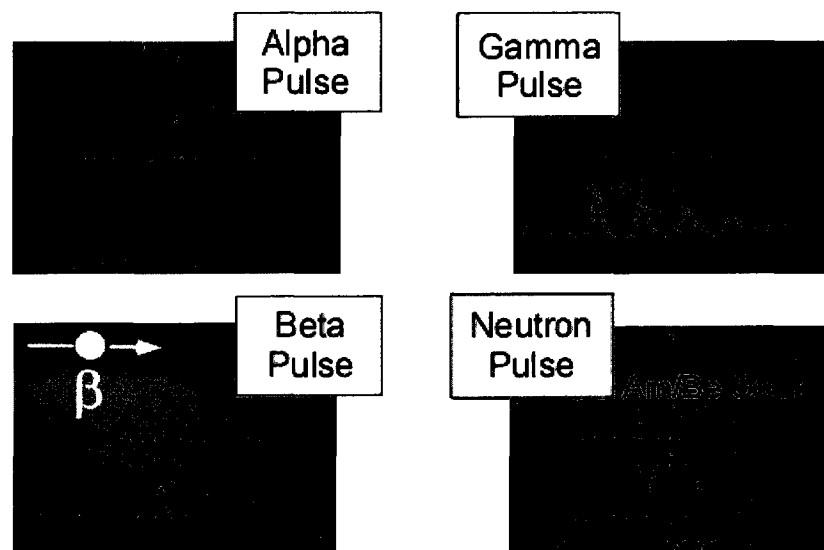


Figure 4.11 Boron doped scintillator has the ability to detect all four radiation species. Scaling for the alpha, beta, and gamma pulse are 50 mV y-axis divisions and scaling for the neutron pulse is 25 mV y-axis divisions.

We can see that the alpha and neutron pulses are similar in energy. This comes from interaction between the boron nanoparticles and neutron producing a secondary radiation species of an alpha particle which is then scintillated. We can also see from the figure that all the pulses, while different in amplitude, look similar; and since not all particles of a particular type have the same energy, there can be overlap in pulse heights for different species. This can make determining the kind of radiation difficult; the solution to this problem is to not look at individual pulse heights but to look at pulse height sets. This is later discussed in the radiation source differentiation section.

4.4.4 More Quartz Testing

The quartz scintillator doped with boron nanoparticles was shown to be a better detecting medium, so further testing was done using quartz. The amount of nanoparticles in the scintillator affects the detection efficiency; the more particles inside the substrate, the better the chance of particle interaction. There is a drawback to increasing the doping percentage of the scintillator; as the nanoparticle content is increased, the optical qualities of the scintillator become degraded. Although it increases the detection efficiency, it makes it more difficult for the created light to exit the scintillator. Figure 4.12 shows the count rate of multiple quartz scintillators each doped with a different percentage of boron concentrations based on weight.

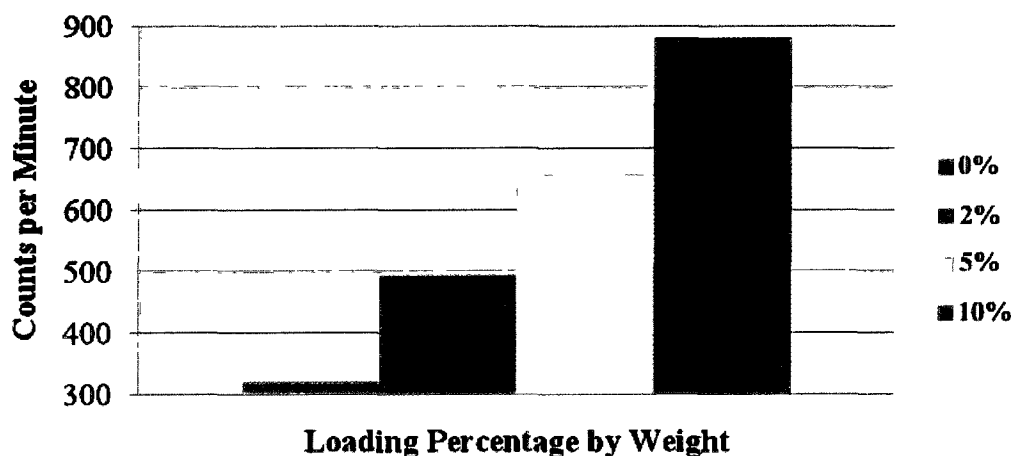


Figure 4.12 Quartz scintillator was doped with various doping percentage based on weight.

The results from the graph show that as more boron is doped into the quartz substrate, the detection efficiency becomes higher. To further understand what is occurring as the doping percentage is increased, the energy spectrum of the detectors were compared. Figure 4.13 shows the energy spectrum for the 2%, 5%, and 10% doping concentrations.

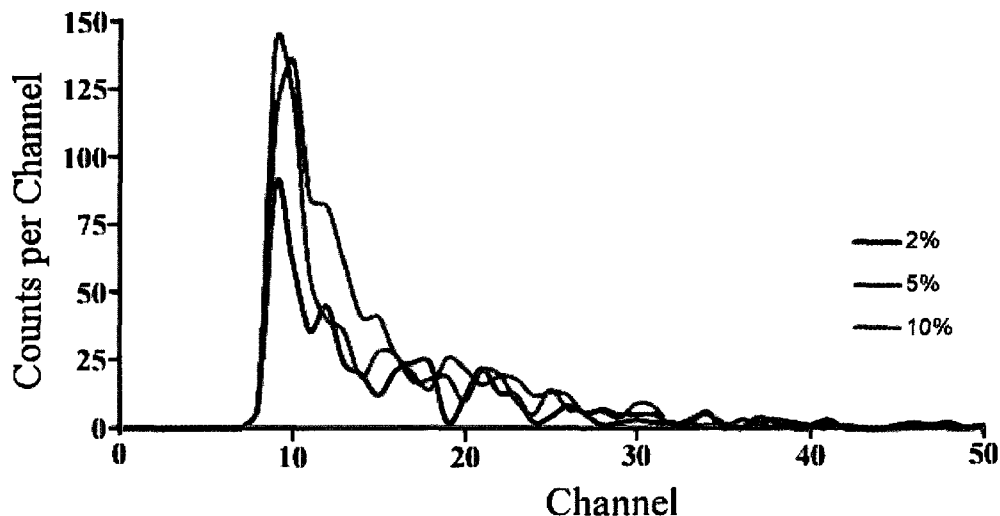


Figure 4.13 Energy spectrum of the quartz scintillator doped with 2%, 5% and 10% boron by weight.

Comparing the energy spectrums of the three doping percentages shows that both the 5% and 10% doping levels have about the same detection efficiency for lower energy particles. The scintillator with a 10% doping level shows a higher stopping power than the 5% doping when interacting with higher energy particles. This results in the higher doping percentage to have a better overall detection efficiency.

4.4.5 Radiation Source Differentiation

To effectively determine the type of threat a package emitting radiation poses, there needs to be a way to determine what kind of radiation is being emitted, not just that there is radiation present. Each type of radiological isotope has its own type of radiation decay scheme. Figure 4.14 shows the radiological decay scheme for two types of radiation sources.

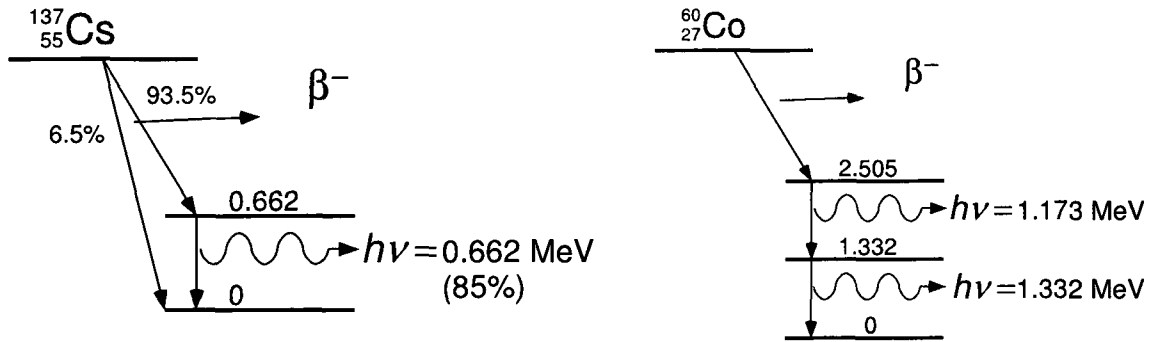


Figure 4.14 Decay scheme for cesium-137 and cobalt-60 radiation sources.

Knowing that each type of source has its own decay scheme, we can now look for radiation particles detected over a period of time from one source to determine the type of source. Since the scintillator is capable of detecting all types of radiation species, it can be used for sources that emit more than one type of radiation. By calibrating the detector with different sources, the difference between each type of source can be recorded and compared to radiation detected in the field. Figure 4.15 shows the difference between detecting ^{137}Cs and ^{60}Co using the boron doped quartz scintillator.

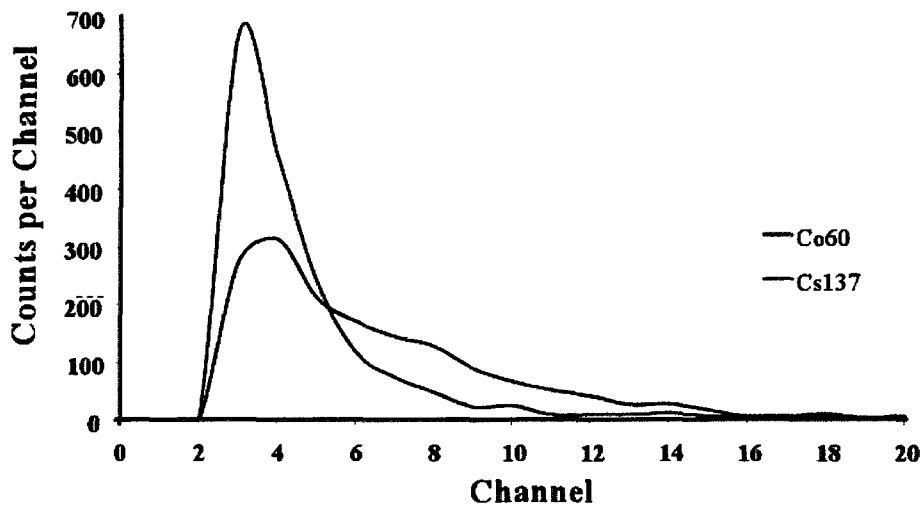


Figure 4.15 Source differentiation between ^{137}Cs and ^{60}Co .

From the figure we can see that when the two sources are compared, we can use the energy of the emitted particles to tell the difference between the two sources. When the scintillator is exposed to both sources for the same period of time the ^{137}Cs emits more lower energy particles than the ^{60}Co . This type of result is expected when looking at the decay schemes of the two sources. ^{137}Cs emits one beta and one lower energy gamma ray, while the ^{60}Co source emits a beta particle and two higher energy gamma rays. For a field ready detector, there is a need to set up a complete database of sources that can be encountered to effectively discriminate between types of radiological sources.

CHAPTER FIVE

CREATING A DETECTING PACKAGE: ADDING CIRCUITRY

Once a sensor is designed and prototyped, there is a need to design the next part in the sensing package. After a sensor can detect the input signal, the next step is to create the circuitry that can take this input signal and turn it into something that is useful and can be recorded and analyzed. This chapter discusses the design of the signal processing circuitry that is used with the scintillators and PM tube sensors discussed in the previous chapter.

The goal of the detecting circuitry is to linearly amplify the signal that is generated by the PM tube. The circuitry needs to amplify the total charge of the radiation particle, not just the peak current output produced from PM tube. After the total charge is amplified, the circuitry then needs a system that can amplify and record the data that is being received. The last step is using that data to determine the type of radiation that is being detected. The system needs to be field portable and have multiple methods of displaying the information, dependant on the application. If the sensors are being used in a wireless network, then the data from each sensor just needs to be stored in the device and then transmitted to a central location that can interpret the data. If the sensor is used in a handheld device, then the user needs to be able to read and interpret the data in the field.

5.1 Circuit Design

The first iteration of the design was created in the circuit simulator program LT Spice IV and prototyped using discrete circuit components on a printed circuit board. The signal from the PM tube is fed into a charge sensitive preamplifier. The preamplifier integrates the current that is received from the PM tube to obtain the total charge of the particle that is being detected. The output of the amplifier is a voltage signal representing the charge of the particle; from this point the signal can be shaped and amplified. The output signal then passes through a high pass filter to remove any DC offset that is produced by the dark anode current of the PM tube. The next stage is a set of filters to shape and amplify the voltage signal. At this point, the signal is split and used for both recording the particle energy and triggering the recording device. The first signal is fed into a peak detection circuit; this circuit is used to hold the peak of the shaped wave form until it can be recorded. The second signal is used as a trigger to start recording the peak. A comparator is used for this task; the comparator is set at a trigger voltage that is above the noise level and will go into a high state once the leading edge of a radiation pulse reaches the trigger voltage. This high state will signal a recording device to start recording the pulse height of the peak detecting circuit. When the pulses trailing edge drops below the trigger level, the device will stop recording and reset the peak detector. A block diagram of the circuit components is shown in Figure 5.1.

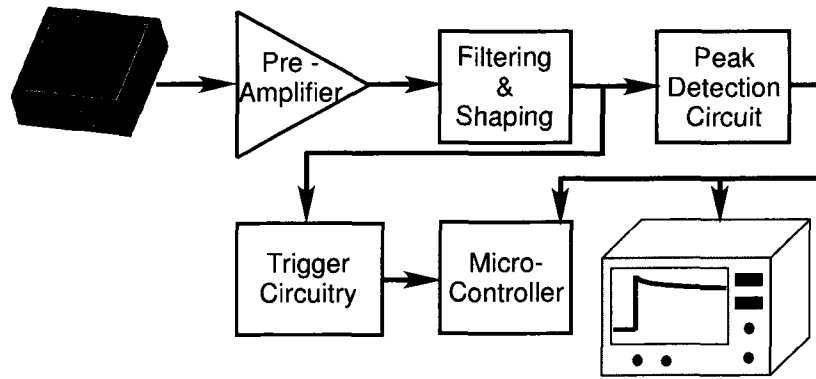


Figure 5.1 Block diagram of circuit components.

5.1.1 Charge Sensitive Preamplifier

The charge sensitive preamplifier is designed using a single operational amplifier with a capacitor and resistor in the feedback loop of the amplifier. When the PM tube is detecting a signal, the electrons are pulled to the detectors anode. The convention is to say current flows in the opposite direction of the movement of electrons; therefore, in the case of a PM output, the current flows into the detector. Because of this, the signal from the PM tube that is seen is a negative pulse. The negative pulse generated from the PM tube is helpful because the preamplifier configuration has an inverting property that will give a negative input a positive output voltage. A schematic diagram of the charge sensitive preamplifier is shown in Figure 5.2.

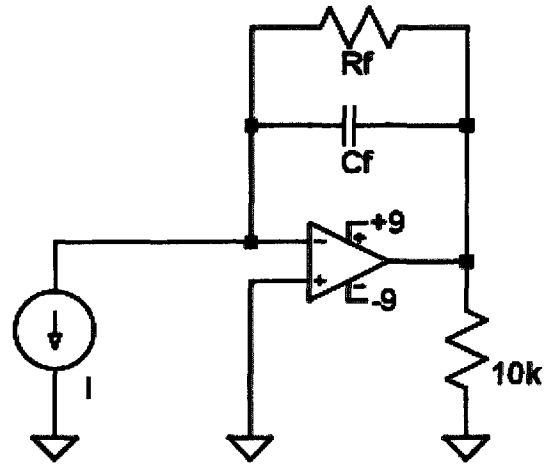


Figure 5.2 Schematic diagram of the simulated charge-sensitive preamplifier.

Having a capacitor (C_f) in the feedback loop allows the amplifier to integrate the total charge that is deposited onto the capacitor which is then represented by an output voltage [55]. The equation for the amplitude of the output voltage is given by Equation 5.1.

$$V_{out} = -\frac{Q}{C_f}, \text{ where } Q = \int_0^t i(x)_{in} dx, \quad (5.1)$$

The feedback resistor (R_f) that is connected in parallel with the feedback capacitor is used to discharge the accumulated current on the capacitor. This gives the output voltage pulse an exponential decay that is governed by the time constant, τ , which is created between the capacitor and resistor. The equation for the total output voltage waveform is then given by Equation 5.2.

$$V_{out} = -\frac{Q}{C_f} e^{-\frac{t}{\tau}}, \text{ where } \tau = R_f C_f, \quad (5.2)$$

The preamplifier was simulated in LT Spice to determine what types of values are needed to get a usable output waveform that can later be filtered and shaped for recording. The output form of a PM tube related to the electrons flowing to the anode

can be approximated by a Gaussian shape [45]. The preamplifier was tested using a single current pulse. To approximate a simple Gaussian shape, the current source was set up to have a rise and fall time as well as a time interval at peak current. Various input currents, each with a different peak current, were tested, each input using the same rise and fall time of 5 ns (Figure 5.3). A second set of input signals were also tested to show how the amplifier amplifies the total charge, not just the peak current; for this the peak current was held constant, but the on time was varied (Figure 5.4).

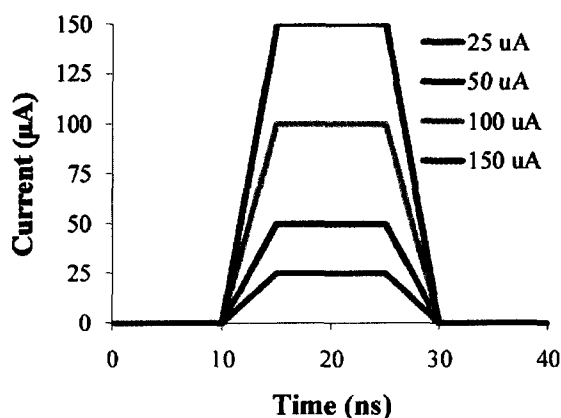


Figure 5.3 Varied input test currents with uniform pulse width.

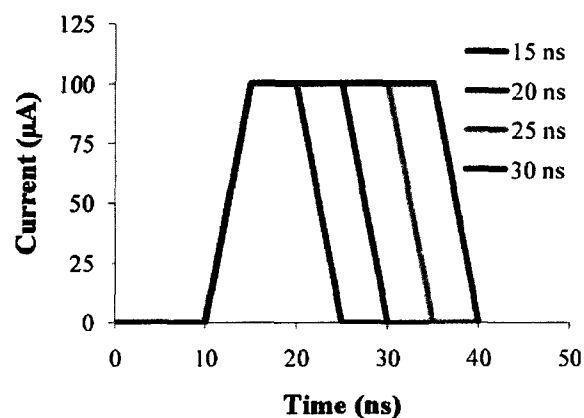


Figure 5.4 Uniform input test current with varied pulse width.

Figure 5.5 shows the output voltage of the charge sensitive preamplifier using the input currents shown in Figure 5.3. The preamplifier was tested with a feedback capacitor of 5 pF and two different feedback resistors, one with a value of 50 kilo-ohms and other a value of 100 kilo-ohms. We can see that the output voltage peaks follow a linear path, showing that this configuration will give us linear amplification, which will make discriminating between radiation particles of varying energy easier. We can also see that the feedback resistor also slightly affects the output voltage; in the ideal case, the resistor would not affect the output peak and only affect the discharging time constant. This side

effect can be useful if the requirement for the discharging time constant is not strict because the higher the resistor value, the easier it is to discriminate between different pulse heights, giving the circuit a higher resolution. Figure 5.6 proves the preamplifier is actually amplifying the total current from the current source not just the peak. The input current source is shown in Figure 5.4. By varying the feedback capacitor, we can also see how the capacitor affects the resolution of the circuit; as the capacitance is increased, the resolution between various current sources is reduced.

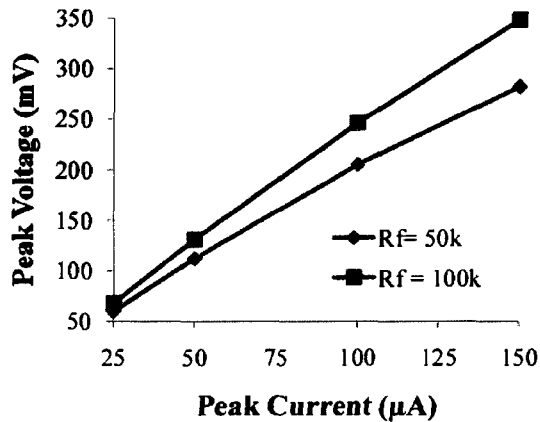


Figure 5.5 Peak output voltage with feedback capacitor of 5pF.

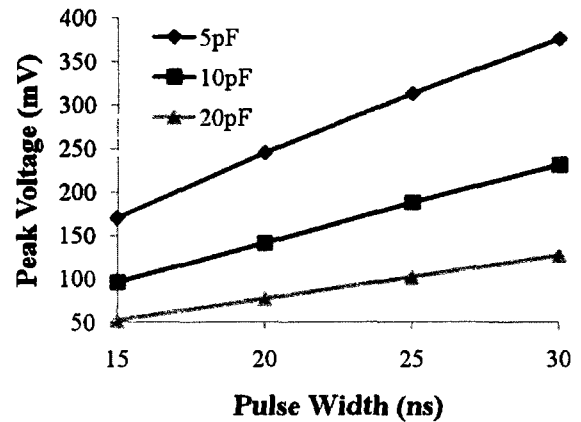


Figure 5.6 Peak output voltage with varying pulse widths.

Figure 5.7 shows the output of the preamplifier with a time constant of 500 ns using a 5 pF feedback capacitor and a 100 kilo-ohm feedback resistor. Once a time constant is picked for the test circuit, current pulses can then be used to determine the approximate pulse heights versus the total charge deposited from the PM tube. Figure 5.8 is another example of how the feedback capacitor affects the resolution of circuit. The feedback resistor was held constant to show how changing the resolution between peaks will also affect the time constant; this fact becomes important later when the circuit will be designed into an integrated circuit. When the capacitor and resistor must be put on

chip, the physical size of the components then become a factor, since the capacitors take up the most physical space on the circuit die.

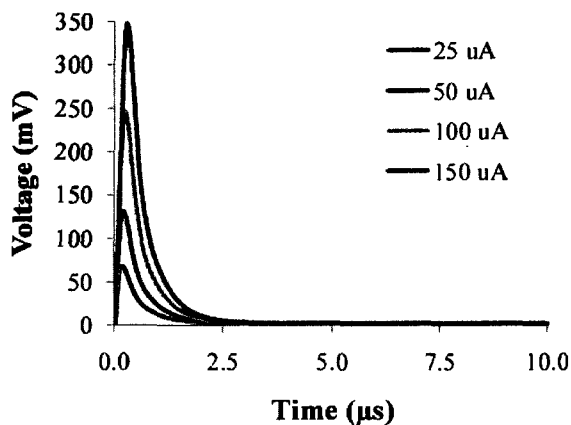


Figure 5.7 Preamplifier output with 5pF capacitor and 100k resistor.

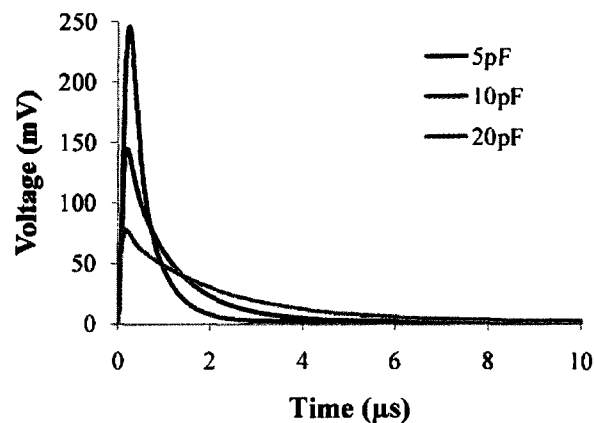


Figure 5.8 Preamplifier output with varying feedback capacitors and 100k resistor.

5.1.2 Filtering and Shaping

After designing a preamplifier and understanding what kind of limits it imposes on the type of output voltage pulse that can be created from a PM tube current input, the next step is to use a set of filters to adjust the output voltage signal into an output wave shape and amplitude that can be used for recording purposes. Since the initial design is constructed with discrete components using off-the-shelf amplifiers. Dual supply operational amplifiers that use large supply voltages, approximately 9 volts, allow for large gain amplification to separate the pulse heights. For my design, I wanted to make sure that all of the amplification is as linear as possible so that the design will easily scale and a variety of supply voltages can be used without large modifications.

The overall waveform that I want to design is a Gaussian type shape that can be used for both recording a ratio of the peak voltage that is received from the charge sensitive preamplifier and using the leading and falling edges of the Gaussian shape to

trigger the comparator. The best method for creating a filter is to use Laplace transforms and transfer functions to calculate a filter that will give the desired output waveform. The input waveform from the preamplifier can be approximated by the function given in Equation 5.3.

$$f(t) = Ae^{-\alpha t}, \quad (5.3)$$

where A is the amplitude of the input and α is the inverse of the time constant τ which is obtained from the values of your feedback resistor and capacitor of the preamplifier. For a time constant of 2 μs , α is equal to 500,000. The desired output of the filter is a Gaussian waveform described in Equation 5.4.

$$g(t) = Ae^{-\frac{(t-b)^2}{2c^2}}, \quad (5.4)$$

where A is the amplitude of the curve, b is the location of the peak and c is half the desired width of the curve. The problem with using a true Gaussian function with Laplace transforms is that the transform of the function includes an error function. The error function complicates the process of finding a realizable transfer function. To avoid this, an approximation of the Gaussian curve can be substituted. The function used in the place of the Gaussian is given in Equation 5.5.

$$y(t) = A(e^{-\beta t} - e^{-\gamma t}), \quad (5.5)$$

where A is the amplitude and β and γ are decay constants of the exponential functions. In the case of a Gaussian with a peak at 3 μs and a pulse width of 6 μs the values of β and γ are 300,000 and 425,000 respectively with amplitude, A , of 7.8. The three waveforms are shown in Figure 5.9.

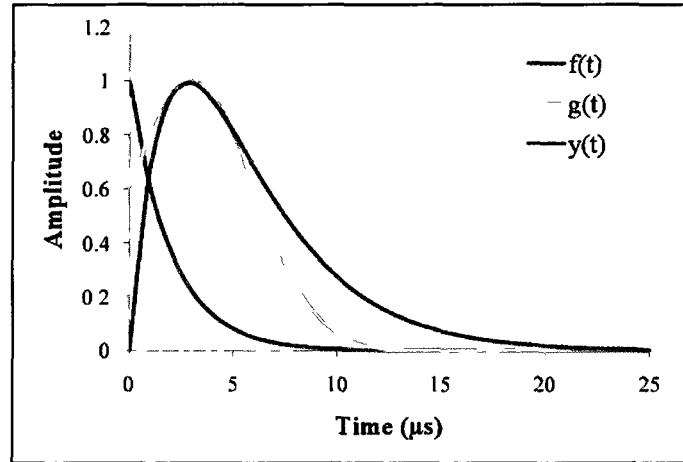


Figure 5.9 Preamplifier input and desired filter output.

The Laplace transforms of $f(t)$ and $y(t)$ are given in Equations 5.6 and 5.7:

$$F(s) = L\{e^{-\alpha t}\} = \frac{1}{s+\alpha}, \tag{5.6}$$

$$Y(s) = L\{A(e^{-\beta t} - e^{-\gamma t})\} = A \frac{\gamma - \beta}{s^2 + (\beta + \gamma)s + \beta\gamma}. \tag{5.7}$$

The transfer function needed to transform the input signal into the output signal is obtained by dividing the output by the input in the s domain (Equation 5.8),

$$H(S) = \frac{Y(s)}{F(s)} = A \frac{(\gamma - \beta)(s + \alpha)}{s^2 + (\beta + \gamma)s + \beta\gamma}. \tag{5.8}$$

After obtaining a transfer function, the system realization can be performed. System realization uses a combination of summer and integrator circuits to create the transfer function. The canonical realization for the transfer function is shown in Figure 5.10.

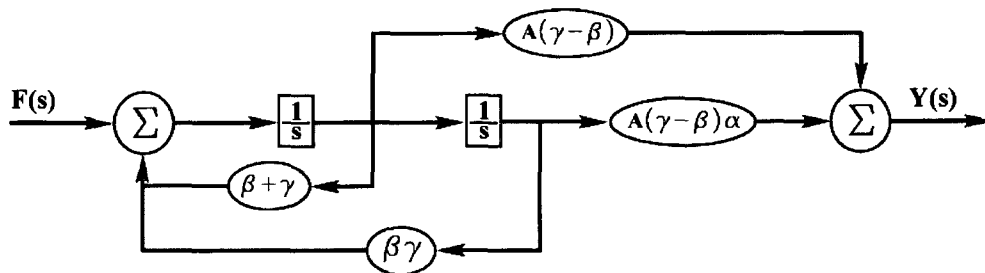


Figure 5.10 Canonical representation of the transfer function $H(s)$.

The canonical representation of a circuit is a quick method to break down the transfer function into its basic components. The next step would be to transfer the blocks from the canonical form into electronic circuits using operational amplifiers. The canonical form shows that the circuit would require two summers, two integrators, and multiple gain amplifiers to create the transfer function. It would not be practical to implement that many op-amps into a circuit; it would take up too much space on a PCB or in the case of an IC with integrated passive components, the passive component would take up too much valuable die area.

To reduce the number of operational amplifiers needed to implement the filter, specific types of active filter designs can be used. Active filters are a good option because a good active filter design uses only a few components, typically has a transfer function that is insensitive to component tolerances, is easily adjusted, only requires a small spread of component values, and can realize a wide range of transfer functions [56]. A common active filter configuration is a modified Sallen-Key filter shown in Figure 5.11.

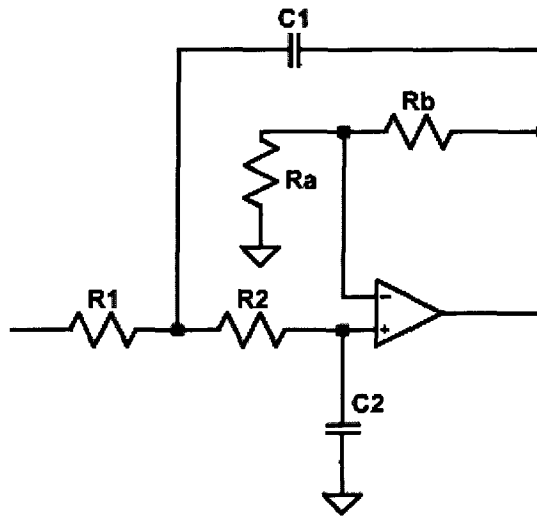


Figure 5.11 Schematic of a Sallen-Key low pass filter.

The Sallen-Key filter is a good starting point for the filter design because of its transfer function. The transfer function of the Sallen-Key filter is given in Equation 5.9; the function is rather similar to the calculated transfer function from Equation 5.8.

$$H(s) = \frac{K\omega^2}{s^2 + 2\alpha s + \omega^2}, \quad (5.9)$$

where,

$$K = 1 + \frac{R_b}{R_a}, \quad (5.10)$$

$$\omega^2 = \frac{1}{R_1 R_2 C_1 C_2}, \quad (5.11)$$

and

$$2\alpha = \frac{1}{R_1 C_1} + \frac{1}{R_1 C_2} + \frac{1}{R_2 C_2} (1 - K). \quad (5.12)$$

The full derivation of the transfer function for a Sallen-Key circuit can be found in the text by B.P. Lathi, *Signal Processing & Linear Systems* [57]. The advantage of using a Sallen-Key filter is that it gives a two pole system using only one operational amplifier. It is also possible to cascade multiple Sallen-Key filters, which will increase the number of poles in the system. Using this type of filter it is possible to get an n th-order filter using only $n/2$ circuits [56]. The more poles in the system, the more customizable the filter. Any component in the Sallen-Key filter can be adjusted to affect the filter, which later will be important when the passive components are included inside of an integrated circuit [58]. The capacitor will take a lot more room on chip than a resistor, so if the capacitor values can be held constant and are reasonably small capacitances, then less area will be used on the chip die. The Sallen-Key filter also can amplify the signal, reducing the need for additional amplifiers.

The initial discrete component design uses two Sallen-Key filters cascaded with each other to create a four pole system. Since the preamplifier's output first passes through a high pass filter to remove any DC offset from the PM tube, the total filter is a 5th order system. The schematic of the 5th order filter is shown in Figure 5.12. The initial component values were determined from the values found by calculating the constants from Equation 5.8 and then adjusted by trial and error using LT Spice to get the desired output. Figure 5.13 shows the simulated LT Spice output and the original output waveform $y(t)$ from Equation 5.5.

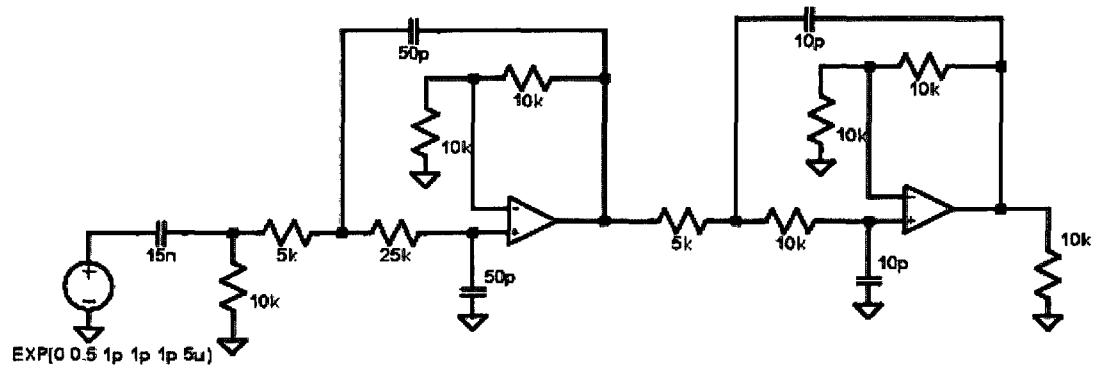


Figure 5.12 Schematic of 5th order filter.

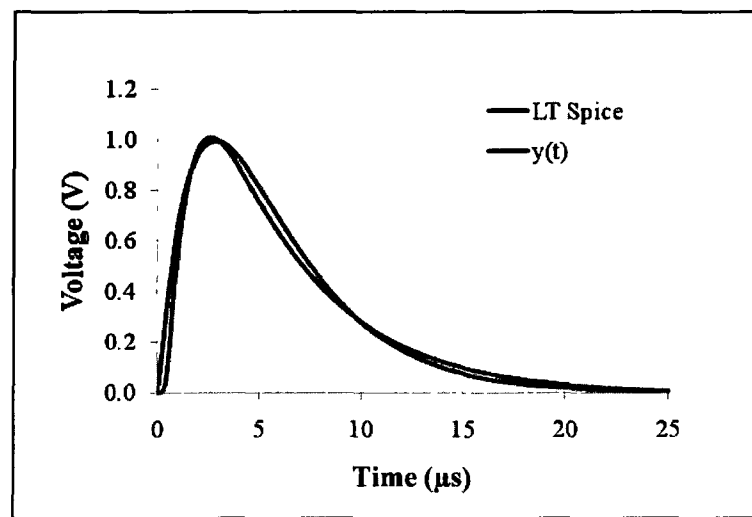


Figure 5.13 LT Spice simulation versus the desired output $y(t)$.

The negative feedback section of the two active filters can be adjusted to add a voltage gain to the filter section without adding additional operational amplifiers. The gain can be easily adjusted to the supply voltage so that the different pulse peaks are easy to differentiate without strong pulses reaching the supply voltage rails.

5.1.3 Peak Detection and Comparator Trigger

The peak detector circuit is used to hold the peak voltage of the pulse that is at the output of the filter. The purpose of the circuit section is to hold the peak voltage so that a microcontroller can sample and record the peak pulse value. An ideal peak detector will produce a DC output that is equal to the peak value of the input signal [56]. A basic peak detector can be constructed with a diode and a capacitor. This simple circuit is effective but will not hold the true peak value of the circuit because the load impedance will slowly discharge the capacitor. To avoid capacitor discharging, the peak detection circuit can have a unity gain buffer at the front and back of the circuit, shown in Figure 5.14.

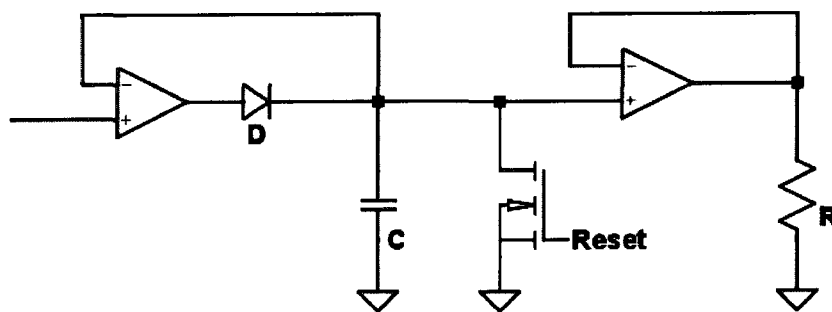


Figure 5.14 Schematic of a peak detector with op-amp buffers.

The voltage follower at the output of the peak detector supplies the load resistor with current so that the capacitor does not need to supply the current. Since the output buffer is unity gain, the output voltage of the operational amplifier is equal to the value of the capacitor voltage. This configuration helps hold the total peak voltage at the output to

have accurate sampling. Since the load is no longer discharging the capacitor, a MOSFET switch is required to reset the peak detector. The time it takes to charge the capacitor is affected by the size of the capacitor and the slew rate of the operational amplifier. A sample output of the peak detector circuit is shown in Figure 5.15. The input to the detector is the output waveform of the filter circuit from Figure 5.13.

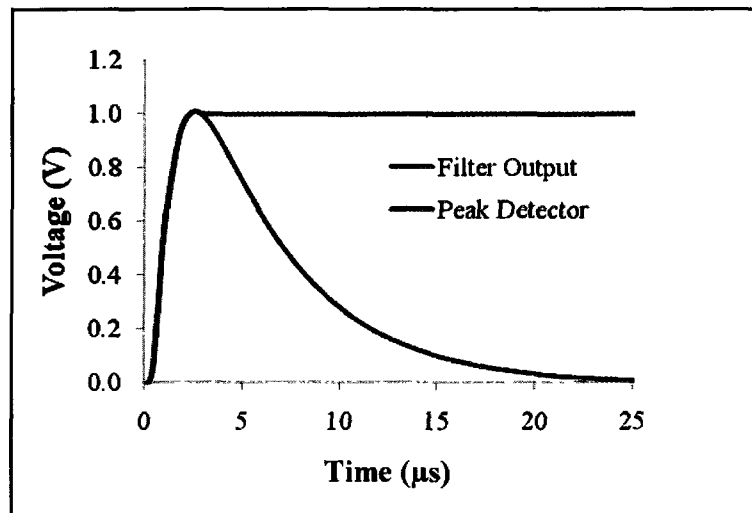


Figure 5.15 Peak detector output waveform.

A comparator trigger is the last part of the circuit that was constructed. An ideal comparator compares two voltages and will produce a logic output signal, either high or low, depending on which input voltage signal is the largest. Comparators have inverting and non-inverting input terminals. When the non-inverting input is larger than the inverting input signal, the output of the comparator will be high; when the inverting input has the larger voltage the output is low. My circuit uses the comparator as a trigger for the recording microcontroller. Microcontrollers can easily be programmed to record the voltages on specific pin when a trigger voltage on another pin is detected. The comparator is setup with a voltage divider on the inverting input to set a trigger voltage.

The trigger voltage is set slightly higher than the noise level of the circuit. Non-inverting input is connected to the filter output. The filter output will set the comparator to go high when a pulse goes beyond the inverting voltage. The comparator output is then used to tell the microcontroller to begin recording the peak detector's output. The comparator trigger circuit is shown in Figure 5.16.

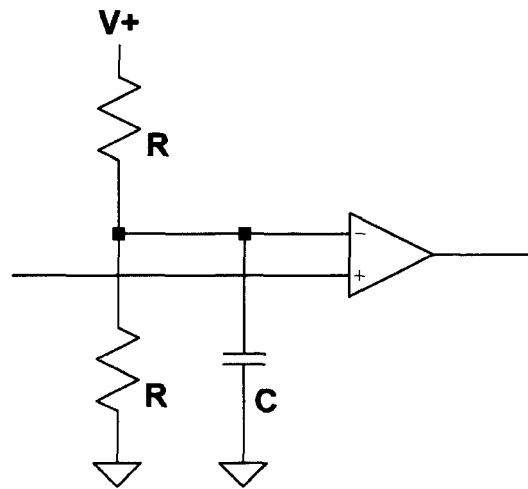


Figure 5.16 Comparator circuit used to trigger a microcontroller.

5.1.4 Complete Radiation Spectroscopy Circuit

Once all the circuit sections were calculated and simulated, the complete circuit schematic was created and simulated. Once simulated, the circuit was initially constructed out of discrete components (Figure 5.17).

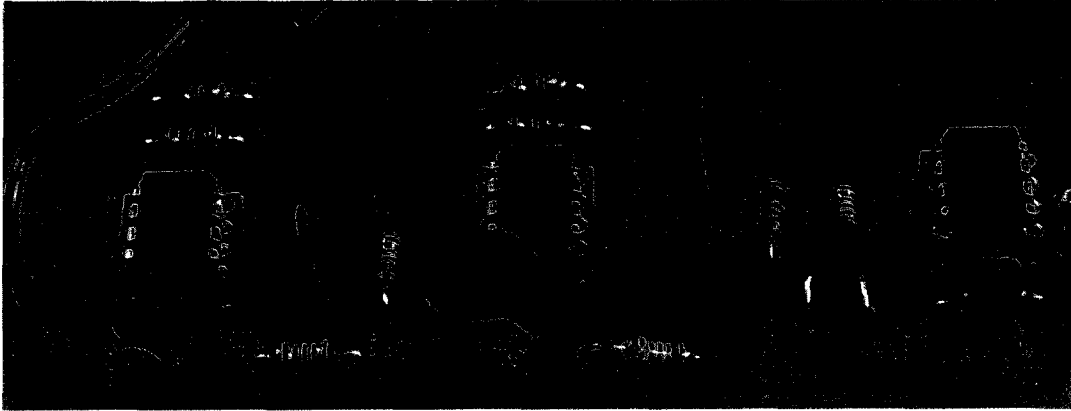


Figure 5.17 Discrete circuit charge sensitive pre-amplifier and Sallen-Key filters.

The discrete component circuit is a rather large single sided PCB board that is not optimized for space considerations. To create a small sensor package that is cheap to produce and deploy in large numbers, the circuit needs to be reduced. To decrease the overall size of the circuit, it has to be reduced into a custom integrated circuit. Since the size of an integrated circuit is largely dependent on the number of components, the circuit was reduced to using one Sallen-Key filter, and filter components were recalculated to use smaller capacitors. The capacitors take up the most space in the integrated circuit layout, so reducing their value saves a lot of space. Figure 5.18 shows the new schematic for the radiation spectroscopy circuit.

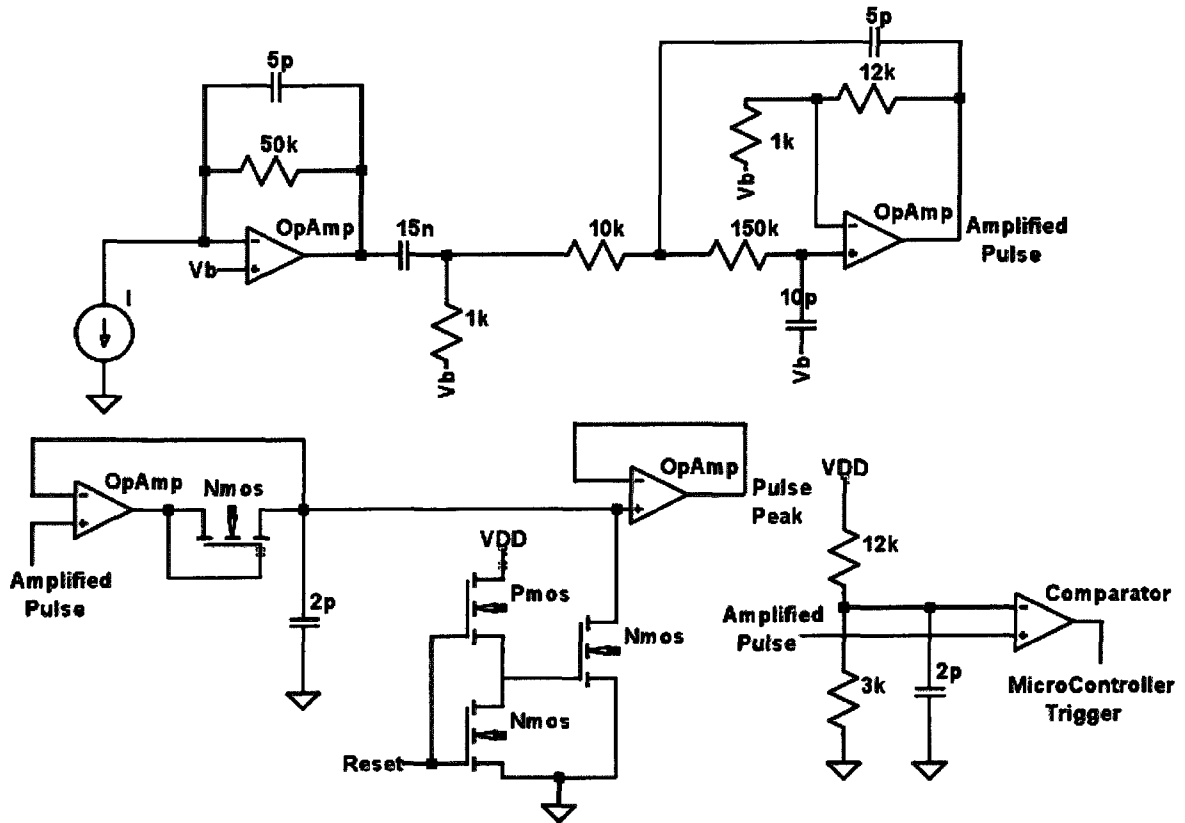


Figure 5.18 Radiation spectroscopy circuit for the integrated circuit layout.

Figure 5.19 shows the output waveforms for the schematic in Figure 5.18. We can see that the filtering circuit produces more of an exponential waveform than a Gaussian, but the trade-off for this is a significant reduction in the chip area needed for the integrated circuit.

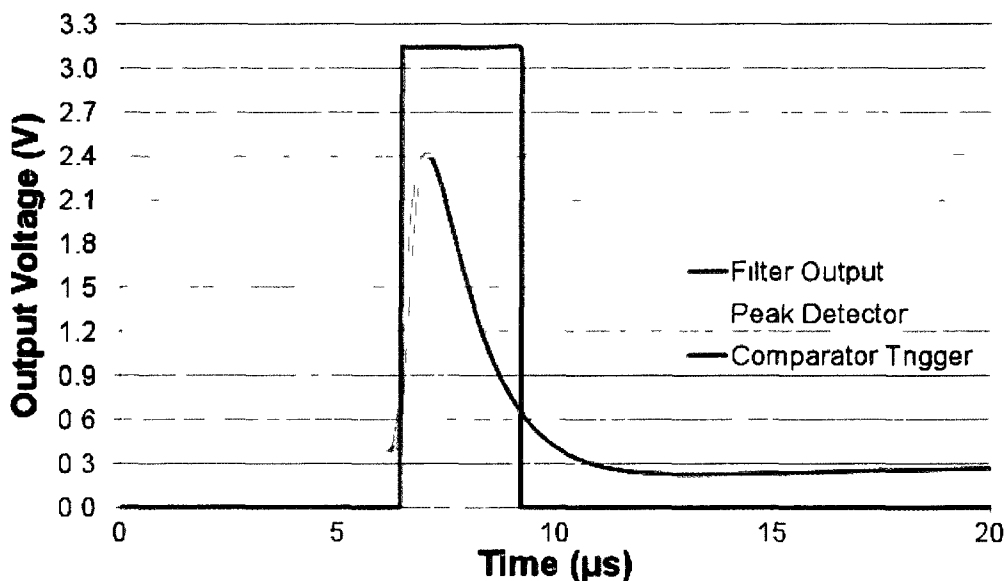


Figure 5.19 Output waveform of the radiation spectroscopy circuit.

5.2 Integrated Circuit Design

Integrated circuits are the heart of today's high tech world. On September 12th, 1958, Jack Kilby demonstrated the first working semiconductor integrated circuit [59]. Since then, integrated circuits have revolutionized the world electronics. Almost every electronic device that is a part of our everyday life contains integrated circuits.

Having the ability to integrate a large number of transistors and passive components on a single chip has two major advantages over discrete component circuits: lower cost and better performance. Integrated circuits have a low cost when they are produced in mass because all of the components are produced at one time on the same chip. The circuit is not constructed one transistor at a time, as with discrete components, and less material is used since all the transistors are on a single die, instead of a die for each individual transistor. Integrated circuits also often have better performance because the overall size of the transistors is smaller; the compact design improves signal speed

and switching between components. The smaller components will also consume less power than individual discrete components.

To create a detector that will have a small physical footprint and can be cheaply mass produced, a custom integrated circuit is needed. A single chip design will reduce the previously designed discrete component circuit into a small compact circuit with little additional off-chip components. The technology that was used for my design was Taiwan Semiconductors (TSMC) 0.35 micron process. This technology is a double polysilicon process with up to four metal layer interconnects and is used with a supply voltage of 3.3 volts. There is also an option to use a thick oxide layer for 5 volt transistors. This technology was chosen mainly for the double polysilicon feature which allows for poly2 over poly capacitors to be constructed. The capacitance for poly2 over poly is $850 \text{ aF}/\mu\text{m}^2$.

When designing analog IC circuits, the capacitors are the components that take up the most layout area. Using a poly2 over poly capacitor gives the highest linear capacitance per unit area.

5.2.1 Amplifier Design

Multiple operational amplifiers were used in the discrete circuit design, so this was the first component designed for the integrated circuit package. The amplifier needs to operate with a supply voltage of 3.3 volts and have a large output swing for amplification of the radiation pulse heights. A large output swing will allow easier discrimination between each radiation pulse. The amplifier was designed using several basic CMOS designs constructed together to create a two stage op-amp.

Amplifier design starts off with understanding the basic single stage MOSFET amplifier. Common-source amplifiers are widely used single stage amplifiers. The basic topologies of the common-source amplifier that use gate-drain connected loads are shown in Figure 5.20; transistors M1 and M2 are both assumed to be biased in the saturation region.

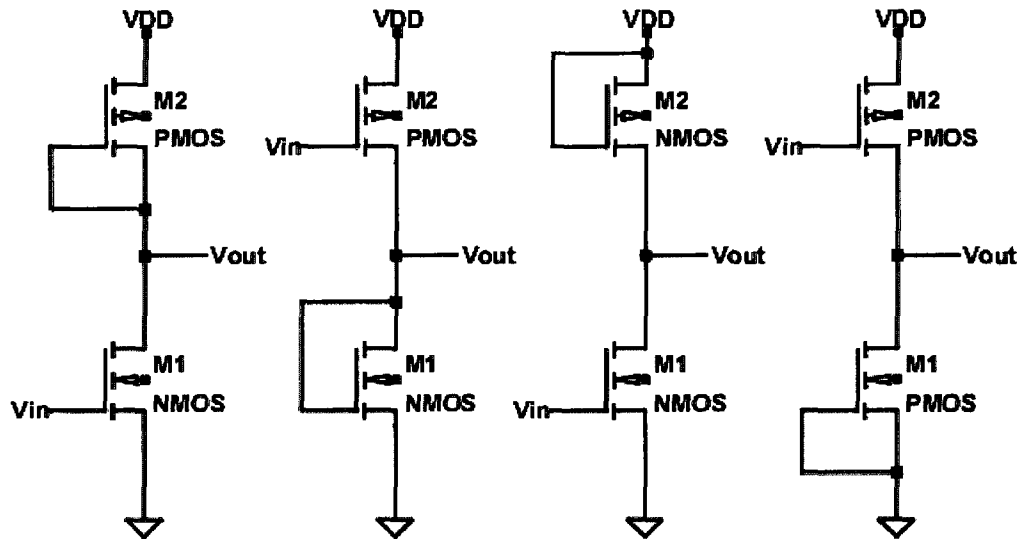


Figure 5.20 Four common-source amplifier configurations.

To understand how this type of amplifier operates, we can replace M2 with a resistance with a value of $1/g_{m2}$ and replace M1 with a current source with a value of $g_{m1}v_{in}$. The value g_m is the transconductance of the transistor. For proper operation $1/g_{m2}$ must be much smaller than the parallel combination of the transistors output resistances. The gain of the common source amplifier is given by Equation 5.13:

$$\frac{v_{out}}{v_{in}} = \frac{-i_d \frac{1}{g_{m2}}}{i_d \frac{1}{g_{m1}}} = -\frac{g_{m1}}{g_{m2}} \quad (5.13)$$

This equation shows that the small signal gain for a common source amplifier is the resistance in the drain of M1 divided by the resistance looking into the source of M1 added to any resistance between the source of M1 and ground.

Common-source amplifiers are also used with a current source load shown in Figure 5.21. M1 is the common source amplifier, while M2 is the current source load. Current source loads provide the amplifier with the largest possible load resistance, allowing for the largest gain.

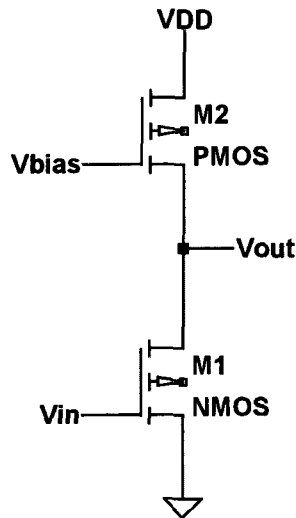


Figure 5.21 Common-source amplifier with a current source load.

The gain of this configuration is given by Equation 5.14.

$$\frac{v_{out}}{v_{in}} = -\frac{r_{o1} || r_{o2}}{\frac{1}{g_{m1}}} = -g_{m1}(r_{o1} || r_{o2}), \quad (5.14)$$

where r_o is the output resistance of the transistor. The gain of this amplifier can further be increased by replacing M2 with a cascode current load. With a cascode load, the resistance looking into the drain of M1 is much larger than the output resistance of M1. This type of configuration leads to the maximum gain possible by a single MOSFET. The open circuit gain of M1 is given by Equation 5.15:

$$gain = \frac{r_{o1}}{\frac{1}{g_{m1}}} = -g_{m1}r_{o1}. \quad (5.15)$$

The next type of amplifier expanding the common source amplifier is cascode amplifier configuration. Cascode amplifier uses multiple current source loads cascoded together to achieve much larger gains than what is possible with the simple common-source amplifier and eliminates the Miller effect that associated with this type of amplifier. The Miller effect refers to the impedance between the input of an amplifier and another node. This impedance can affect the input impedance of the amplifier. One type of cascode amplifier is given in Figure 5.22; the resistance at the drain of M3 is given by $g_{mp}r_{op}^2$, and the resistance looking into the drain of M2 is $g_{mn}r_{on}^2$.

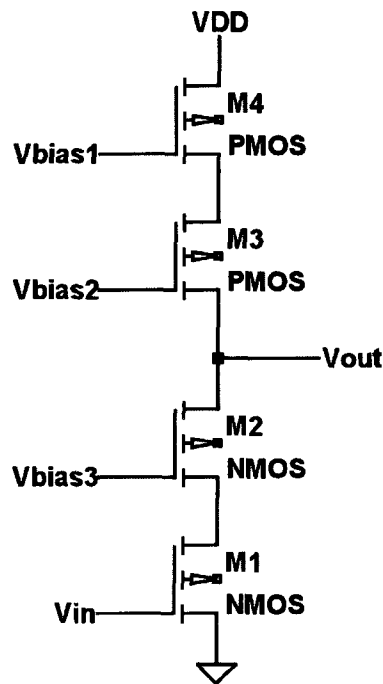


Figure 5.22 Cascode amplifier configuration.

The gain of the amplifier is then given by Equation 5.16:

$$\frac{v_{out}}{v_{in}} = -\frac{g_{mn}r_{on}^2 || g_{mp}r_{op}^2}{\frac{1}{g_{mn}}} = -g_{mn}(g_{mn}r_{on}^2 || g_{mp}r_{op}^2). \quad (5.16)$$

configuration is later used in conjunction with a differential amplifier to make a two stage amplifier.

For practical applications of common-source and cascode amplifiers, an output buffer is needed to drive a resistive load adequately. A push-pull amplifier is used as an output buffer. Push-pull amplifiers have a topology like an inverter, where the output can swing from VDD to ground. Figure 5.24 shows an example of a push-pull amplifier; with zero AC input current, M1 and M2 have the same current as M3 and M4. M3 and M4 set the current in the output stage.

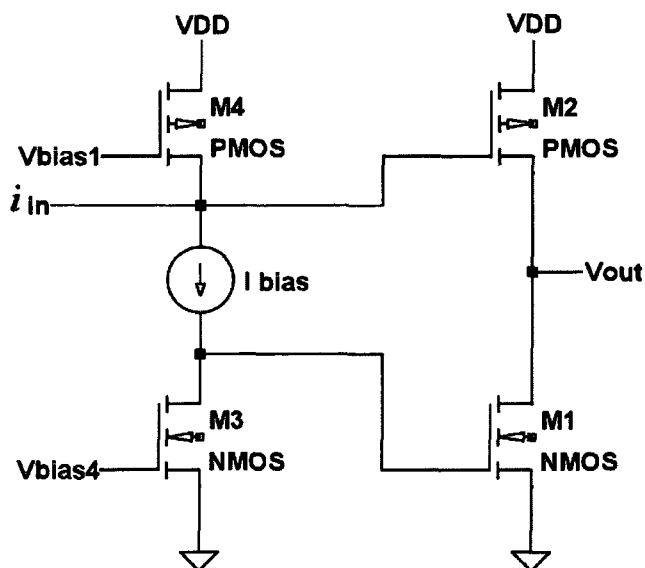


Figure 5.24 Push-pull output topology.

When a positive AC input current flows into the circuit, the gate voltage of M1 and M2 rises, and M2 eventually shuts off. When negative current flows into the pair, the gate of M1 will drop, eventually shutting off. This operation makes M1 and M2 pull and push current to and from the output. This topology is useful because the output voltage swing is very close to VDD and ground.

The previously discussed amplifiers require that large resistors and capacitors are used to bias the input transistor to the correct operating point. Without proper biasing, the current load will not source current equal to the current in the input transistor when both transistors are in saturation. To solve this, differential amplifiers are used at the input of the amplifier so that the input voltages can move up and down without affecting the biasing of the gain stage. By doing this, the bias voltage is no longer a function of the input voltage. A source-coupled pair, also known as a differential pair, is shown in Figure 5.25.

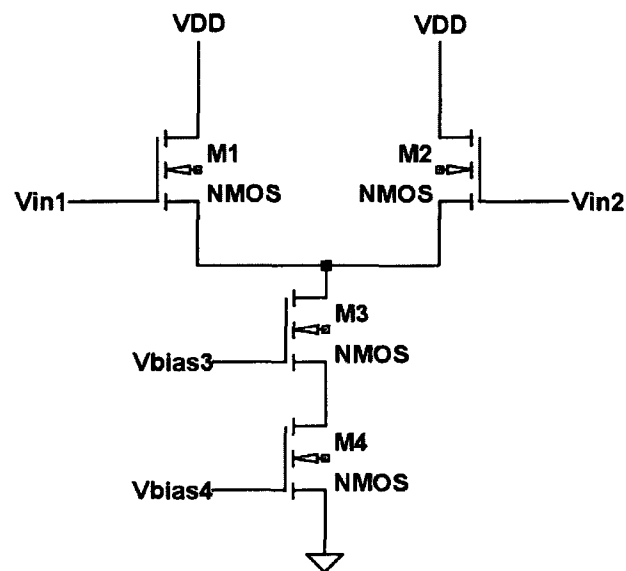


Figure 5.25 NMOS source-coupled differential pair.

With a differential pair, the voltage at the input of M1 and M2 are equal when there is no input signal. As a signal is input into one of the MOSFETs, the voltage difference between the pair increases; this voltage difference can then be amplified. Figure 5.26 shows a differential pair with a current load. When the differential pair inputs

are unbalanced, the output of the amplifier will move towards VDD or ground depending on the difference between the gates of M1 and M2.

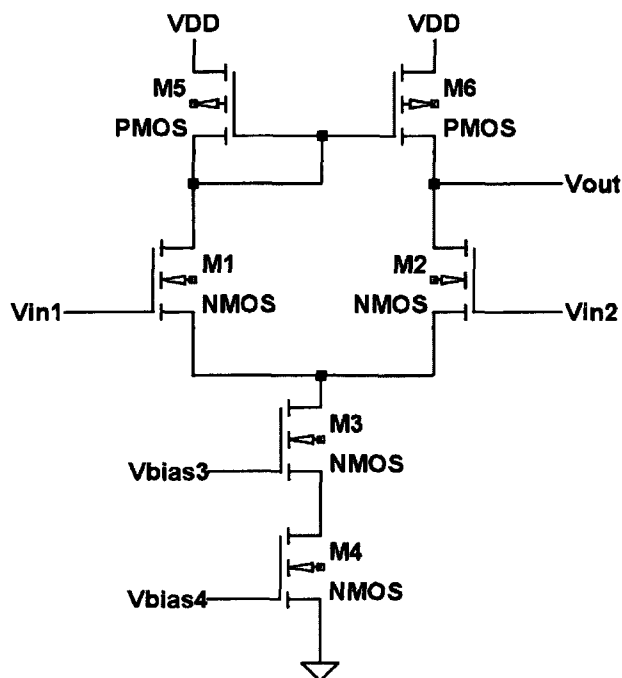


Figure 5.26 Differential amplifier with a current mirror load.

Another feature of differential amplifiers is they can reject a signal that is common to both inputs. In ideal cases with a perfectly matched pair, noise that is found in both analog signals can be completely cancelled out with the use of differential amplifiers.

5.2.2 Operational Amplifier Design

Operational amplifiers are constructed using the basic building block previously discussed. The basic construction is shown in Figure 5.27. The amplifier consists of a differential amplifier in the first stage followed by a second gain stage.

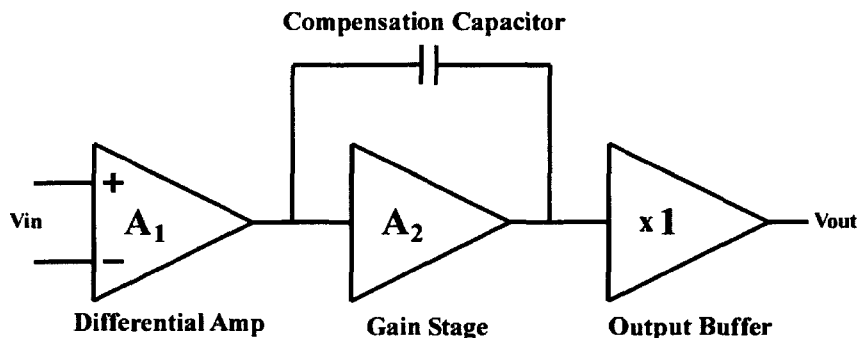


Figure 5.27 Two-stage operational amplifier block diagram.

For driving resistive and large capacitive loads, an output buffer is needed at the output of the second gain stage. There is also usually a need for a capacitor with the second stage which affects the poles of the system, lowering the gain at higher frequencies. Moving the poles will reduce the overall bandwidth of the amplifier but allows for a stable design.

Figure 5.28 shows the op-amp design for my integrated circuit. This design is based off of all the elements that have previously been discussed.

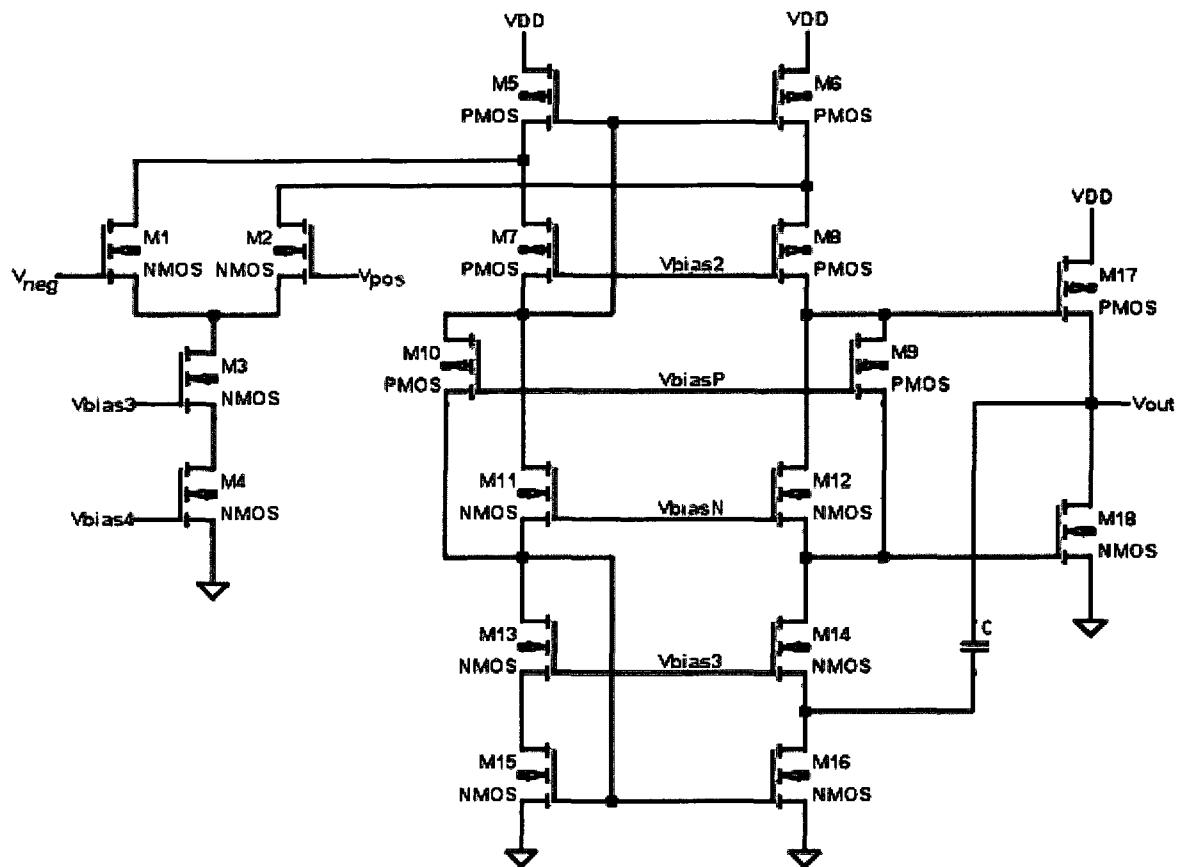


Figure 5.28 Two-stage operational amplifier design.

The first stage consists of a differential amplifier constructed from M1 – M4. The input pair M1 and M2 is a differential pair and sized to accept very small current sources that are supplied from the photomultiplier tubes and photodiodes. M3 and M4 are used to set the bias current for the input pair. M5 and M6 act as the current load for the first stage; the M5 and M6 pair are twice the size of M7 and M8 to supply enough current to both the input differential amplifier and the folded cascode gain stage. The gain stage of the amplifier consist of MOSFETs M5 – M8 and M13 – M16; this stage increases the overall gain of the amplifier and allows for the output voltage to swing to nearly VDD and ground. This last part of the amplifier is the output buffer. M9 – M12 act to bias the push-pull pair M17 and M18. The compensation capacitor is connected to the output to

move the poles of the amplifier to allow for more stable operation. The larger the compensation capacitor, the more stable the amplifier; the trade-off to this is that it will affect the speed and bandwidth of the amplifier. The transistor sizes are given in Table 5.1.

Table 5.1 Transistor sizes for the operational amplifier

Component	Model	Size	Component	Model	Size
M1	NMOS	200/1	M10	PMOS	50/1
M2	NMOS	200/1	M11	NMOS	25/1
M3	NMOS	100/1	M12	NMOS	25/1
M4	NMOS	100/1	M13	NMOS	50/1
M5	PMOS	200/1	M14	NMOS	50/1
M6	PMOS	200/1	M15	NMOS	50/1
M7	PMOS	100/1	M16	NMOS	50/1
M8	PMOS	100/1	M17	PMOS	100/1
M9	PMOS	50/1	M18	NMOS	50/1

5.2.3 Biasing Circuit Design

The biasing circuit used to bias transistors in the op-amp is a rather complex design because of the various voltages needed to have all the amplifier's transistors operating in saturation. The biasing circuit used in my chip is based off of a biasing circuit designed by R. J. Baker published in his text *CMOS Circuit Design, Layout, and Simulation* [60]. The base design in most biasing circuits is the current mirror configuration. A simple current mirror is shown in Figure 5.29, using two transistors, M1 and M2.

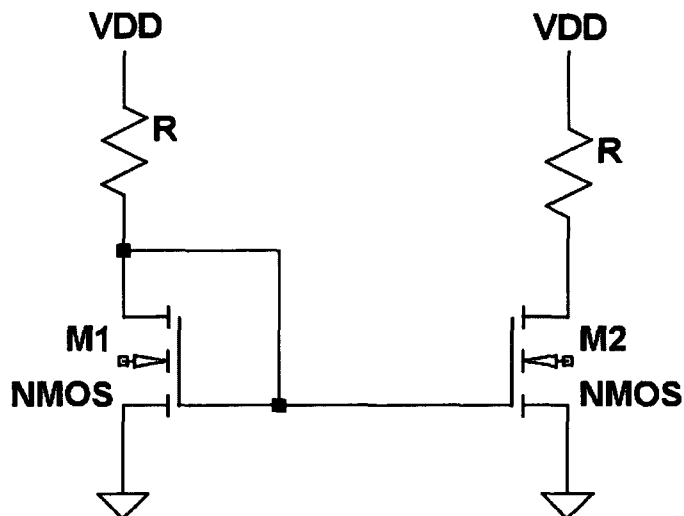


Figure 5.29 Basic current mirror with resistor loads.

If both transistors are the same length and width, then $V_{GS1} = V_{DS1} = V_{GS2}$. Since we know that the transistors have the same gate voltage, it is expected that they would also then have the same drain current. With matching resistors, the potential at the drain of M2 would be the same as the potential of the drain on M1. When using current mirrors, the output current can be adjusted by scaling the width of M2. A general equation for this is given in Equation 5.17, assuming that the lengths of the transistors are the same:

$$\frac{I_{M2}}{I_{M1}} = \frac{W_{M2}}{W_{M1}} \quad (5.17)$$

Current mirrors are usually not made with resistors in their design; instead they are made using a second transistor as the current load similar to what was previously discussed in designing the amplifier components. By using a transistor as the load, the current of the mirror is not affected as much by the supply voltage variations. Using a resistive load leaves the current mirror linearly dependant on supply voltage.

A more complex current mirror is shown in Figure 5.30. This circuit has two parts; it has what is known as a beta multiplier reference mirror and a start up circuit.

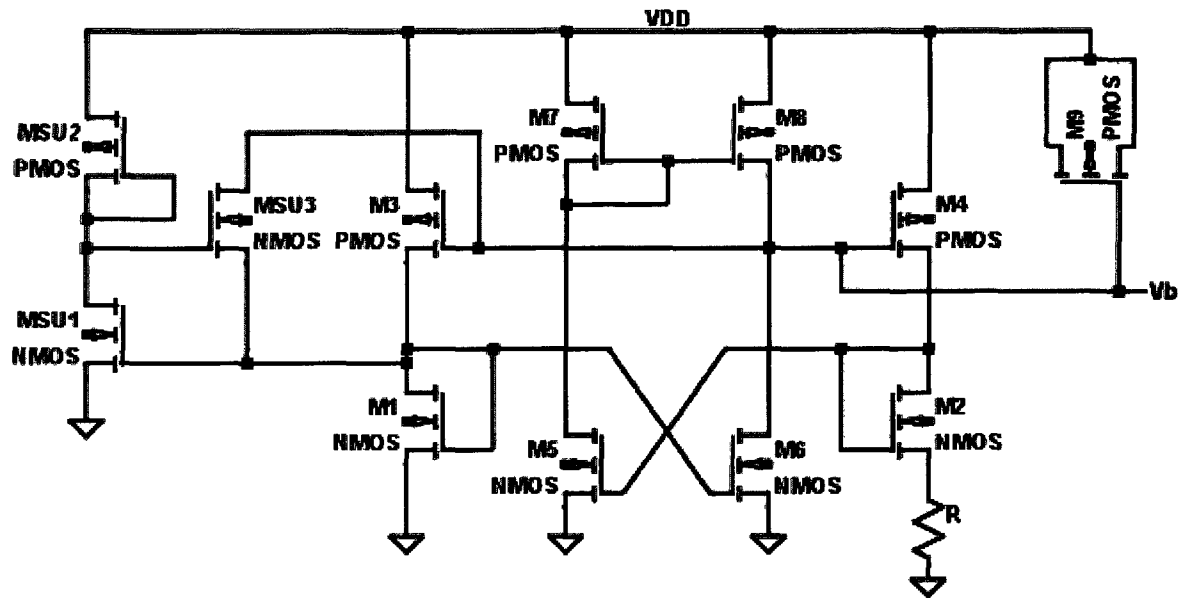


Figure 5.30 Current reference circuit with start-up circuit.

The startup circuit is important because in self-biasing circuits, there are two possible operating points. There is an unwanted state which no current flows in the circuit when the gates of the NMOS transistors are grounded while the PMOS gates are at VDD. When in this state, MSU3 acts as a switch and leaks current into the gates of the NMOS transistors from the gates of the PMOS transistors. This results in the currents of the mirror going to the desired operating point and then turning off MSU3. In this circuit the beta multiplier is combined with a differential amplifier constructed from M5-M8. The amplifier is added into the circuit so that the design will not be affected by variations from the power supply. The object is for the amplifier to compare the drain voltage of M1 to the drain of M2 and regulate the two; the connection V_b is used to create voltage

reference for the bias circuit. Table 5.2 gives the transistor sizes for the current reference circuit with start-up transistors.

Table 5.2 Transistor sizes for the current reference circuit

Component	Model	Size	Component	Model	Size
MSU1	NMOS	50/2	M5	NMOS	50/2
MSU2	PMOS	22/2	M6	NMOS	50/2
MSU3	NMOS	10/2	M7	PMOS	100/2
M1	NMOS	50/2	M8	PMOS	100/2
M2	NMOS	200/2	M9	PMOS	100/100
M3	PMOS	100/2	R	Resistor	5.5 k-ohms
M4	PMOS	100/2			

The op-amp previously discussed needs a number of different reference voltages to operate correctly. The various voltage references are created using current mirrors starting from the V_b reference. Figure 5.31 shows the current mirrors for the first three references.

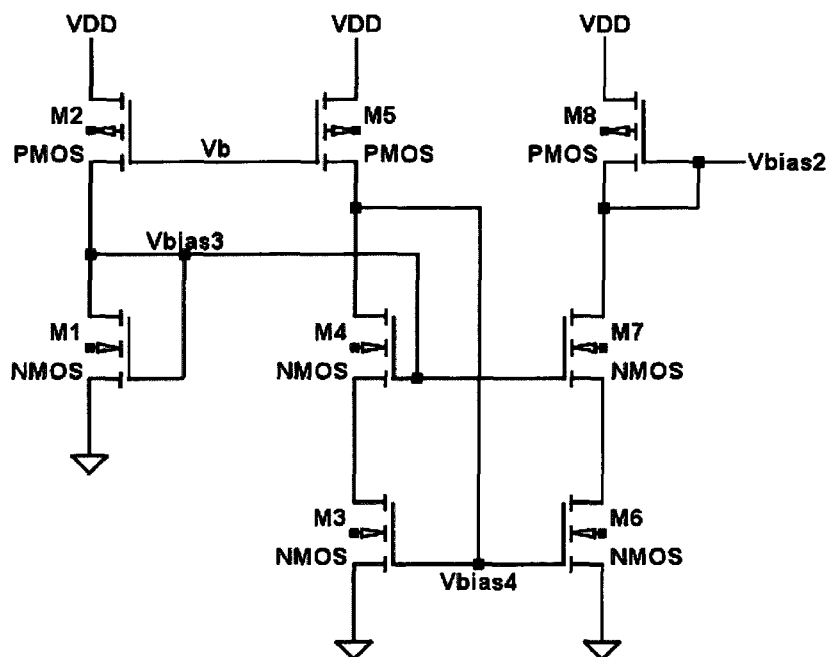


Figure 5.31 Current mirrors for bias voltages 2, 3, and 4.

The first current mirror that is created between M1 and M2 sets the voltage for V_{bias3} using the voltage reference V_b . Once a bias voltage is set, it can then be used in other mirrors to create more voltage levels. Using the bias voltage from V_b and V_{bias3} , the next reference voltage, V_{bias4} , can be created using M3, M4, and M5. Then, using V_{bias3} and V_{bias4} , we can use M6, M7, and M8 to set the reference voltage for V_{bias2} . Figure 5.32 shows the second half of the current mirrors; these mirrors set the voltage for V_{bias1} , V_{biasN} , and V_{biasP} . The transistor sizes to the current mirror section of the bias circuit are given in Table 5.3.

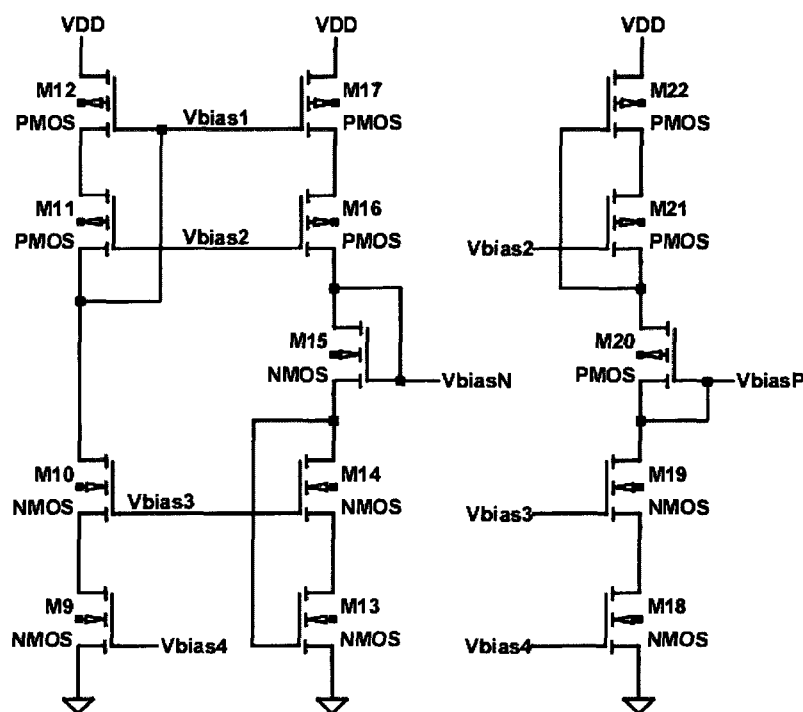


Figure 5.32 Current mirrors for bias voltages 1, N, and P.

Table 5.3 Transistor sizes for the current mirror bias circuit

Component	Model	Size	Component	Model	Size
M1	NMOS	10/10	M12	PMOS	100/2
M2	PMOS	100/2	M13	NMOS	50/2
M3	NMOS	50/2	M14	NMOS	50/2
M4	NMOS	50/2	M15	NMOS	50/2
M5	PMOS	100/2	M16	PMOS	100/2
M6	NMOS	50/2	M17	PMOS	100/2
M7	NMOS	50/2	M18	NMOS	50/2
M8	PMOS	20/10	M19	NMOS	50/2
M9	NMOS	50/2	M20	PMOS	100/2
M10	NMOS	50/2	M21	PMOS	100/2
M11	PMOS	100/2	M22	PMOS	100/2

5.2.4 Comparator Circuit Design

The final circuit that was designed for the integrated circuit was a comparator circuit. Comparators operate as a decision making circuit. The basic block schematic is shown in Figure 5.33.

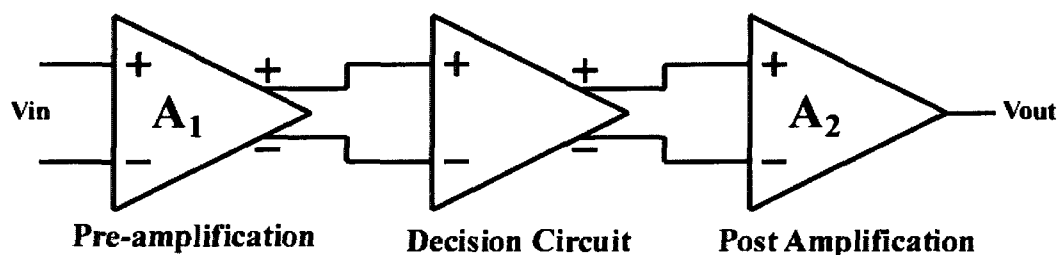


Figure 5.33 Block diagram of a comparator.

If the positive input is at a higher potential than the negative input, the output of the comparator will be logic level 1, ideally VDD. When the negative input rises above the positive input, the logic level is 0, or ground. Op-amps can be used as voltage comparators but only for low frequency and slow speed applications. Circuits that are

designed as comparators are able to be specifically tailored for sensitivity and propagation delay.

The circuit has three stages: pre-amplification, decision stage, and post amplification with an output buffer. The pre-amplification stage is a fully differential amplifier; fully differential amplifiers have both differential inputs and differential outputs. This stage amplifies in the input signals and improves the comparator's sensitivity. This stage will also isolate the input from switching noise, which is from the positive feedback in the decision making stage. Figure 5.34 shows the input stage of my comparator.

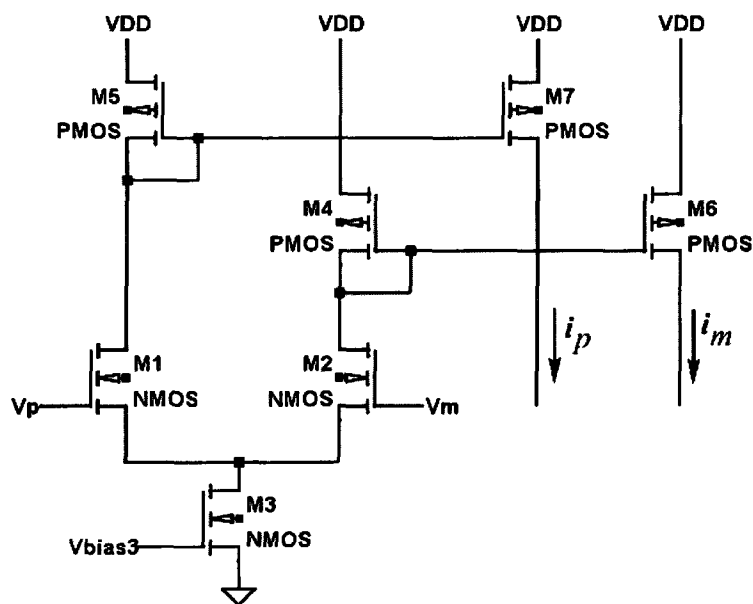


Figure 5.34 Comparator pre-amplification stage.

The sizes of M1 and M2 are set by considering how much gain and input capacitance is desired. The transconductance of the MOSFETs controls the gain of the input stage, while the size of the MOSFETs controls the input capacitance. The pre-

amplification stage differential outputs i_p and i_m are fed into the decision circuit of the comparator (Figure 5.35).

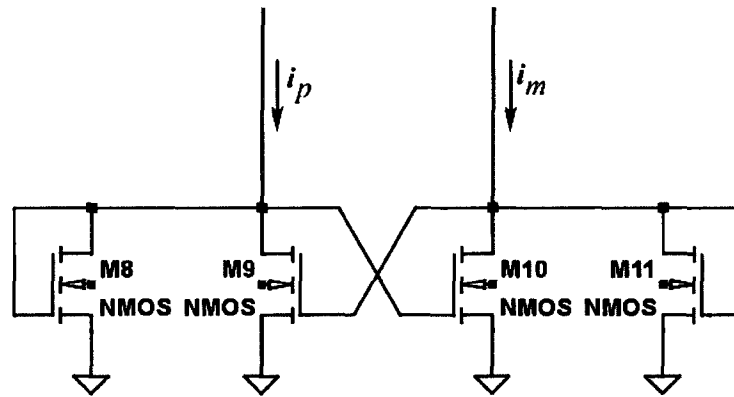


Figure 5.35 Comparator decision circuit.

The decision circuit operates by using positive feedback from the crossed gate connection at M9 and M10. If we assume that the current i_p is larger than i_m , then M8 and M10 are initially on, and M9 and M11 are off. As the current i_m increases and i_p decreases, switching will take place when gate-source voltage of M11 reaches the turn on voltage threshold. As M11 goes past the turn on voltage, M9 starts to take current from M8. This decrease in current will eventually turn off M10, completing the switch. Hysteresis can be implemented into the decision circuit by changing the transistor designs so that M8 and M10 do not have the same beta values as M9 and M11. By not using a common centroid matching for the transistor, the integrated circuit process will produce a slight variation between the transistors. The circuit is able to discriminate mV level signals and will have some hysteresis to reject noise from the input signal.

Comparator post amplification and the output buffer is the last stage of the circuit. It amplifies the output of the decision circuit, which results in a logic signal of VDD or 0. Since the output of the decision circuit is differential, I used a differential amplifier for

the last stage. The differential amplifier is a simple self biasing design with the output connected to an inverter. The inverter acts to isolate the self biasing amplifier from load capacitances. The MOSFET that is connected between the sources of the decision circuit to ground is used to move the output of the decision circuit into the common mode input range of the output amplifier. The complete comparator schematic is shown in Figure 5.36. Table 5.4 gives the transistor sizes used for the comparator.

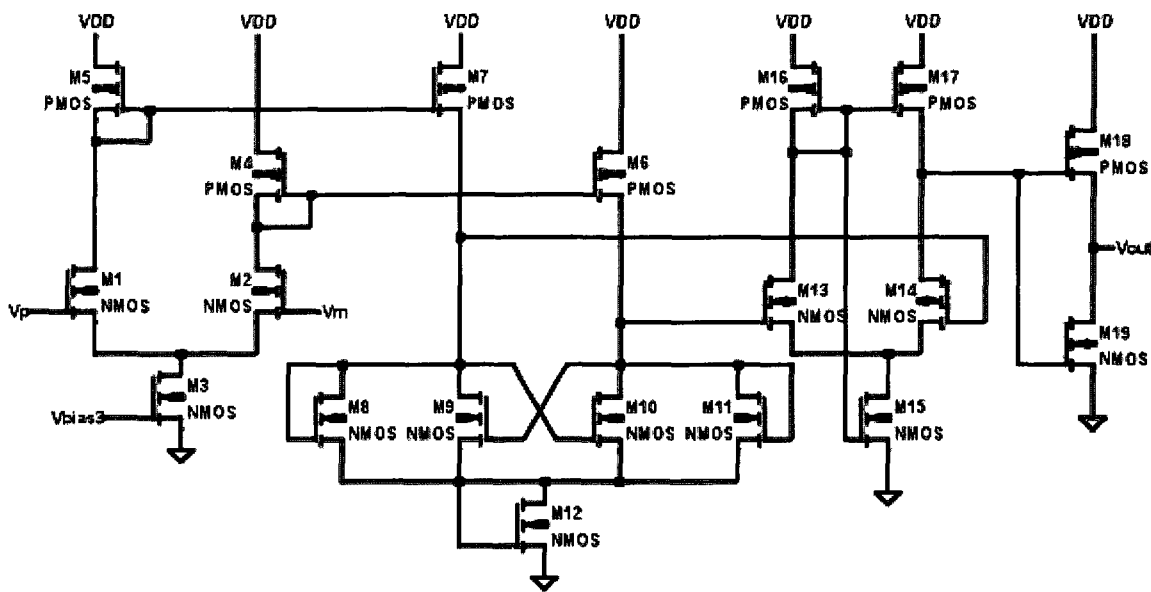


Figure 5.36 Comparator schematic.

Table 5.4 Transistor sizes of the comparator

Component	Model	Size	Component	Model	Size
M1	NMOS	200/1	M11	NMOS	25/1
M2	NMOS	200/1	M12	NMOS	10/10
M3	NMOS	50/1	M13	NMOS	50/1
M4	PMOS	30/1	M14	NMOS	50/1
M5	PMOS	30/1	M15	NMOS	50/1
M6	PMOS	30/1	M16	PMOS	40/1
M7	PMOS	30/1	M17	PMOS	40/1
M8	NMOS	25/1	M18	PMOS	100/1
M9	NMOS	25/1	M19	NMOS	50/1
M10	NMOS	25/1			

5.2.5 Operational Amplifier Simulation Results

After an initial amplifier design is constructed and transistor sizes estimated, the next step is to run a number of simulations that test different aspects of the design. To run simulations that accurately represent the operating conditions of transistor, model files for the transistors are needed. The model files for a process are supplied by the fabrication facility; for my design the model files for the TSMC 0.35 micron process are found at the MOSIS website. The model files I used were TSMC 0.35 micron T88F MM found at the MOSIS webpage [61].

The open loop gain of an amplifier is a measure of the amplifier's gain without the use of a feedback loop to regulate the gain. The number of stages in an op-amp affects the open loop gain as well as the stability of the amplifier. The more stages the amplifier has, the more poles it has to control the open loop gain; but an increase in dominant poles also affects the stability of the amplifier. The use of a compensation capacitor in the amplifier design introduces an additional dominant pole. My amplifier was tested using two different size compensation capacitors since the capacitor will have a large affect on the speed and stability of the amplifier. Figure 5.37 shows the open loop gain and phase response of the amplifier using a 500 fF compensation capacitor.

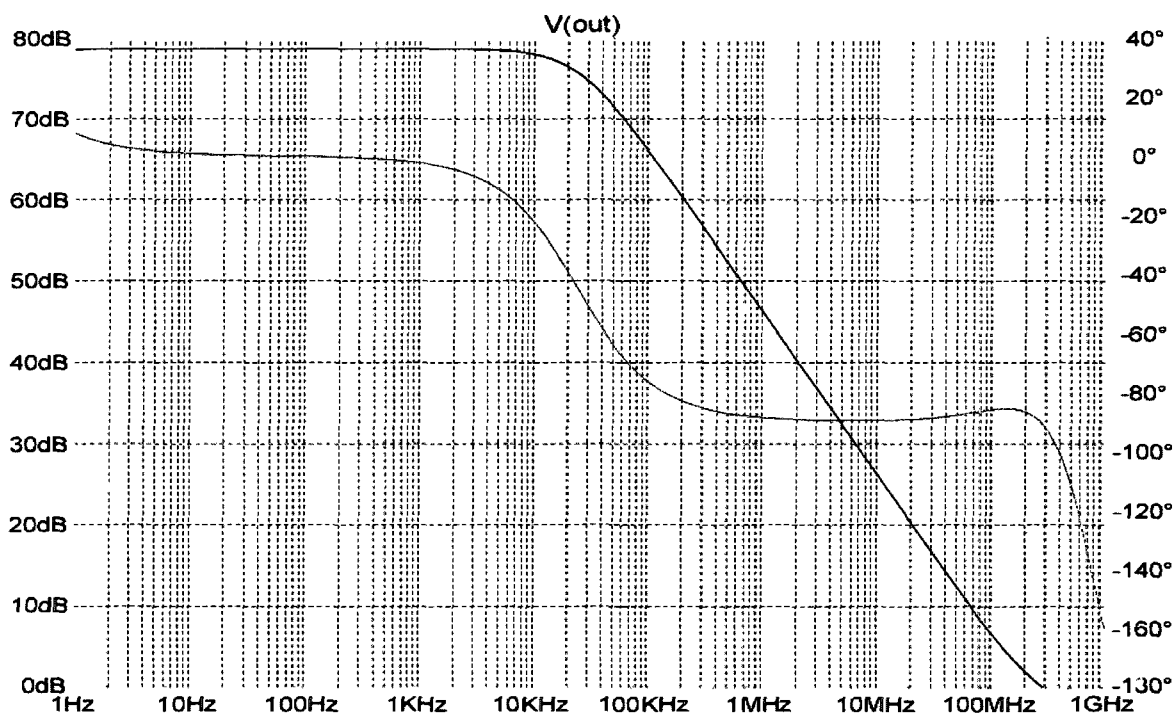


Figure 5.37 Open loop gain and phase response, 500 fF capacitor.

This graph gives information about the type of gain the amplifier will produce over a large range of frequencies. The open loop gain of the amplifier is about 78 dB; with the gain plotted over a large frequency, we can also determine the 3 dB point of the amplifier, which is 28 kHz. The graph also shows the gain bandwidth product of the amplifier, which is 281 MHz. The gain bandwidth product is the maximum frequency the amplifier can amplify with a gain of at least one. The phase response is also plotted on the graph. The phase margin of the amplifier shows the stability of the amplifier. The phase margin is determined by adding the phase response of the amplifier at its maximum frequency (281 MHz) to 180°. The phase margin of amplifier in Figure 5.37 is 89°. Any phase margin above 45° is considered stable. Figure 5.38 shows the open loop gain and phase response of the amplifier using a 250 fF compensation capacitor.

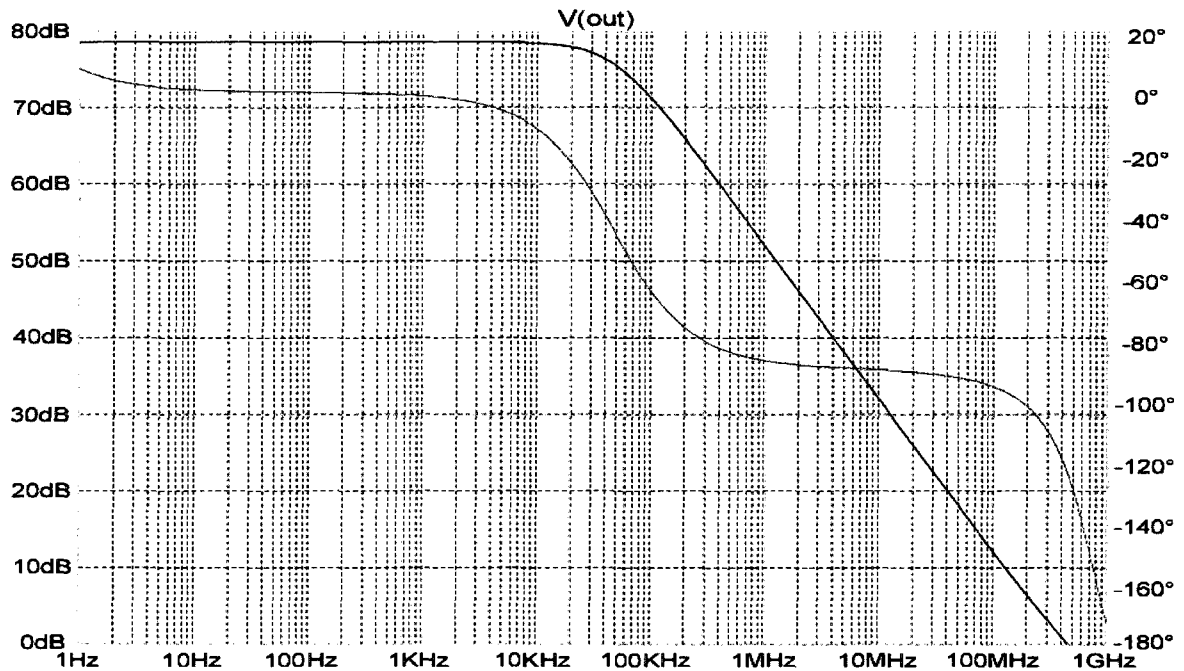


Figure 5.38 Open loop gain and phase response, 250 fF capacitor.

This simulation shows the same open loop gain for 78 dB, but the change in capacitor size has affected other aspects of the amplifier. The 3 dB of the amplifier has increased to 53 kHz with a gain bandwidth product of 446 MHz. This increase comes at the cost of stability; the phase margin of this amplifier is reduced to 57° , which is much closer to the 45° limit. In practical applications is it better to try and keep the phase margin above 60° .

Another important simulation when designing an amplifier is the step response of that amplifier, which is how well the amplifier's output follows the input with a 1 volt step input with a unity gain. Figure 5.39 shows the step response of the amplifier with the 500 fF compensation capacitor.

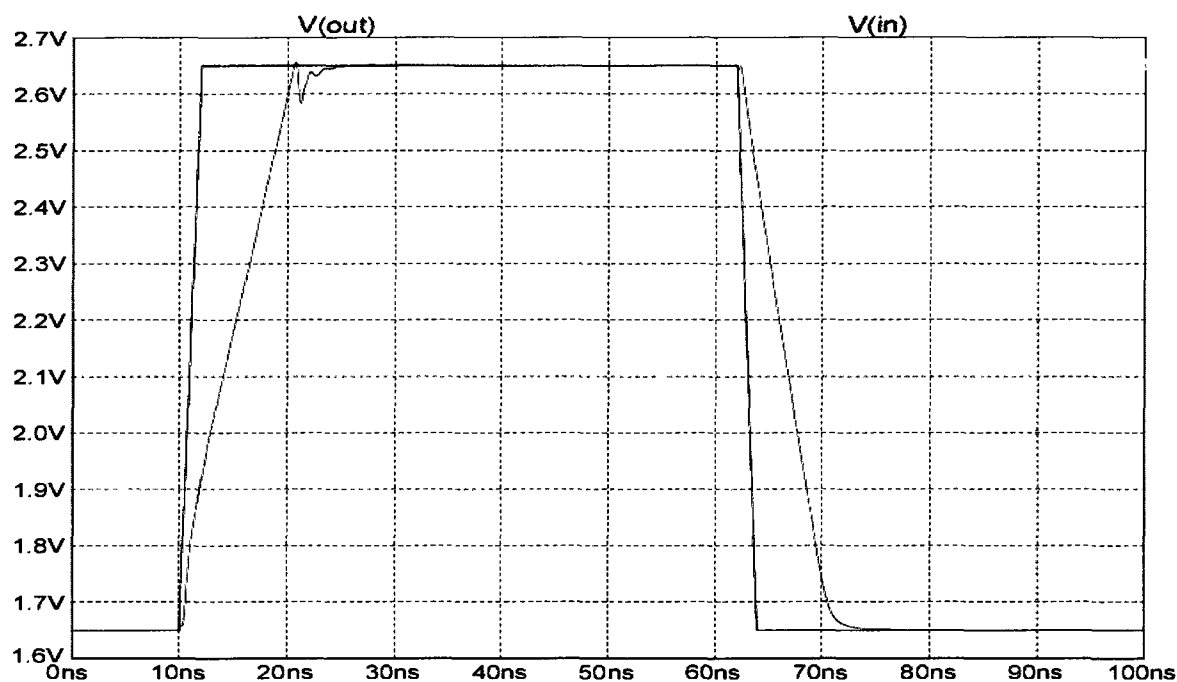


Figure 5.39 Step response, 500 fF capacitor.

The two factors that are found from the step response are the slew rate and the settling time of the amplifier. The slew rate of the amplifier is how fast the amplifier can follow the input step response. The slew rate is calculated from Equation 5.18:

$$SR = \frac{dV_{out}}{dt} . \quad (5.18)$$

Using this equation, the slew rate of the amplifier was determined to be 105 V/ μ s. The settling time of the amplifier is how fast the final value of the output comes within 2% of the input signal. The settling time of the amplifier was found to be 10 ns. Figure 5.40 shows the step response of the amplifier with a 250 fF compensation capacitor. For this amplifier we can see that using a smaller capacitor increases the speed of the amplifier. The slew rate for this amplifier was calculated to be 182 V/ μ s and had a settling time of 7 ns.

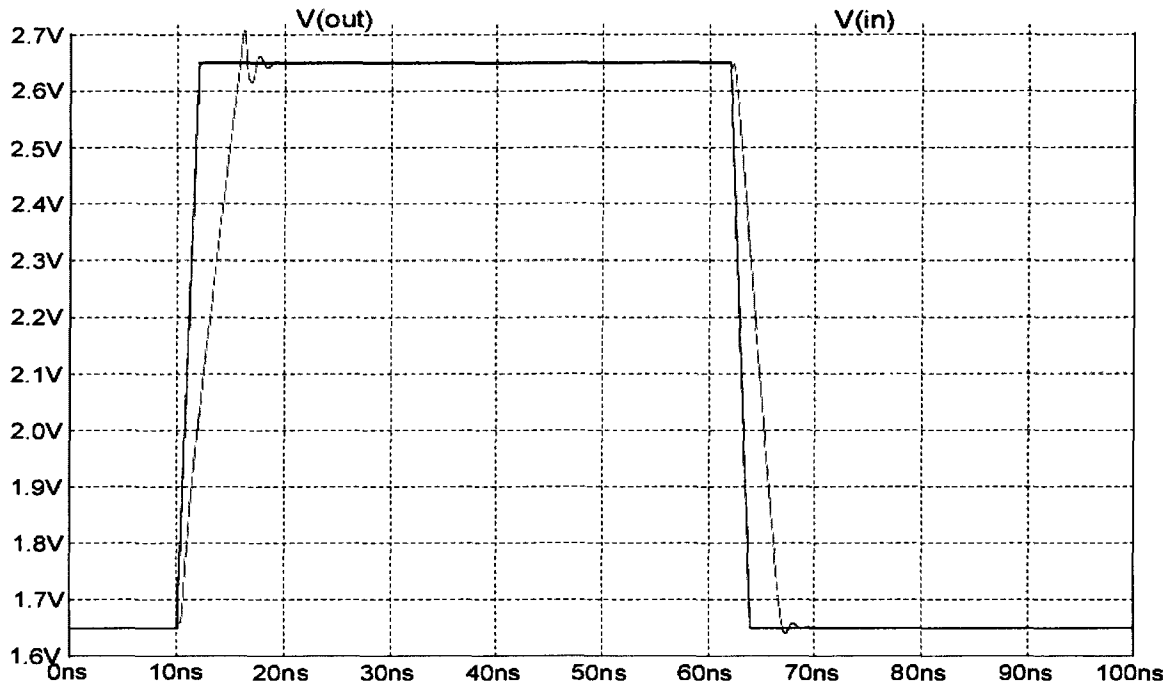


Figure 5.40 Step response, 250 fF capacitor.

There are a number of other simulations that need to be run to determine how well the design will handle noise and large signals. For these simulations, the results are not affected by the compensation capacitor size, and both amplifiers will have the same results. The common mode rejection ratio of an amplifier is a way to test how well an amplifier rejects a common noise signal on both inputs. The common mode rejection ratio for the amplifiers was determined to be 126 dB. Another test was conducted to find the common mode range of the amplifiers. The common mode range is used to determine for what voltages the input will match the output of the amplifier. This can be used to determine how close the amplifier can amplify the signal to the supply rails. In the case of my amplifier, the supply rails are 0 and 3.3 volts. The common mode range for the amplifiers was determined to be 0.3 to 3.2 volts.

The final simulation done for the amplifier was the noise performance. For an op-amp, the input referred noise has the most contribution to the total noise of the amplifier. The range that the input referred noise is simulated is from 1 Hz to 10 Hz, where both white noise and flicker noise contribute to the signal. The total RMS noise of the amplifier is determined by integrating the noise over the 1 Hz to 10 Hz range. The total RMS noise for the amplifiers was calculated to be $185 \mu\text{V}$.

5.2.6 Comparator Simulation Results

Comparator simulations were done to test the performance of the comparator design. The positive input of the comparator was swept from 0 to 3.3 volts, while the negative input, which is the trigger voltage, is stepped in increments from 0.3 to 3 volts. This shows the input common mode range of the comparator. Figure 5.41 shows one test graph for the comparator. The trigger increment for this graph is 200 mV.

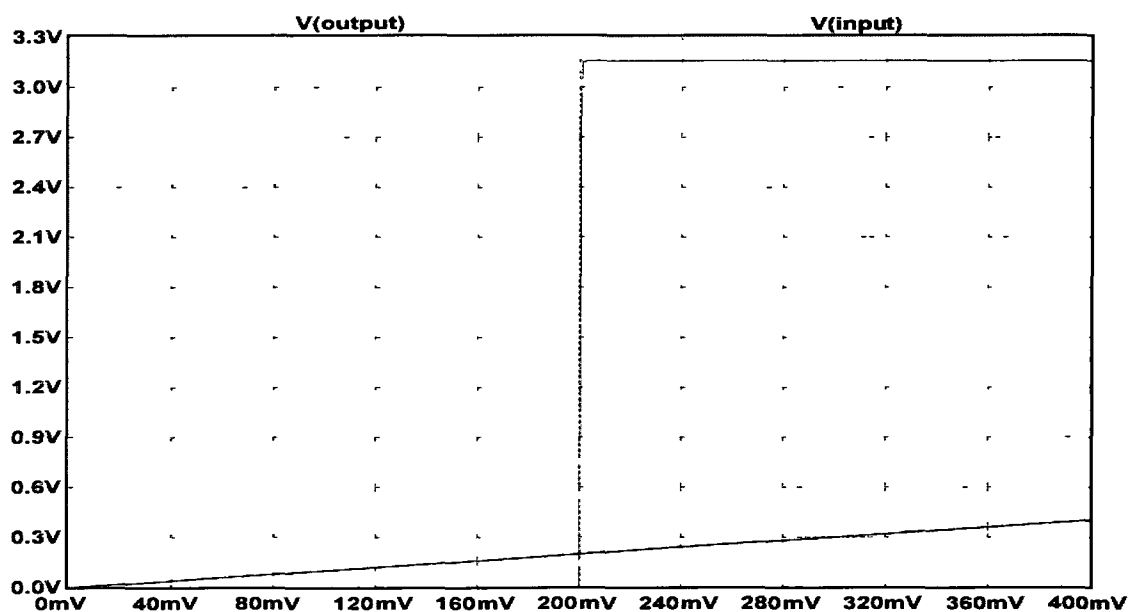


Figure 5.41 Comparator switching test at 200 mV.

The transient response to the comparator was also tested using sine waves with various frequencies. Figure 5.42 shows the transient response of the comparator using a 50 kHz sine wave.

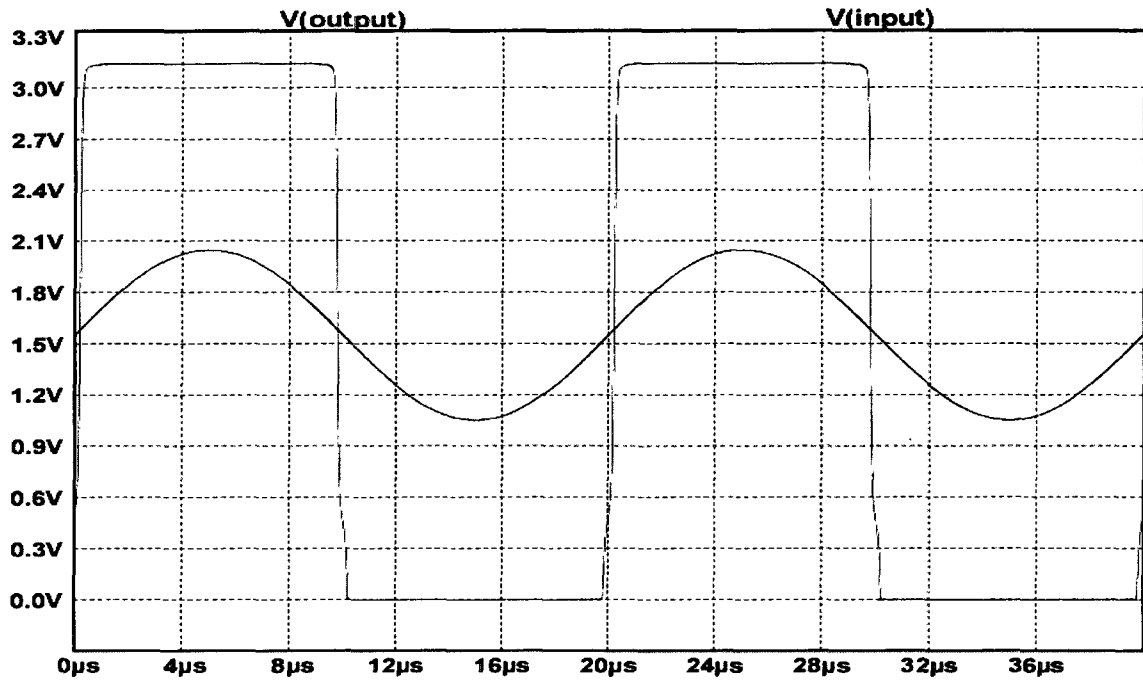


Figure 5.42 Transient response of the comparator.

5.3 Integrated Circuit Layout Design

Once the circuits are designed in SPICE and simulated, the next step is to layout the designs for the chip die. When creating a circuit layout, the designer needs to arrange the components to optimize matching of similar devices, packing, and ease of creating interconnections [62]. Once the components are connected together into a cell, the cells can then be connected to form the complete circuit die. The designer must also follow specific design rules for the technology being used. The design rules are in place to insure that the processing step of making the chip does not affect the device operation; this is done by creating limits on the spacing between circuit elements that are in the

same layer. It also limits the smallest width depending on the technology used. For my design I used the TSMC 0.35 micron process. This process has a minimum transistor size gate of 0.35 microns.

5.3.1 Operational Amplifier Layout

When creating a layout of a device, there are two important aspects to consider, matching components and minimizing cell area. Looking at the schematic for the op-amp in Figure 5.28, we can see that most of the components are matched in pairs. When laying out components that are similar to each other, the designer should place these parts close together so that if the manufacturing process has variations, the transistors will both be affected. Two common methods to minimize the area of the cell are laying out the transistors so they can share source or drain connections when possible and reducing transistors with large widths to multiple short width transistors connected in parallel. The layout of the designed op-amp is shown in Figure 5.43.

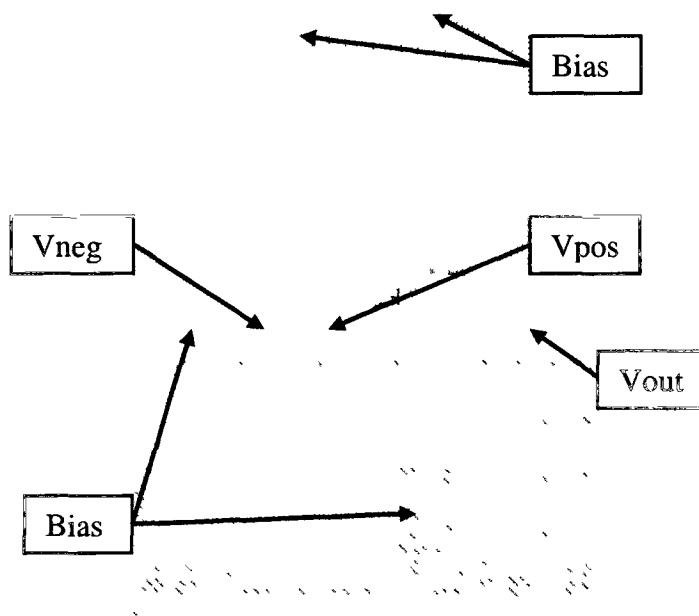


Figure 5.43 Operational amplifier layout.

5.3.2 Comparator Layout

The comparator was laid out using methods similar to the operational amplifier. The matching of the decision circuit transistors is not a large concern for this design. By not focusing on exact component layout matching, the manufacturing process will create a slight hysteresis in the circuit, which will help eliminate some false triggering from noise. The layout of the designed comparator is shown in Figure 5.44.

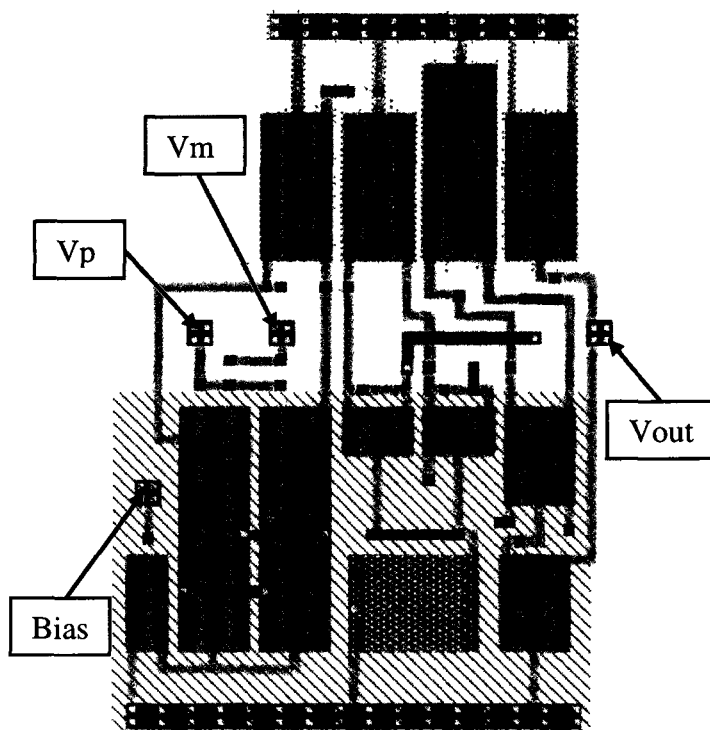


Figure 5.44 Comparator layout.

5.3.3 Passive Component Layout

To create a detection package with the smallest footprint possible, the passive components also must be constructed on the chip die. The design will need to use both capacitors and resistors on chip. There are various types of capacitors that can be created in a CMOS process. Capacitors can be created between the active region layer and poly-

silicon layer, between two poly-silicon layers if a second layer is available, or between poly-silicon and the metal layers. For this design, the TSMC process has a second poly-silicon layer which allows for poly-poly capacitors. This type of capacitor is ideal because this type gives the most capacitance per area than any other type available. The TSMC 0.35 process can create a poly-poly capacitor with a capacitance of $850 \text{ aF}/\mu\text{m}^2$. Instead of creating a single large capacitor, smaller capacitors were created and connected in parallel to achieve the correct capacitance for a component. Figure 5.45 shows both capacitors that were used in the design, 500 fF and 250 fF.

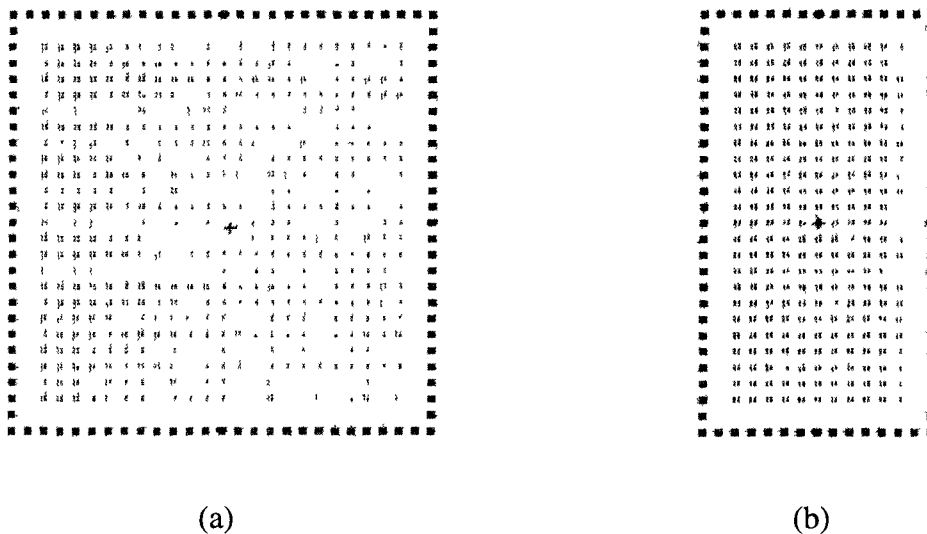


Figure 5.45 Capacitor layout for 500 fF(a) and 250 fF(b) capacitors

Resistors can be created on chip by using the sheet resistance of various layers in the manufacturing process. The two types of resistors that are used are either a poly-silicon or an n-well resistor. I chose to use poly-silicon resistors for my design. Resistors are constructed in the layout by using strips of poly-silicon. The MOSIS data sheet for the TSMC 0.35 micron process has a sheet resistance for poly-silicon over the n-well of

995 ohms/square and a contact resistance of 7.2 ohms. The sheet resistance can be used to calculate resistor sizes using Equation 5.19.

$$R = R_{sheet} \left(\frac{L}{W} \right), \quad (5.19)$$

where L and W are the length and width of the strip of material being used for the resistor. When creating a large resistor, you can either bend the material into a serpentine shape or connect multiple small resistors in series with metal layers. For my design, I chose to use multiple small resistors so I could use one resistor design to create many different size resistors. Figure 5.46 shows a layout of a 50 kilo-ohm resistor constructed from 10 kilo-ohm segments.

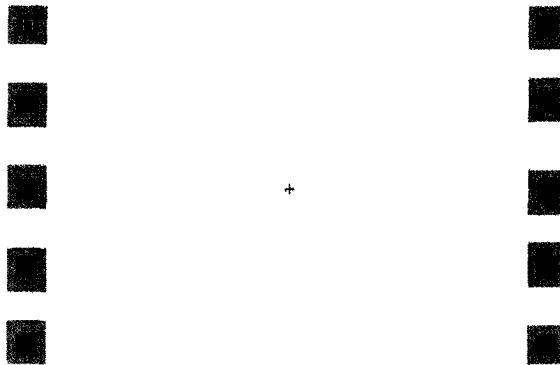


Figure 5.46 50 kilo-ohm resistor layout

5.3.4 Pads and Pad Frame

Once the chip components are complete, they must be put inside of a pad frame with pads to connect the circuit to the outside world. The inside chip die in a package is very sensitive to static charge and can be damaged if directly touched. To avoid damaging the chip, electrostatic discharge protection pads are required. The pad protects the inner chip core as well as buffers the signals entering and exiting the chip. The pad

uses two large diode connected transistors, one PMOS and one NMOS, to absorb any electrostatic discharge that can occur from a person touching and handling the chip. The number of pads needed for a design affects the overall size of the chip. The more pads that are needed, the more area the chip will require. My design uses pre-designed pads that are supplied by MOSIS for the TSMC 0.35 micron process. The pads supplied have a width of 90 μm and a length of 300 μm . This gives a 25 pin chip with 5 pins per side and an inner chip area of 450 μm by 450 μm .

5.3.5 Chip Core

Once a pad frame is constructed, the individual cells for the other components can be placed inside of the frame. Constructing the components in their own cell gives the flexibility of moving parts around to optimize space usage and place cells that must be connected together near one another. Capacitors consume the most area on a chip, so the capacitor array was constructed first. After the capacitor array, the bias circuits were placed; one bias circuit powers three op-amps, and the second bias circuit powers two op-amps and one comparator. The resistors needed for the design were then inserted between and on the side of the op-amp cells where space was available. Since resistors are the smallest component with large resistors constructed using many smaller resistors, they are the most flexible for placement. Figure 5.47 shows the total circuit layout submitted to MOSIS for fabrication. Since the complete radiation circuit did not consume the entire inner chip area, additional test op-amps and a comparator were added before fabrication.

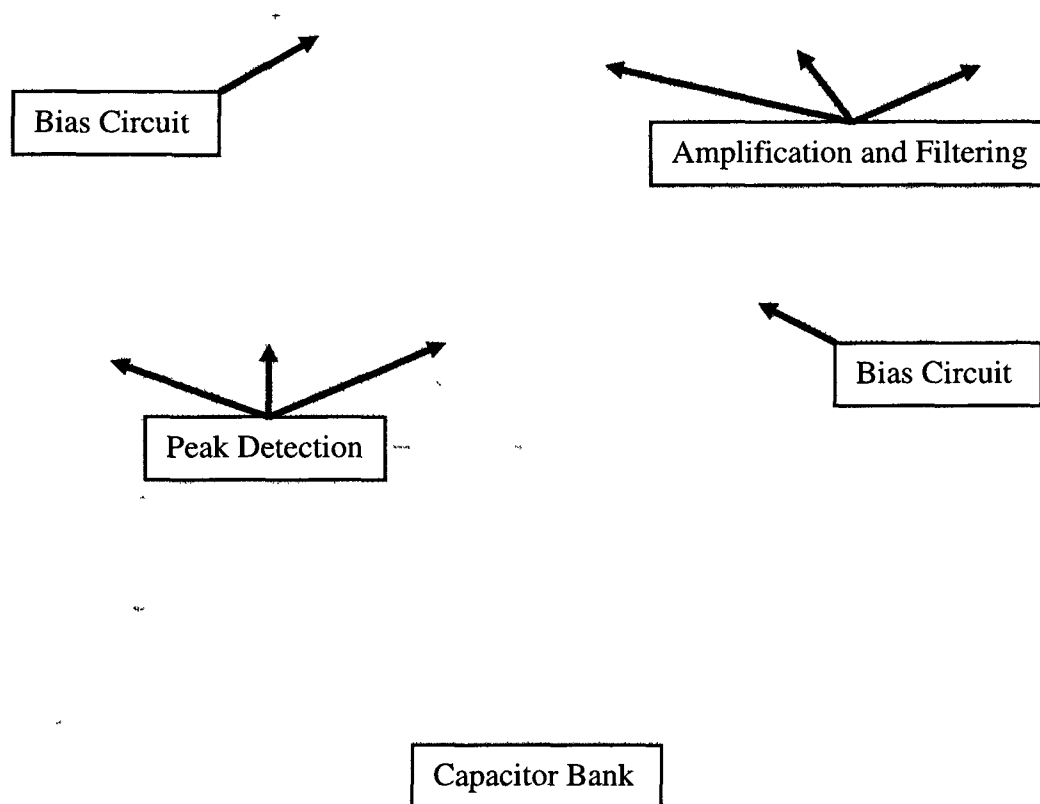


Figure 5.47 Layout of complete radiation detection circuitry.

5.4 Results and Improvements

Once the chip was returned from MOSIS, testing was done to the components. The fabricated chip had four separate circuits that needed to be tested. The radiation spectroscopy circuit was the main circuit with the most components; the other three

circuits were test circuits. The three test circuits were placed on the chip in case the full radiation circuit did not work on the first try. The test circuits were two op-amp designs, one with a 500 fF compensation capacitor and one with a 250 fF capacitor. The third test circuit was a comparator.

The op-amps used in the main circuit design were built using 250 fF compensation capacitors because the simulations showed this op-amp has faster response compared to the 500 fF capacitor. When the main radiation circuit was tested, no output signals could be recorded. The only type of signal on the output of the circuit was a noisy low frequency sine wave. Since the main circuit did not work, the next step was to move on to the test circuits to determine if there was a problem with the op-amps or some other problem that could possibly be from layout techniques.

5.4.1 Operational Amplifier Testing

The op-amps were tested to see what type of gain could be achieved with various sine waves, and the step responses of the amplifiers were also tested. The op-amps that were constructed with the 250 fF compensation capacitors were the first tested since they were used in the main design. Unfortunately, the test op-amps also would not output any type of usable signal; they would show some signs of amplification but would not consistently have the same type of output. Figure 5.48 shows the inverted step response of one 250 fF op-amp. This result was only achievable in one particular op-amp and could not be reproduced with any other 250 fF op-amp. The blue wave form is the input step signal, and the yellow is the corresponding output form for a unity gain inverting amplifier configuration.

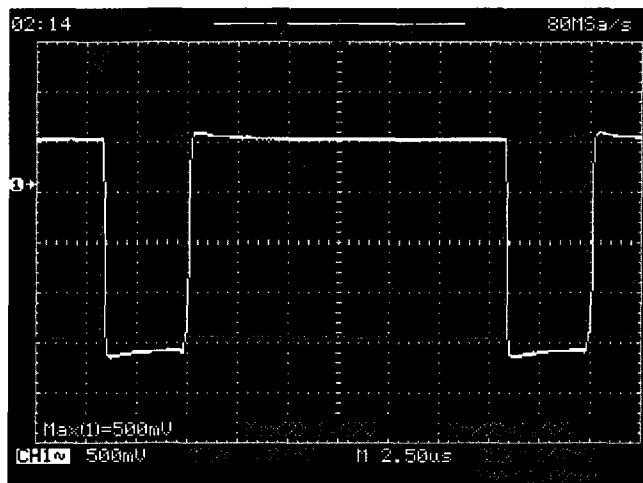


Figure 5.48 Inverted step response of one particular 250 fF amplifier.

From this type of result, I believe that the amplifiers with 250 fF compensation capacitor were an unstable design. The amplifier initial design was simulated, and it was determined that the design was close to being marginally stable. Since the manufacturing process is not ideal, I believe the fabricated amplifiers were in the unstable range.

The op-amps with the 500 fF compensation capacitors had much better results than the other test op-amp. The 500 fF op-amps were able to both show some signal amplification and the ability to follow a step input signal. Figure 5.49 shows the op-amp amplifying a 50 kHz sine wave with an input voltage of 1 volt peak to peak. The amplifier was constructed for non-inverting amplification with a gain of two.

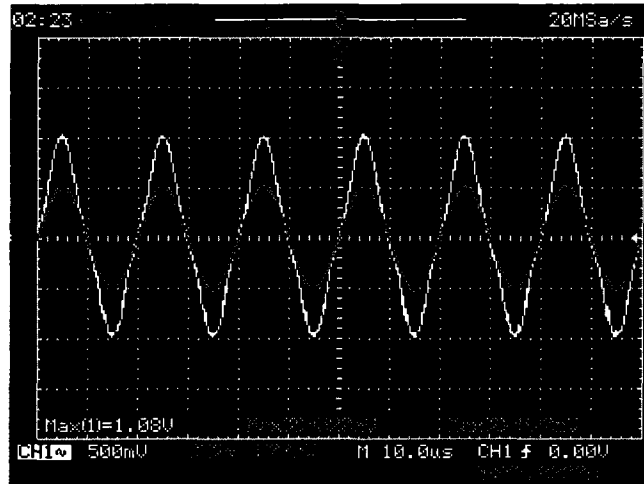


Figure 5.49 Non-inverted amplification of the 500 fF amplifier with a gain of two.

The amplifiers with the 500 fF capacitors show that they can successfully amplify the input signal. The inverting amplification of the amplifier was also tested. Using the same sine wave input, the inverting amplification output is shown in Figure 5.50.

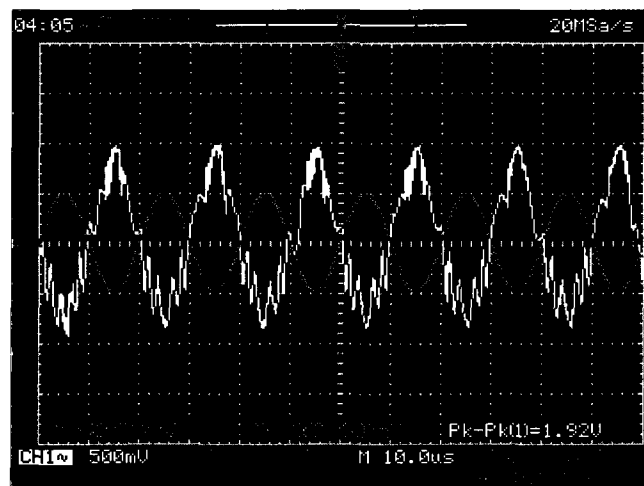


Figure 5.50 Inverting amplification of the 500 fF amplifier.

The inverting amplification shows a lot more noise in the output signal compared to the non-inverting amplification. I believe this comes from inadequate transistor matching.

The step response of the amplifier was also tested. An input step signal of 100 kHz was used. Figure 5.51 shows the output of the amplifier (yellow) with the step signal input (blue).

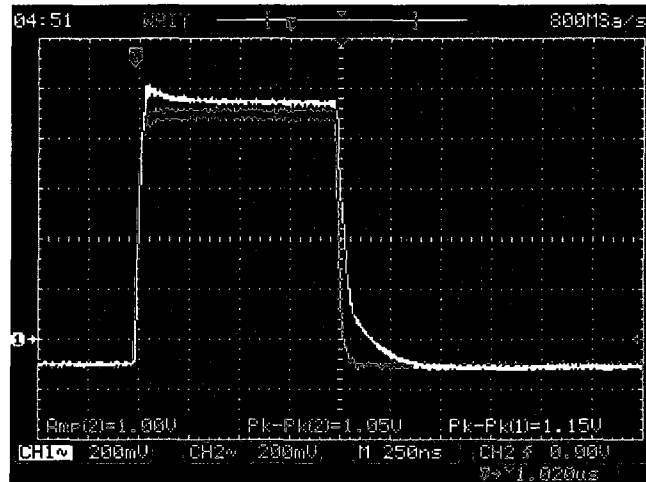


Figure 5.51 Step response of the 500 fF amplifier.

The amplifier shows the ability to follow the step response reasonably well. The amplifier has a calculated settling time of 140 ns with a slew rate of 22 V/μs. The amplifier does have an offset from the input signal of 50 mV. I believe this is another matching issue.

The next step was to determine the limitations of the amplifier so that the working design can be improved. The next test was to increase the amplifier gain to see output voltage limitations of the design. Ideal amplifiers would be able to output a signal up to the supply voltages; in this case the supply voltage is 3.3 and 0 volts. Figure 5.52 shows the amplifications of the same input 50 kHz sine wave used earlier but with a gain of three.

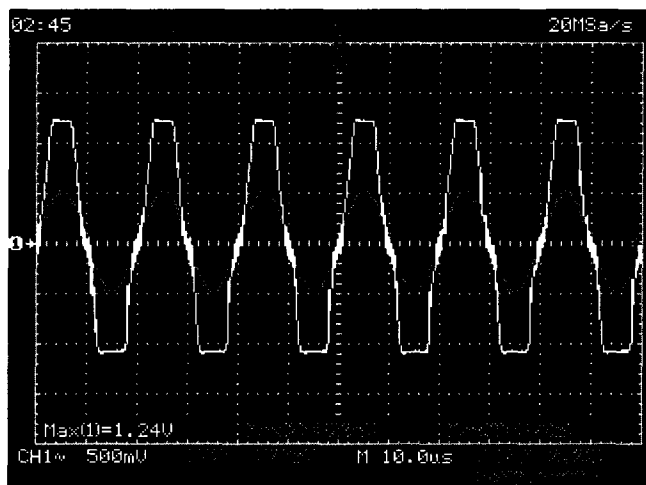


Figure 5.52 Testing the output limitations of the amplifier.

The output of the amplifier shows output limitation of the amplifier is 2.8 to 0.4 volts. This output range is much smaller than what was simulated. The simulated output range was 3.2 to 0.3 volts. I believe this issue can be resolved with better power calculations for the amplifiers and better sizing of the metal traces used to power the circuit.

5.4.2 Operational Amplifier Improvements

From the test results, I have determined two major improvements needed for the second MOSIS submission; better transistor matching and better power calculations. The current design used some transistor matching techniques, but other more complicated methods may be needed. Figure 5.53 shows a diagram of a common centroid layout of a transistor pair.

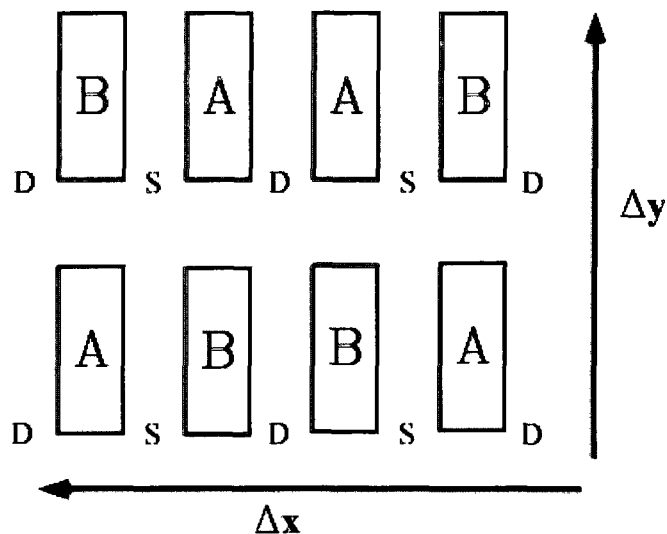


Figure 5.53 Common centroid layout of a transistor pair.

To layout a pair of transistors in a common centroid configuration, the transistors are divided into smaller transistors that are placed in the pattern seen in the figure and then connected in parallel. This configuration balances the two transistors so that no matter what type of process errors are introduced, both transistors will be affected evenly. Figure 5.54 shows the new layout of the op-amp focusing on transistor matching with the common centroid layout. The transistor sizing was also reconsidered and improved. The size changes are shown in Table 5.5.

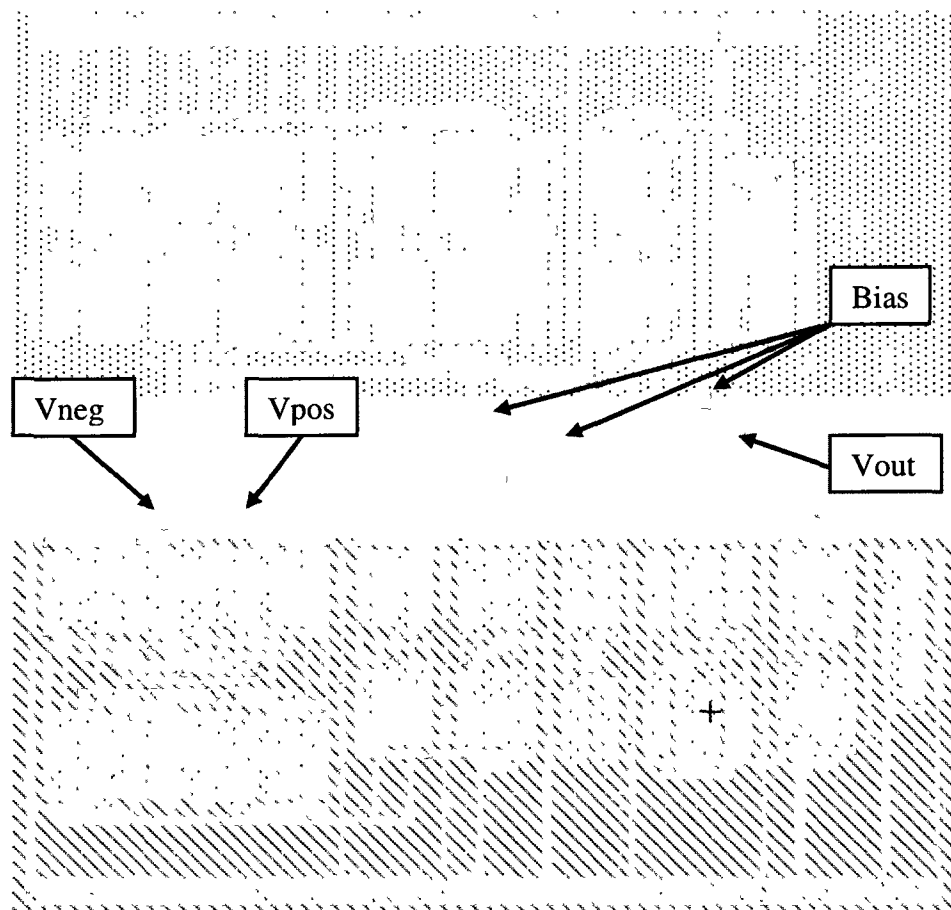


Figure 5.54 New op-amp layout with better transistor matching.

Table 5.5 New transistor sizes for the operational amplifier

Component	Model	Size	Component	Model	Size
M1	NMOS	350/1	M10	PMOS	88/1
M2	NMOS	350/1	M11	NMOS	44/1
M3	NMOS	175/1	M12	NMOS	44/1
M4	NMOS	175/1	M13	NMOS	88/1
M5	PMOS	350/1	M14	NMOS	88/1
M6	PMOS	350/1	M15	NMOS	88/1
M7	PMOS	175/1	M16	NMOS	88/1
M8	PMOS	175/1	M17	PMOS	175/1
M9	PMOS	88/1	M18	NMOS	88/1

The power that is supplied to the circuit is another concern for correct operation. If the traces that are connected between the power and ground supply pad and the actual circuit are under-sized, then these traces become resistors in the circuit (Figure 5.55).

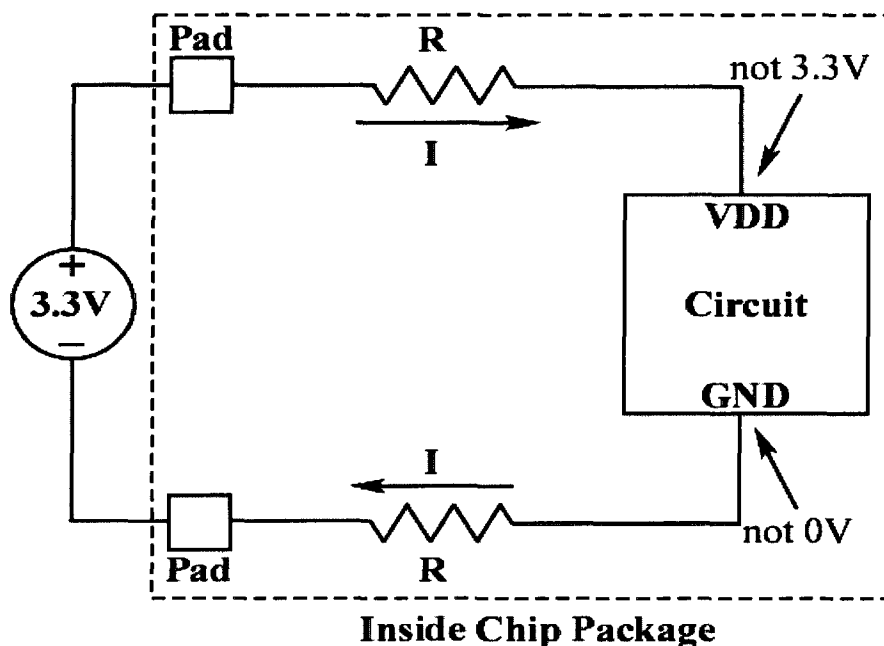


Figure 5.55 Under-sized power and ground traces become resistors in the circuit.

If the traces are too small for the amount of current that the chip is pulling from the supply, the resistance of the trace will cause some of the supply voltage to be lost over the distance of the trace. This problem is solved by increasing the width of the traces between the power and ground pad and the circuit. The resistance of the traces can be calculated the same way a poly-silicon resistor is calculated. This calculation can only be done after the circuit has been placed inside of the pad frame and the distance between the pad and the circuit is measured. Once the distance is measured, this is your resistor length for the calculation and your width is the variable parameter to reduce the resistance between the pad and circuit. The new amplifiers have been determined have a

max current draw of about 700 μA ; when a final package size is determined for the new amplifiers, this information will be used with the trace resistance calculations to determine the appropriate trace widths.

5.4.3 Comparator Testing and Improvements

A test comparator was also placed on the layout. A test comparator circuit was set up to see what type of switching speeds and hysteresis were in the fabricated comparator. Unfortunately, the test comparator could not generate any type of useable outputs. The output of the comparator would show some switching, but the output was always a very noisy signal. The signal noise was so high, no significant results could be recorded. For the second MOSIS submission I have decided the best course of action is to use part of the op-amp circuits that have been proven to work in the comparator circuit. It was discussed earlier that the comparator has two amplification stages and a decision circuit. The op-amp designs are two stage op-amps, and this design can be used with a comparator decision circuit. Figure 5.56 shows the new schematic for the comparator, and Table 5.6 shows the new transistor sizes.

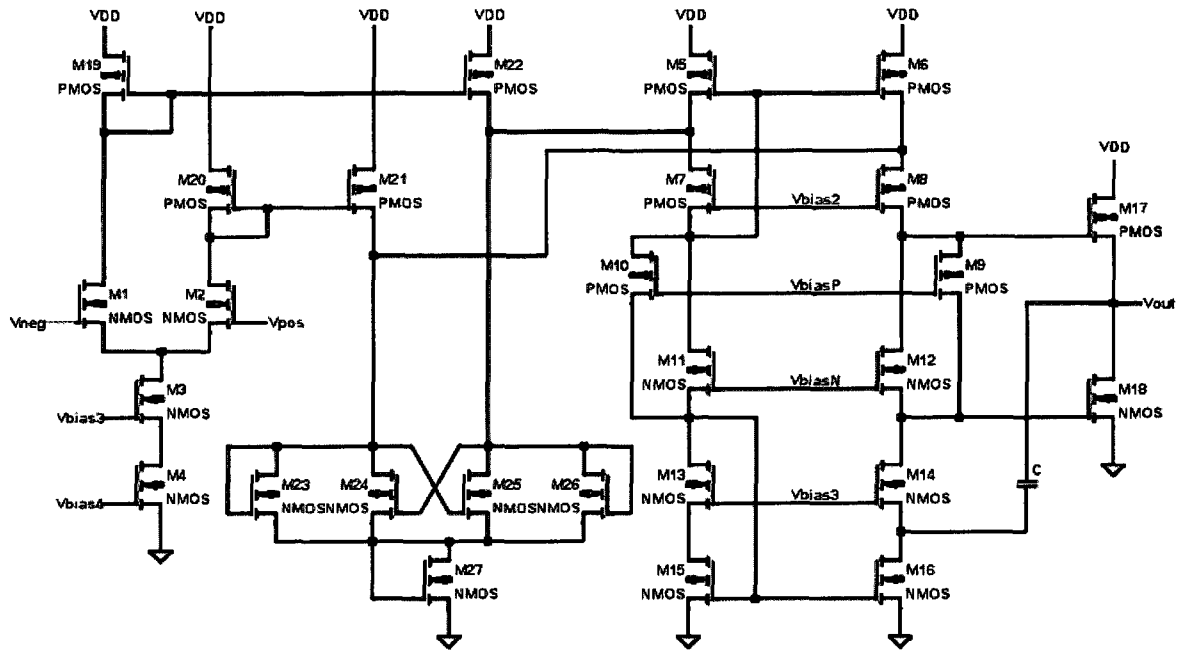


Figure 5.56 New comparator schematic.

Table 5.6 New transistor sizes for the comparator circuit

Component	Model	Size	Component	Model	Size
M1	NMOS	350/1	M15	NMOS	88/1
M2	NMOS	350/1	M16	NMOS	88/1
M3	NMOS	175/1	M17	PMOS	175/1
M4	NMOS	175/1	M18	NMOS	88/1
M5	PMOS	350/1	M19	PMOS	100/1
M6	PMOS	350/1	M20	PMOS	100/1
M7	PMOS	175/1	M21	PMOS	100/1
M8	PMOS	175/1	M22	PMOS	100/1
M9	PMOS	88/1	M23	NMOS	50/1
M10	PMOS	88/1	M24	NMOS	50/1
M11	NMOS	44/1	M25	NMOS	50/1
M12	NMOS	44/1	M26	NMOS	50/1
M13	NMOS	88/1	M27	NMOS	100/1
M14	NMOS	88/1			

Figure 5.57 shows the new comparator layout. This layout uses the same layout as the operational amplifier with the additional decision circuit transistors added to the outside of the cell.

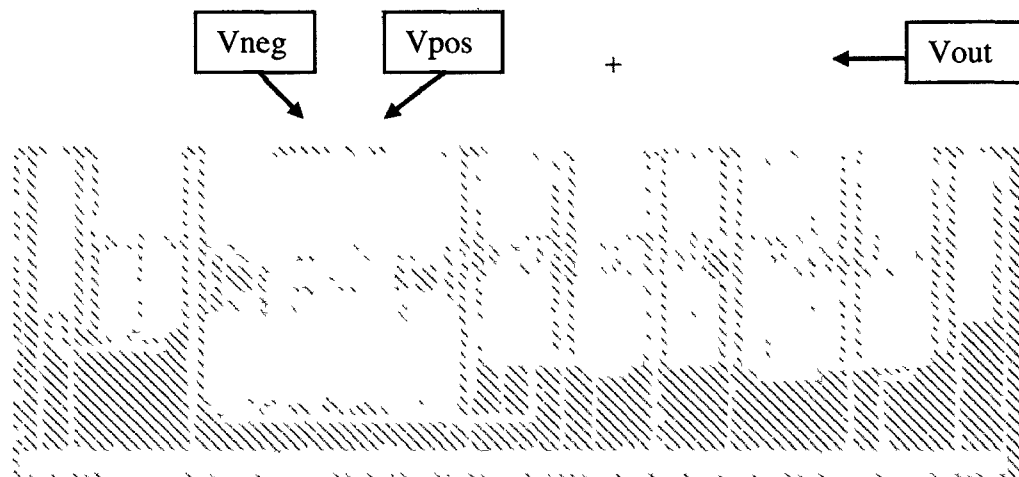


Figure 5.57 New comparator layout with transistor matching.

5.4.4 New Test Layout

The final layout for the second MOSIS run is shown in Figure 5.58. The layout consists of two test op-amp circuits with 250 fF compensation capacitors, two op-amp circuits with 500 fF compensation capacitors, and one test comparator. After the chip core package size is determined, the layout distance from the power and ground pins can be measured, and the trace sizes can be calculated and sized appropriately.

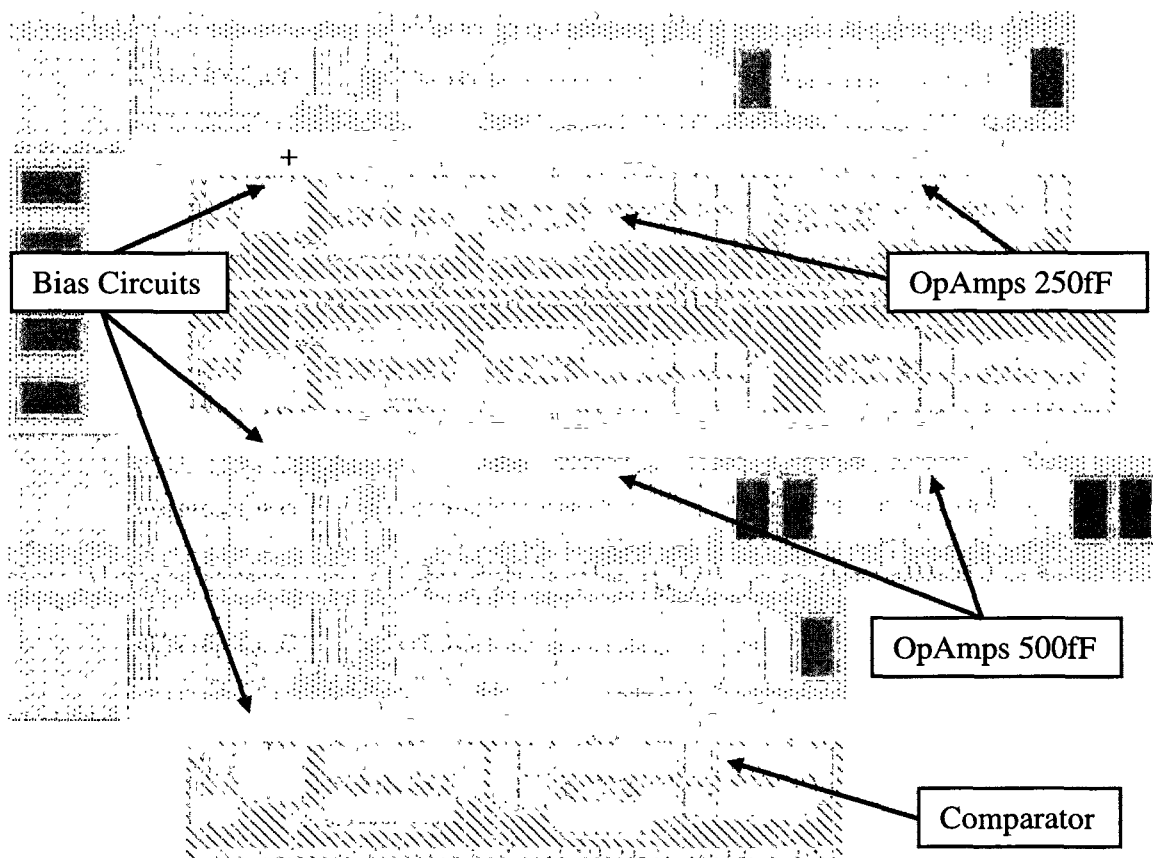


Figure 5.58 Test layout for second MOSIS fabrication run.

CHAPTER SIX

COMPLETING THE DETECTING PACKAGE: STACKED LAYER PHOTOMULTIPLIER TUBE

The widespread use of scintillators for radiation detection was not adopted until the invention of the photomultiplier tube. The scintillation of a radiation event produces a very low light output which is hard to see and count with the use of only a microscope and the human eye. PM tubes can convert the weak light output of only a few hundred photons produced by a scintillator into a corresponding electrical signal without the addition of a large amount of noise. PM tubes are able to convert light into photoelectrons and then amplify the photoelectrons into an electrical signal that can be used as an input current source. The PM tube design comes from two scientific discoveries, the observation of the photoelectric effect in the late 1800's of Heinrich Hertz and secondary electron emission phenomena discovered by Austin and Stark in 1902 [63]. With the advances of vacuum technology in the 1920's, the elements of the PM tubes were combined, leading to a multistage PM tube designed by RCA in 1936 [63].

PM tubes come in many different sizes depending on the application, but for small radiation detectors to be easily concealed, the PM tube design requires further reduction in size. There is also the requirement that the device be tailored to the dimensions of the application and not be limited by the commercially available devices.

There is also a need to reduce the cost of manufacturing these devices. If a large array of detectors is required for an application, the cost of the PM tube is the highest priced component of the detector, limiting the number of detectors that can be implemented. The scintillators and the circuitry for the detector are inexpensive to produce on a large scale. By creating a process for batch production and simple assembly of the PM tube component, we can reduce this cost, bringing the overall cost per detector down.

Others have tried different methods to reduce the overall size of a detector by using various technologies. One method that is being researched is to use what is called silicon photomultipliers, which are solid state photodiodes set up in an array. These devices are designed with an array of avalanche photodiodes that are biased a few volts away from their breakdown voltage and have quench resistor [64]. One or more of the diodes will then absorb the light photons and go into breakdown [64]. All of the diodes are connected to a common electrode, so if the silicon photomultiplier detects light photons, the charge is proportional to the energy of the photon [64]. The drawback of using a detector like this is the effect that radiation has on the silicon material. In high radiation flux areas, the neutrons and gammas are not fully absorbed by the scintillating medium and can damage the crystal structure of the silicon. This damage can reduce the effectiveness of the detector over time. Another device that has been researched is GEM (Gas Electron Multiplier) detectors. A photocathode is used to release a photoelectron from incident light particles. The photoelectron passes through several thin mesh type structures where avalanche amplification occurs under a high electric field [65]. The issue with this type of detector is the need to quench the created ions without limiting the detector's gain. A variation on the GEM detector is a micro-hole and strip-plate (MHSP)

detector. This detector is constructed with pairs of layers, one with GEM-like micro-holes and the other with micro-channel strips with the holes in line with the cathode of the strips, with anode strips running between them [66]. A voltage difference is between the top layer and the cathode strip, as well as between the cathode and anode; this results in high electric fields in the holes and around the anode strip [66]. The photoelectrons are then focused into the holes generating avalanche electrons, which are then extracted towards the anode strip [Maia]. The device produces an average gain of about 10^5 . The gain can become limited due to ion backflow into the device as the gain is increased.

6.1 Photomultiplier Tube Components

A photomultiplier tube is constructed of three main parts: a photocathode, dynode stages, and the anode (Figure 6.1).

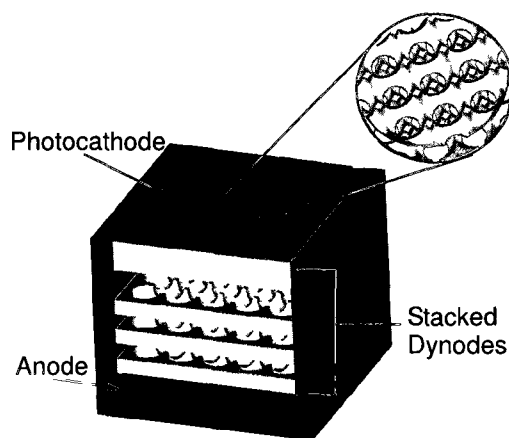


Figure 6.1 AutoCAD drawing of a stacked layer PM tube.

The photocathode is a photosensitive material that will emit photoelectrons after absorbing electromagnetic radiation emitted from the scintillator. The emitted photoelectrons are pulled toward the dynode stages by the electric field created inside of the tube. When the photoelectrons hit the dynode stages, more electrons are released

from secondary electron emission. The cascade of secondary electrons increases after each stage, resulting in amplification. The electrons are then absorbed by the anode and produce a measurable electric current.

6.1.1 Photocathode

The photocathode is a photosensitive material that produces photoelectrons due to the photoelectric effect. The photocathode is usually constructed from multiple materials, including alkali metals. This gives the cathode a very low work function, increasing the number of photoelectrons that can be produced from incident radiation. The material that is used in the cathode also will affect what wavelengths of light it is sensitive to.

Photocathodes can be designed to either be a semitransparent or opaque layer, depending on the type of detector that is used. The detector can be designed to operate using two different methods. They can be designed for transmission mode, where the incident light hits one side of the cathode and a photoelectron is released on the opposite side of the photocathode material, or they can be designed for reflection mode, where the photoelectron is released on the same side of the incident light photon. The window of the detector is made from borosilicate glass unless UV wavelengths are to be detected; then a UV transparent material is used.

Two important features of photocathodes are their quantum efficiency and spectral response. The quantum efficiency of the cathode is determined by the number of photoelectrons released by the cathode compared to the number of incident light photons. The incident photons transfer their energy to the electrons of the valence band of the photocathode, but not all of these electrons are emitted from the cathode [67]. Photons at

shorter wavelengths are higher energy than the longer wavelength photons and contribute more to the probability that photoelectrons will be emitted. This results in the maximum quantum efficiency of photocathode to occur at a wavelength slightly shorter than its peak spectral sensitivity. The spectral response of the photocathode is the range of wavelengths that the cathode is sensitive to. The long wavelength cutoff of the cathode is determined by its composition materials, while the short wavelength cutoff is typically determined not by the cathode, but by the wavelength cutoff of the PM tube window material.

Common types of cathode materials and their spectral response are shown in Figure 6.2.

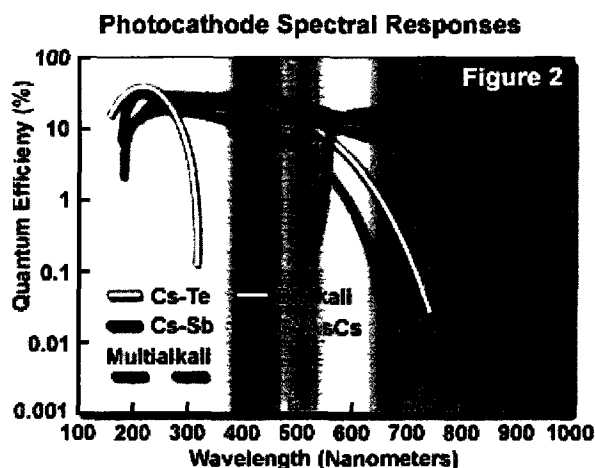


Figure 6.2 Spectral response of common types of photocathode materials [68].

Photocathodes composed of Cs-Te are not sensitive to wavelengths that are longer than 300 nm, therefore are not sensitive to solar radiation. This material has the same spectral response in both transmission and reflection modes. Since the UV range is of interest when using this type of cathode, synthetic silica or MgF_2 is used as a window material [67]. A photocathode made of Cs-Sb has a range from UV to the visible

spectrum and is used over the bialkali material when the PM tube will be used where light intensities will be high, allowing for a large current to flow in the cathode [67]. Bialkali (Sb-Rb-Cs, Sb-K-Cs) has about the same light spectrum range as the Cs-Sb but has a higher sensitivity and a lower dark current. This material combination is often used with scintillators because its sensitivity peaks at around the 450 nm range, which is around the same wavelength many common scintillators emit their photons. Multialkali (Sb-Na-K-Cs) allow for the broadest range of light absorption due to their combination of many types of materials.

6.1.2 Dynode Stages

The amplification stages of the PM tube are based off the secondary electron emission phenomenon. The photoelectrons that leave the photocathode strike the surface of the dynodes. Depending on the material of the dynode, the energy that is transferred from the photoelectron to the dynode will result in the release of more than one electron from the dynode surface. Amplification occurs by having a series of dynode stages, allowing for the secondary electrons from the first stage to strike the surface of the next stage producing more secondary electrons (Figure 6.3). As the number of dynode stages is increased, the overall gain of the PM tube is increased.

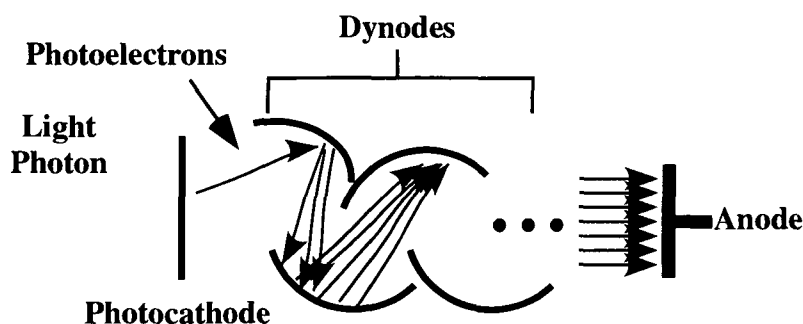


Figure 6.3 Dynode electron amplification.

There are different configurations that the dynodes of the PM tube can be constructed into. The configuration of the dynodes will affect the characteristics of the PM tube, such as the time response, linearity, and amplification efficiency. Hamamatsu's PM tube handbook covers various types of configurations that are currently in use. A popular dynode configuration for a fast response time and large gain with a relatively low operating voltage is the circular cage configuration (Figure 6.4a). This design also allows for the PM tube to be more compact than other configurations, which contributes to its fast response time. This type of PM tube typically has a side window for photon collection. A second configuration that displays good linearity with high collection efficiency is the box and grid (Figure 6.4b). The high collection efficiency of this design is due to the uniformity of the dynodes. The symmetry of the layout helps to confine the secondary electron emissions and guide them to the anode. A design that is similar to the box and grid configuration is the linear focused configuration (Figure 6.4c). This design has a high response time and good time resolution. This type also has excellent pulse linearity when compared to other designs. A fourth configuration is the metal channel type (Figure 6.4d). This configuration is micro-machined layers that are stacked together. This type of layout has a fast response time and has a stable gain, even in the presence of a high magnetic field, due to the ability to stack the layers tightly together. At the end of the dynode stages, an anode collects the electrons and produces an electric current. The anode of the PM tube is made of copper or another highly conductive material for maximum electron absorption.

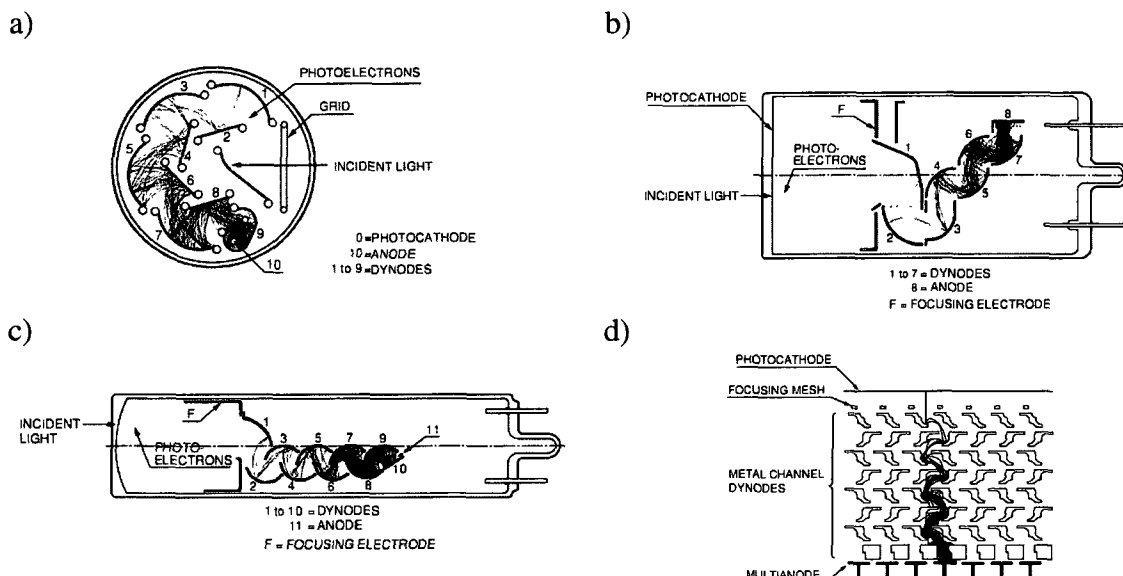


Figure 6.4 Photomultiplier tube dynode configurations [67].

6.2 Design

The design of the dynode layers came from the need to create a PM tube that is small and cheap to produce. To create a sensor package that can be cheaply mass produced, all elements of the device need to be easy to make at low cost. Stainless steel powder was chosen to be the material of the dynodes since it is easy to cast into different shapes. The dynodes were also designed to be stacked together so that they do not need to be attached to a substrate. The anode is made from a strip of copper that has the same dimensions of dynodes. To create the proper electric field in the device to guide the electrons to the anode, a voltage divider circuit is used to power the dynodes.

6.2.1 Dynodes and Anode

The dynode structure of the device was chosen to be stackable layers that are separated by an insulator around the edges of the layers. The stackable design was picked because it would remove the need to align the angle of each stage. The holes in the top layer align with the peaks of the bottom layers by simply stacking the piece. The

dynode material is sintered stainless steel parts; the casting of stainless steel parts is cheaper than having to machine each piece individually from stainless steel stock. Injection molding metal parts is the most effective way of producing pieces at low cost [69]. The finished stainless steel parts are a porous material and do not conduct charge well. This is a desired property in the material; since the parts do not conduct well, the electrons from amplification will not travel into the voltage divider circuit. The anode of the device was made from copper since it must have a high conduction of electrons to absorb the electron avalanche from amplification.

The dynode layers were first designed using AutoCAD software. The first stack layer design is shown in Figure 6.5. The design uses two different layers that will alternate in the stack; this allows for the bottom of the wells on the top layer to line up with the peaks in the bottom layer.

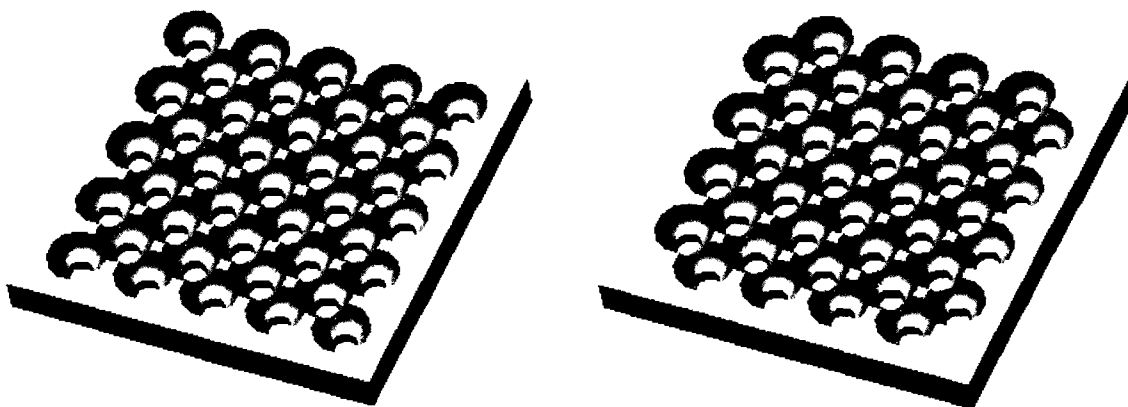


Figure 6.5 First stack layer design; layers are alternated as they are stacked.

This design allows for the layers to be squares that could be stacked in any orientation and still have the wells and peaks of the layers align. In making this design,

the problem arose that the initial dynodes did not always cast perfectly because the very small peaks did not have much structural support.

A new design was created that allowed for the peaks between the wells to have a larger support area (Figure 6.6). The well sizes were also increased for ease of fabrication for initial testing.

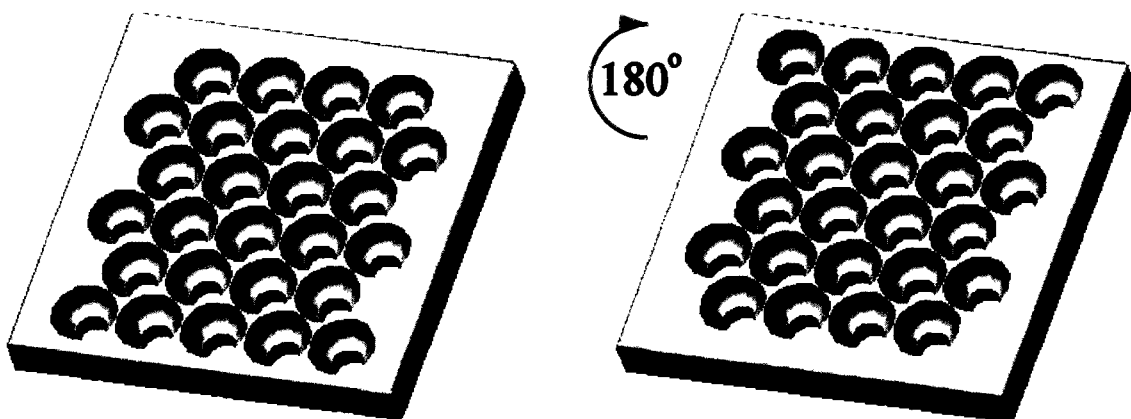


Figure 6.6 Second stack layer design; only a single layer is needed, requiring each layer to be rotated 180° as they are stacked.

The new design was changed to a slightly rectangular dynode shape and allows all the layers to be cast from the same mold. The wells of the top layer line up with the peaks of the lower layer by the placement of the layers. Each layer is rotated 180 degrees relative to the layer above it.

6.2.2 Voltage Divider

A voltage divider network is needed to properly bias each of the dynode stages. The divider network biases each dynode stage at a more positive voltage than the last stage to attract the electrons through the multiplying stages. The voltage divider circuit consist of a set of 330 k-ohm resistors and three 10 nF capacitors. The circuit was laid out in EagleCAD and fabricated on a PCB board. The high voltage supply and the total

equivalent resistance of the network are used to determine the current in voltage divider circuit. The current in the divider network is used to keep the voltage on each dynode layer constant and not allow the generated current of the PM tube amplification to change the total current in the divider network. A constant current on the dynodes will result in a constant gain in the PM tube. Since the generated current is at its highest on the last few stages of amplification before the anode, capacitors are used to help stabilize the current in these stages. A schematic diagram of the voltage divider network is shown in Figure 6.7.

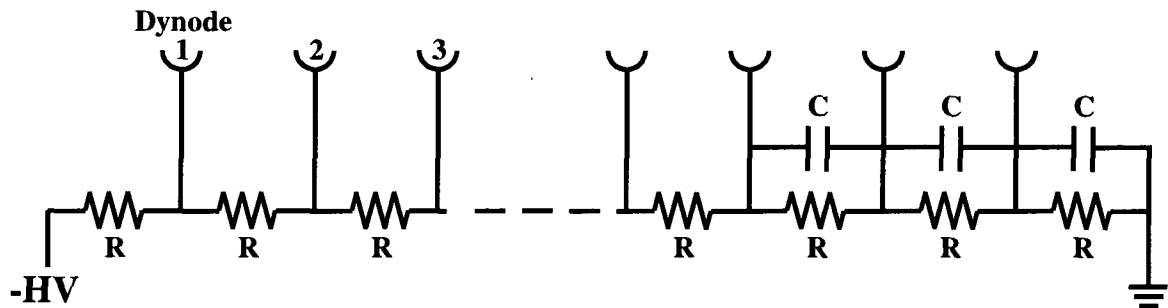


Figure 6.7 Schematic diagram of the voltage divider circuit.

6.3 Fabrication

The goal of the fabrication process was to create a device that is easy to mass produce. To have a device that can be mass produced, the dynodes are made from a master mold. The master mold is made from Teflon stock. PDMS is then used to make a reverse mold of the master. The dynodes are made using a combination of stainless steel powder and binder poured and compressed into the reverse mold. Once the binder hardens, the green dynodes can be removed and placed inside of the furnace. Wires are then attached to the dynodes using epoxy to supply power to each layer. The anode was

constructed from a strip of copper foil and attached to the bottom of the dynode stack. A wire is soldered to the anode to monitor electron collection on an oscilloscope.

6.3.1 Dynode Layers

The master mold of the dynode layers was cut from Teflon stock using a Roland MDX-40 milling machine. The machine uses a .stl file of the AutoCAD part where the user then programs in the bit passes and the drilling points for the piece. The machine was programmed to mill the outline of the part and then use a drill bit to drill holes through the piece. A ball mill end bit was then used to drill all the wells into the piece. The dynodes are 1 mm thick with a well depth of 0.8 mm. The mold is released from the Teflon stock using a band saw. The master mold Teflon pieces are shown in Figure 6.8.

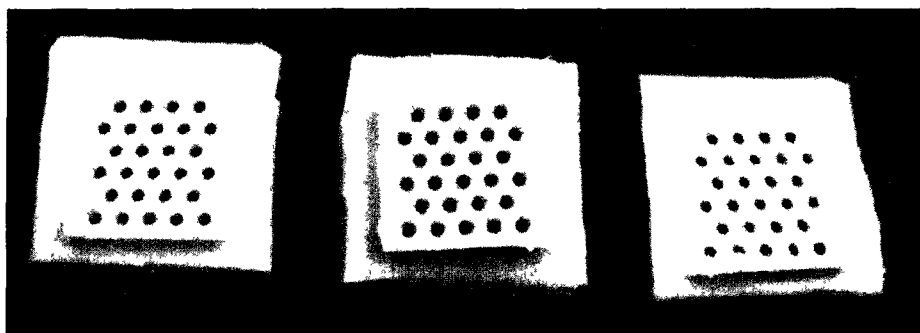


Figure 6.8 Master mold milled from Teflon stock.

The reverse disposable molds for the dynodes were made using Sylgard 184 silicone elastomer. The elastomer is a gel type resin with a separate activator. The resin is mixed 10:1 with the activator and poured into a Teflon container with two small shelves on the side to hold the master molds off the bottom of the container to prevent air bubbles from getting suspended in holes of the mold. The resin is then cured on a hot plate at 100 °C for one hour. Once the resin is cured, it can be pulled out of the Teflon container and the master molds removed from the reverse mold (Figure 6.9).

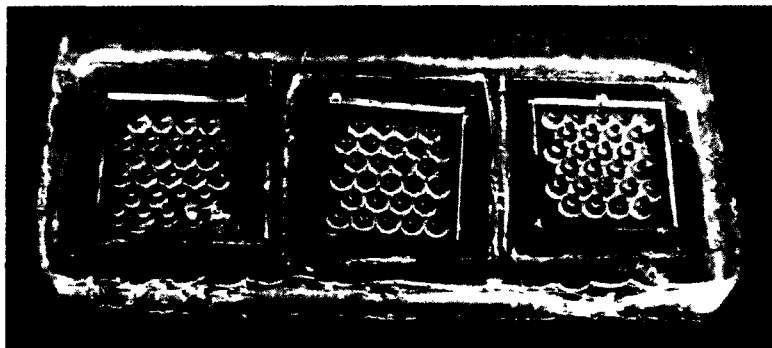


Figure 6.9 Reverse silicon mold of dynode master mold.

The green parts are cast from a mixture of stainless steel powder, Dow Duramax B-1000 binder, Dow Duramax D-3005 dispersant, and distilled water with a mixture ratio of 1:0.1:0.05:0.15, respectively. This mixture ratio was created based off a publication by M. Imbaby on “Characterization of Stainless Steel Microparts Fabricated by Soft Molding Techniques” [70]. The stainless steel powder has mesh size of 325, which means it has a maximum particle size of 44 μm . The stainless steel powder is first mixed with the dispersant and distilled water and placed inside a small vacuum chamber to remove the air bubbles. Once the air is removed, the binder is added to the mixture. The mixture is then poured into the silicone mold and compressed. The mixture is cured on a hot plate for an hour and then transferred to the furnace. The furnace heating cycle was based on a paper published by J. Zhou on “Rapid Pattern Base Powder Sintering Technique and Shrinkage Control” [71]. The cycle had to be adapted to work with the limitations of our lab furnace which heated more slowly than the one used by Zhou. The furnace was heated to 700 $^{\circ}\text{C}$ at a rate of 72 $^{\circ}\text{C}/\text{hr}$, and then held for 1.5 hours. The temperature was then increased to 1250 $^{\circ}\text{C}$ at a rate of 300 $^{\circ}\text{C}/\text{hr}$ and held for 1.5 hours. During the heating process, the binder is evaporated out of the casting, and the energy from the heat binds the atoms of the stainless steel particles together (Figure 6.10). The

completed pieces are slightly thicker than 1 mm, so the excess is removed with a stainless steel grinding disc.

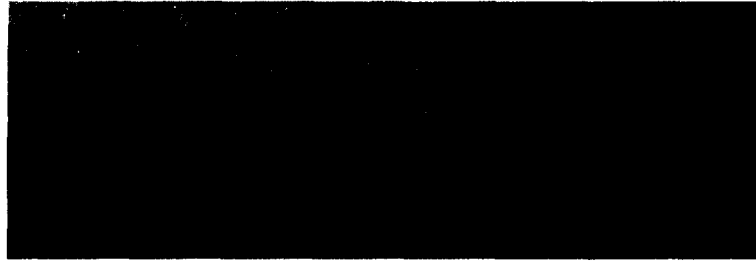


Figure 6.10 Dynode layers from cast stainless steel powder mixture.

Wires are attached to the completed dynodes using a conductive epoxy. The dynodes are then stacked together alternating their orientation 180 degrees for each piece with a small insulating layer between pieces (Figure 6.11). The wires from the dynodes are connected to two DB9 connectors for connecting the stack to the voltage circuit. The anode is attached to the bottom of the stack with a signal wire soldered to its base.

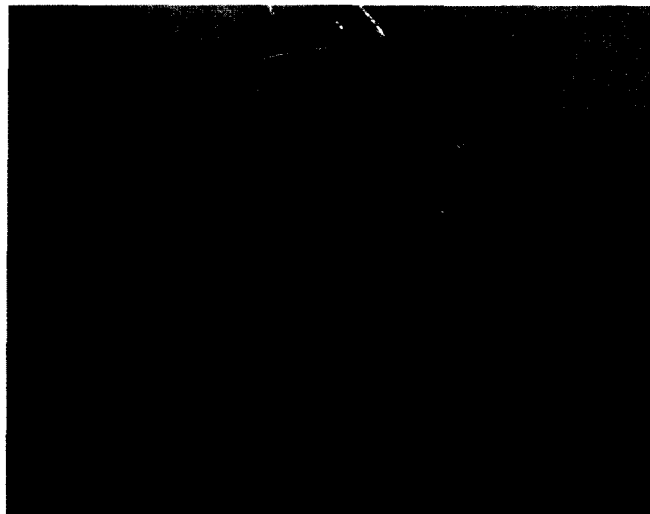


Figure 6.11 Eight layer dynode stack for testing.

6.3.2 Voltage Divider

The voltage divider circuit was created on a single sided PCB board. The board comes packaged with photoresist already spun onto the board. The mask for the board was printed onto a transparency slide using a laser printer. The photoresist on the board is exposed using a UV light box, and then the exposed resist is removed using a positive developer agent. The exposed copper is then etched using ferric chloride, and the through holes are drilled. The circuit components are soldered to the board with wires from each divider stage being connected to the DB9 connectors to supply voltage to the dynode stages (Figure 6.12).



Figure 6.12 Voltage divider circuit.

6.4 Testing

The equipment used for testing the dynode collection was a vacuum chamber with the Stanford high voltage power supply to power the dynodes in the chamber. An oscilloscope to record the current change at the anode and variac to control the voltage supplied to the tungsten filament. The dynodes and the voltage divider network were placed inside of the vacuum chamber. The tungsten filament was then placed inside of

the chamber in front of the dynode stack. The power connections for the filament and dynodes along with the ground connection are supplied to the parts inside the chamber with electrical connections on the outside of the chamber.

6.4.1 Testing Equipment

The vacuum chamber used for my experiments is equipped with a roughing pump to pull the initial vacuum of the chamber down to 100 mTorr and then uses a turbo pump to achieve a vacuum of about 10^{-4} Torr. The tungsten filament is supplied with an AC voltage from a wall outlet. The voltage supplied to the filament is passed through a variac to control the amount of voltage supplied to the filament, which controls the number of electrons emitted from the filament. The voltage divider network is supplied a DC voltage by the high voltage supply. The anode's current change was measured using an oscilloscope.

6.4.2 Testing Setup

The dynodes were stacked together with an insulating layer between each dynode to isolate them from one another. The dynodes and the anode were then attached to a strip of garalite board for testing. The dynodes were housed inside of a copper lined tube for the testing. The copper was used as an outer electrode and kept at the lowest potential to help confine the electrons emitted from the tungsten filament. The tungsten filament used was from a 60 W incandescent light bulb. The filament was housed inside of a glass cylinder to prevent the filament from arcing to the outside copper electrode. The cylinder had an open top to allow for the electrons to reach the dynode stack. The dynodes were powered by the voltage divider circuit with the most negative voltage being connected to the top dynode. Each proceeding dynode stage has a less negative voltage allowing for

the electrons to be directed towards the anode for collection. All electrical connections were provided by connectors on the side of the chamber. The device was tested at a pressure of about 1 mTorr.

6.5 Results and Discussion

The device was tested for electron collection using the tungsten filament. The electron emission from the tungsten filament was controlled using the variac between the filament and a 120 VAC wall outlet. The variac increased the voltage supplied to the filament in 10% increments. The dynodes were tested with filament voltages of 36 VAC, 48 VAC, 60 VAC and 72 VAC. The high voltage supply connected to the dynodes was operated at -500 VDC, -750 VDC, and -1000 VDC for each of the filament voltages. The dynodes stack was tested with eight dynode layers and six dynode layers to compare electron collection between different numbers of dynode stages. An eight layer dynode stack with an aluminum coating applied to the dynodes was also tested. This dynode stack was compared to the uncoated eight layer dynode stack to see how the addition of a secondary electron emission coating affected the gain of the dynode stack.

The oscilloscope was used to see small voltage changes from the anode. A voltage change at the anode of the device indicates more electrons are being collected from the dynodes. The number of electrons collected is affected by both the changes in the filament voltage and an increase in dynode voltage (Figure 6.13).

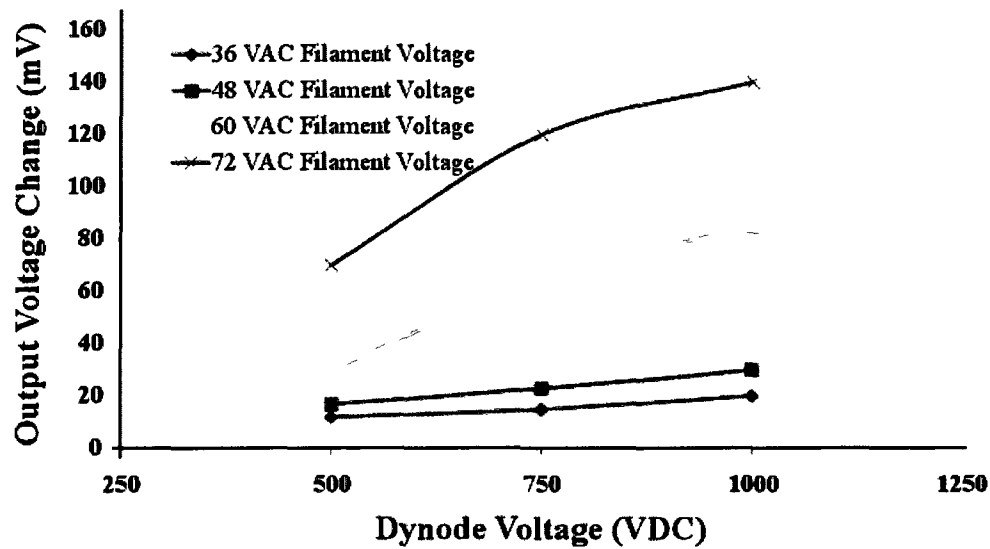


Figure 6.13 Voltage change versus dynode voltage for each filament voltage of the eight layer dynode stack.

At higher filament voltages, more electrons are emitted from the tungsten, and the device collects more electrons in proportion to the increase in supply voltage. As the DC voltage applied to the dynodes increases, the collection efficiency of the device is increased. The increase is due to the increased strength of the electric field created by the dynodes; a stronger electric field means more electrons are pulled to the anode of the device. The electric field that is set up inside of the device is important when creating a MEMS device that requires a vacuum to operate. Since a higher electric field increases the collection of electrons and the small size of the device means a shorter distance between cathode and anode, the vacuum inside of the completed device may not need to be as low as typical PM tubes.

The dynode stack was tested with both eight dynode layers stacked together and six dynode layers stacked together to compare the amount of electrons collected with fewer dynode stages (Figure 6.14). The fewer number of dynode stages used means the overall device can be smaller but also will affect the collection efficiency of the device.

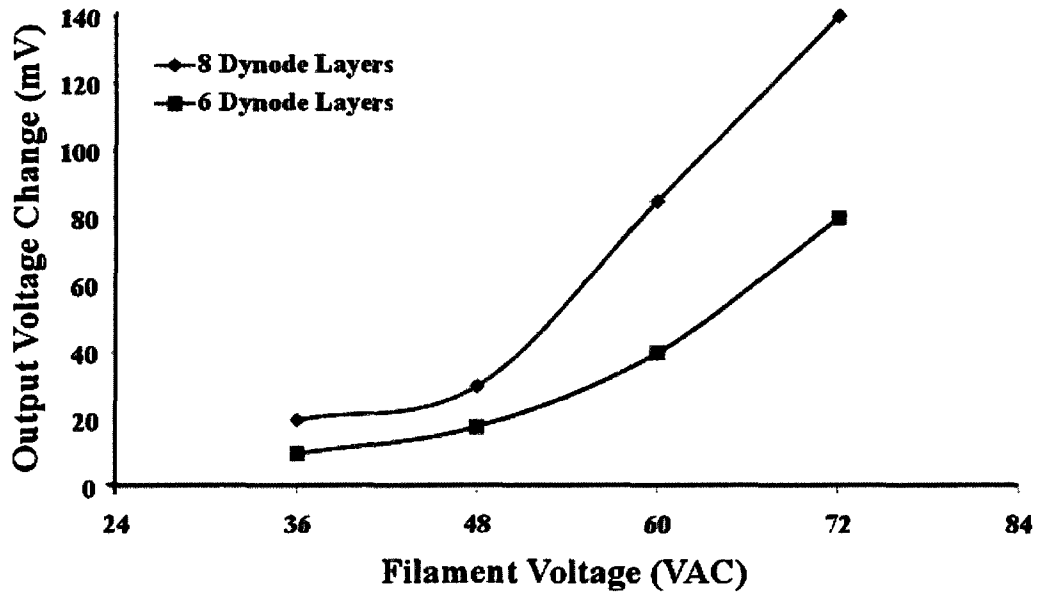


Figure 6.14 Voltage change versus filament voltage of the eight and six layer dynode stacks.

Both dynode stacks were tested at a dynode voltage of -1000 VDC. The six dynode layer device shows a reduction of the amount of electrons collected by about half when compared to the eight dynode layer device. The reduction of dynode stages reduces the number of dynodes available to create the electric field and stages available for amplification inside of the device, which results in fewer electrons being pulled to the anode.

PM tube dynodes are normally coated with an additional metal layer that has a higher secondary electron emission yield than dynode material to increase the number of electron avalanches that occur for each dynode. An aluminum coating was added to the dynode layers to increase the secondary electron emission of each layer for better electron amplification. The dynodes were coated with a 340 nm layer of aluminum using thermal evaporation. The aluminum coated stack was constructed using 8 dynode layers.

Figure 6.15 shows the amplification difference between the Al-coated and non-coated dynode layers. Both dynode stacks were tested using -1000 VDC for the dynode voltage.

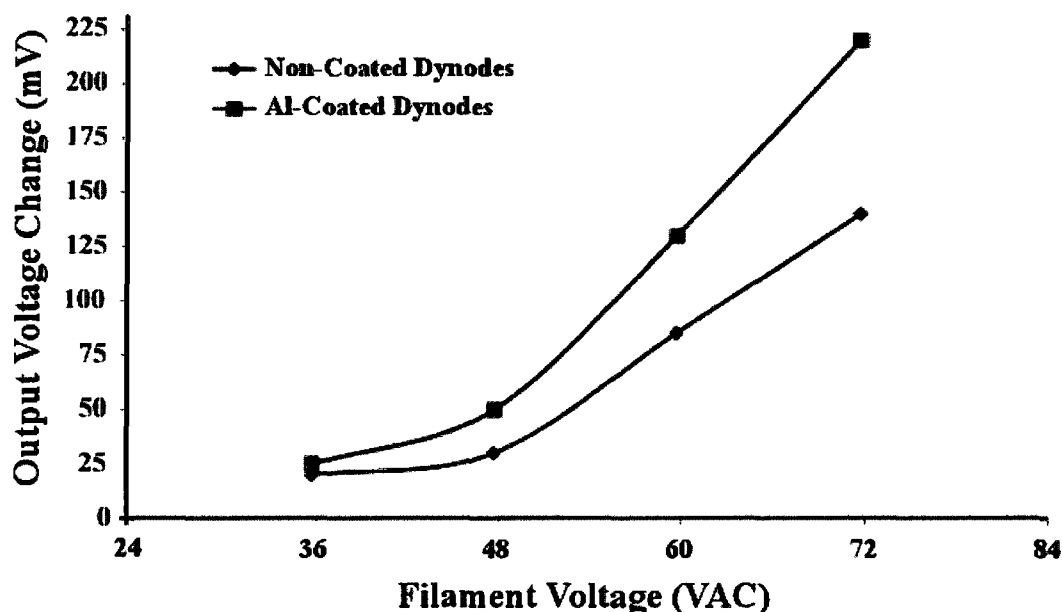


Figure 6.15 Voltage change versus filament voltage of the non-coated and Al-coated dynode stacks.

The aluminum coating increased the DC output of the device by about sixty percent when compared to the non-coated device. The use of higher yield secondary emission coating such as gallium phosphide, magnesium oxide, or lead oxide would increase the amplification of the dynodes even further.

The construction of a small PM tube is the final step in reducing the overall size of the detector platform. There is also the need for the device to have a low manufacturing cost so that a large number of devices can be deployed over an area. Sintered stainless steel dynodes were tested as a method to create cheaper and easier to built PM tubes. The stainless steel dynodes were able to collect the electrons emitted from the tungsten filament, and the addition of a secondary electron emission coating

further increased the collection efficiency of the device. Future testing of the device will include the construction of a photocathode material deposited on window for the device.

Another issue for the complete detector is power consumption and battery life. Since the PM tube amplification depends on the number of stages and the strength of the electric field created inside of the device, this design can be adapted to specific applications by changing the overall size of the device the number of stages used. The smaller the device is constructed, the closer the dynode layers can be stacked together. With the decrease in size, the amount of voltage needed to create the internal electric field is reduced since the electrons have a shorter path to travel between the photocathode and anode. The number of layers used for electron amplification would be dependent on the energy of radiation particles that are expected for the area where device is deployed; higher energy particles would not need the same amplification to have a useable signal for the circuitry as low energy particles.

REFERENCES

- [1] National Academy of Engineering, "Engineering's Grand Challenges," *National Academy of Engineering* 2008, [Online]. Available: <http://www.engineeringchallenges.org>. [Accessed: August 21, 2010]
- [2] G.F. Knoll, *Radiation Detection and Measurement*, 3rd ed. Danvers, MA: Wiley & Sons, Inc., 2000.
- [3] U.S. Senator P. Murray, "Senator Murray celebrates arrival of first cargo container secured through operation safe commerce," *U.S. Senator Patty Murray: Working for Washington State*, March 14, 2004. [Online]. Available: <http://murray.senate.gov/news.cfm?id=219197>. [Accessed: March 15, 2010.]
- [4] R. Waguespack, S. Pellegrin, B. Millet, and C.G. Wilson, "Integrated system for wireless radiation detection and tracking," *2007 IEEE Region 5 Technical Conference*, pp. 29-31, 2007.
- [5] K. Osberg, et al., "A hand-held neutron detector sensor system," *IEEE International Symposium on Circuits and Systems*, 2006.
- [6] S. Normand, et al., "Study of a new boron loaded plastic scintillator," *IEEE Transactions on Nuclear Science*, vol. 49, no. 2, pp. 577-582, April 2002.
- [7] J.S. Neal, et al., "A new scintillator for fast neutron detection: Single-crystal $\text{CeCl}_3(\text{CH}_3\text{OH})_4$," *IEEE Transactions on Nuclear Science*, vol. 57, no. 3, pp. 1692-1696, June 2010.
- [8] Y.T. Viday, et al., "Research and development of ceramic scintillators applied to alpha-particle detection," *Nuclear Science Symposium and Medical Imaging Conference Record*, pp. 762-763, 1995.
- [9] M.E. Keillor and L.W. Burgraf, "Detection alpha radiation by scintillation in porous materials," *IEEE Transactions on Nuclear Science*, vol. 44, no. 5, pp. 1741-1746, October 1997.
- [10] M. Katagiri, et al., "Scintillation materials for neutron imaging detectors," *Nuclear instruments and methods in physics research, section A: Accelerators, spectrometers, detectors, and associated equipment*, vol. 529, no. 1-3, pp. 274-279, August 2004.

- [11] T. Kojima, et al., "Neutron scintillators with high detection efficiency," *Nuclear instruments and methods in physics research, section A: Accelerators, spectrometers, detectors, and associated equipment*, vol. 529, no. 1-3, pp. 325-328, August 2004.
- [12] M. Katagiri, et al., "Neutron/ γ -ray discrimination characteristics of novel neutron scintillators," *Nuclear instruments and methods in physics research, section A: Accelerators, spectrometers, detectors, and associated equipment*, vol. 529, no. 1-3, pp. 317-320, August 2004.
- [13] L. Swiderski, et al., "Boron-10 loaded BC523A liquid scintillator for neutron detection in the border monitoring," *IEEE Transactions on Nuclear Science*, vol. 55, no. 6, pp. 3710-3716, 2008.
- [14] E. Kamaya, et al., "Organic scintillators containing ^{10}B for neutron detection," *Nuclear instruments and methods in physics research, section A: Accelerators, spectrometers, detectors, and associated equipment*, vol. 529, no 1-3, pp. 329-331, August 2004.
- [15] R. Aryaeinejad, et al., "Palm-size low-level neutron sensor for radiation monitoring," *IEEE Transactions on Nuclear Science*, vol. 43, no. 3, pp. 1539-1543, June 1996.
- [16] D.F. Spencer, R. Aryaeinejad, and E. L. Reber, "Using Cockroft-Walton voltage multiplier with small photomultipliers," *IEEE Transactions on Nuclear Science*, vol. 49, no. 3, pp. 1152-1155, June 2002.
- [17] R. Aryaeinejad and D.F. Spencer, "Pocket dual neutron/gamma radiation detector," *IEEE Transactions on Nuclear Science*, vol. 51, no. 4, pp. 1667-1671, August 2004.
- [18] M. Petasecca, et al., "Thermal and electrical characterization of silicon photomultiplier," *IEEE Transactions on Nuclear Science*, vol. 55, no. 3, pp. 1686-1690, June 2008.
- [19] M. Mazzillo, et al., "Quantum detection efficiency in Geiger mode avalanche photodiodes," *IEEE Transactions on Nuclear Science*, vol. 55, no. 6, pp. 3620-3625, December 2008.
- [20] D.J. Herbert, et al., "First results of scintillator readout with silicon photomultiplier," *IEEE Transactions on Nuclear Science*, vol. 53, no. 1, pp. 389-394, February 2006.
- [21] P. Finocchiaro, et al., "Features of silicon photomultipliers: Precision measurement of noise, cross-talk, afterpulsing detection efficiency," *IEEE Transactions on Nuclear Science*, vol. 56, no. 3, pp. 1033-1041, June 2009.

- [22] R. Bencardino and J.E. Eberhardt, "Development of a fast-neutron detector with silicon photomultiplier readout," *IEEE Transactions on Nuclear Science*, vol. 56, no. 3, pp. 1129-1134, June 2009.
- [23] C. Stapels, et al., "Solid-state photomultiplier in CMOS technology for gamma-ray detection and imaging applications," *IEEE Nuclear Science Symposium Conference Record*, vol. 5, pp. 2775-2779, 2005.
- [24] A. Osovizky, et al., "Scintillation light readout using silicon photomultiplier – Review and experimental results," *IEEE Nuclear Science Symposium Conference Record*, pp. 2482-2483, 2008.
- [25] C.H. Mesquita, T.M. Filho, and M.M. Hamada, "Development of neutron detector using the PIN photodiode with polyethylene (n,p) converter," *IEEE Transactions on Nuclear Science*, vol. 50, no. 4, pp. 1170-1174, August 2003.
- [26] D.S. McGregor, et al., "Design considerations for thin film coated semiconductor thermal neutron detectors - I: Basics regarding alpha particle emitting neutron reactive films," *Nuclear instruments and methods in physics research, section A: Accelerators, spectrometers, detectors, and associated equipment*, vol. 500, no 1-3, pp. 272-308, November 2003.
- [27] D.S. McGregor, et al., "Perforated semiconductor neutron detector modules for detection of spontaneous fission neutrons," *IEEE Conference on technologies for homeland security: Enhancing critical infrastructure dependability*, pp. 162-167, 2007.
- [28] F.H. Ruddy, et al., "The fast neutron response of 4H silicon carbide semiconductor radiation detectors," *IEEE Transactions on Nuclear Science*, vol. 53, no. 3, pp. 1666-1670, June 2006.
- [29] S. Metzger, et al., "Silicon carbide radiation detector for harsh environments," *Proceedings of the European conference on radiation and its effects on components and systems*, pp. 51-56, 2002.
- [30] C.G. Wilson, C.K. Eun, and Y.B. Gianchandani, "D-MicroGeiger: A microfabricated beta-particle detector with dual cavities for energy spectroscopy," *18th IEEE International Conference on Micro Electro Mechanical Systems*, vol. 1, pp. 622-625, February 2005.
- [31] C.K. Eun, R. Gharpurey, and Y.B. Gianchandani, "Controlling ultra wide band transmissions from a wireless micromachined Geiger counter," *19th IEEE International Conference on Micro Electro Mechanical Systems*, vol. 1, pp. 570-573, 2006.
- [32] A. Oed, "Position-sensitive detector with microstrip anode for electron multiplication with gases," *Nuclear instruments and methods in physics research, section A: Accelerators, spectrometers, detectors, and associated equipment*, vol. 263, no. 2-3, pp. 351-359, January 1988.

- [33] J. Miyamoto, et al., "Passivation micro-strip gas chambers with an interstitial germanium coating," *IEEE Transactions on Nuclear Science*, vol. 44, no. 3, pp. 660-664, June 1997.
- [34] T. Nakamura, "Usage of a capillary plate as a pre-gas-amplification device for Neutron microstrip gas chamber," *IEEE Transactions on Nuclear Science*, vol. 51, no. 4, pp. 1519-1523, August 2004.
- [35] F. Sauli, "GEM: A new concept for electron amplification in gas detectors," *Nuclear instruments and methods in physics research, section A: Accelerators, spectrometers, detectors, and associated equipment*, vol. 386, no. 2-3, pp. 531-534, February 1997.
- [36] R. Bouclier, et al., "The gas electron multiplier (GEM)," *IEEE Transactions on Nuclear Science*, vol. 44, no. 3, pp. 646-650, June 1997.
- [37] J. Benlloch, et al., "Development of the gas electron multiplier (GEM)," *IEEE Transactions on Nuclear Science*, vol. 45, no. 3, pp. 234-243, June 1998.
- [38] G. Bencivenni, et al., "A fast mult-GEM-based detector for high-rate, charged-particle triggering," *IEEE Transactions on Nuclear Science*, vol. 49, no. 6, pp. 3242-3246, December 2002.
- [39] G. Bencivenni, et al., "Measurement of GEM parameters with x-rays," *IEEE Transactions on Nuclear Science*, vol. 50, no. 5, pp. 1297-1302, October 2003.
- [40] S. Park, Y.K. Kim, and J.K. Kim, "Neutron detection with a GEM," *IEEE Transactions on Nuclear Science*, vol. 52, no. 5, pp. 1689-1692, October 2005.
- [41] J.F.C.A Veloso, J.M.F. Dos Santos, and C.A.N. Conde, "A proposed new microstructure for gas radiation detectors: Microhole and strip plate," *Review of Scientific Instruments*, vol. 71, no 6, pp. 2317-2376, June 2000.
- [42] J.F.C.A Veloso, et al., "Micro-hole & strip plate detector for neutron detection," *IEEE Nuclear Science Symposium Conference Record*, 2003, vol. 1, pp. 257-262.
- [43] K. Siegbahn, *Alpha-, Beta- and Gamma-Ray Spectroscopy*, Amsterdam: North-Holland Publishing, 1965.
- [44] W. Price, *Nuclear Radiation Detection*, New York: McGraw-Hill, Inc., 1958.
- [45] E. Kowalski, *Nuclear Electronics*, Heidelberg Berlin: Springer-Verlag, 1970.
- [46] R. Lapp, and H. Andrews, *Nuclear Radiation Physics*, 4th ed. Englewood Cliffs, New Jersey: Prentice-Hall, Inc., 1972.
- [47] R. Dasaka, S. Pellegrin, M. Kamavaram, and C. Wilson, "Micromachined scintillation device with charge conversion nanoparticles for neutron and beta particle detection," *Proceeding MicroTas*, 2005, pp. 472-475.

- [48] A.G. Stewart, et al., "Performance of 1-mm² silicon photomultiplier," *IEEE Journal of Quantum Electronics*, vol. 44, no. 2, pp. 157-164, 2008.
- [49] S. Pellegrin, C. Whitney, and C.G. Wilson, "A multichannel nanoparticle scintillation microdevice with integrated waveguides for alpha, beta, gamma, x-ray, and neutron detection," *Journal of Microelectromechanical Systems*, vol. 19, no. 5, pp. 1207-1214, October 2010.
- [50] A.M. Conway, et al., "Numerical simulations of pillar structured solid state thermal neutron detector: Efficiency and gamma discrimination," *IEEE Transactions on Nuclear Science*, vol. 56, no. 5, pp. 2802-2807, 2009.
- [51] R.C. Byrd, et al., "Warhead counting using neutron scintillators: Detector development, testing, and demonstration," *IEEE Transactions on Nuclear Science*, vol. 39, no. 4, pp. 1051-1055, August 1992.
- [52] C.E. Moss, et al., "Neutron detectors for active interrogation of highly enriched uranium," *IEEE Transactions on Nuclear Science*, vol. 51, no. 4, pp.1677-1681, August 2004.
- [53] M. Kanyo, et al., "Two-dimensional neutron scintillation detector with optimal gamma discrimination," *IEEE Transactions on Nuclear Science*, vol. 40, pp. 438-442, August 1993.
- [54] T. Itoh, et al., "Development of a new 1-Dimensional γ -ray position sensor using scintillators coupled to a Si strip detector," *IEEE Transactions on Nuclear Science*, vol. 53, pp. 2983-2990, October 2006.
- [55] Ortec, *Pre-amplifier Introduction*, Ortec. [Online]. Available: <http://www.ortec-online.com/download.aspx?AttributeFileId=e7dad471-20f3-465a-8e3f-27ee1c34fa0b>. [Accessed: August 12, 2010]
- [56] A.R. Hambley, *Electronics*, 2nd ed. New Jersey: Prentice Hall, 2000, pp. 728-729.
- [57] B.P. Lathi, *Signal Processing & Linear Systems*, New York: Oxford University Press, 1998, pp. 408-410.
- [58] V. Polushkin, *Nuclear Electronics*, England: Wiley, 2004, pp. 307.
- [59] T.S. Perry, "For the Record: Jack Kilby and the IC," *IEEE Spectrum*, vol. 25, no. 13, pp 40-41, 1988.
- [60] R.J. Baker, *CMOS Circuit Design, Layout, and Simulation*, New Jersey: Wiley-Interscience, 2008.
- [61] MOSIS, *MOSIS Wafer Acceptance Test*, The MOSIS Service. [Online]. Available: http://www.mosis.com/cgi-bin/cgiwrap/umosis/swp/params/tsmc-035/t88f_mm_epi-params.txt [Accessed: October 21, 2009]
- [62] A. Hasting, *The Art of Analog Layout*, New Jersey: Pearson Education, Inc., 2006.

- [63] Burle Industries, Inc., *Photomultiplier Handbook*, USA: Burle Technologies, Inc., 1980. [Online]. Available: <http://psec.uchicago.edu/links.php>. [Accessed: December 29, 2010].
- [64] K.C. Burr and G. Wang, "Scintillation detection using 3 mm x 3 mm silicon photomultipliers," *IEEE Nuclear Science Symposium Conference Record*, 2007, vol. 2, pp. 975-982.
- [65] A. Breskin, et al., "Sealed gas UV-photon detector with a multi-GEM multiplier," *IEEE Transactions on Nuclear Science*, vol. 48, no. 3, pp. 417-420, 2001.
- [66] J. M. Maia, et al., "Progress in MHSP electron multiplier operation," *Nuclear Science Symposium Conference Record*, 2003, vol. 1, pp. 525-529.
- [67] Hamamatsu Photonics K.K., *Photomultiplier Tubes Basics and Applications*, Hamamatsu. [Online]. Available: http://sales.hamamatsu.com/assets/applications/ETD/pmt_handbook_complete.pdf. [Accessed December 30, 2010].
- [68] K.R. Spring, M.W. Davidson, "Theory of Confocal Microscopes - Electronic Light Detectors: Photomultiplier," Olympus. [Online]. Available: <http://www.olympusfluoview.com/theory/pmtintro.html>. [Accessed December 28, 2010].
- [69] T. Garino, et al., "The fabrication of stainless steel parts for MEMS," Sandia National Laboratory, Albuquerque, NM, 2002.
- [70] M. Imbasy, H. Ostadi, and K. Jiang, "Characterization of stainless steel microparts fabricated by soft molding techniques," *Mirco & Nano Letters*, vol. 4, iss. 2, pp. 99-105, 2009.
- [71] J. G. Zhou and Z. He, "Rapid pattern base powder sintering technique and related shrinkage control," *Journal of Materials and Design*, vol. 19, pp. 241-248, 1998.